Chem Soc Rev

Designs from Single Junction, Heterojunction to Multijunction for High-Performance Perovskite Solar Cells

Journal:	*Chemical Society Reviews*
Manuscript ID	CS-REV-09-2021-000841
Article Type:	Review Article
Date Submitted by the Author:	05-Sep-2021
Complete List of Authors:	Wu, Xin; City University of Hong Kong, CHEM Li, Bo; City University of Hong Kong Zhu, Zonglong; City University of Hong Kong, CHEM Chueh, Chu-Chen; National Taiwan University, Department of Chemical Engineering Jen, Alex; City University of Hong Kong, CHEM

ARTICLE

Designs from Single Junction, Heterojunction to Multijunction for High-Performance Perovskite Solar Cells

Received 00th January 20xx,
Accepted 00th January 20xx

DOI: 10.1039/x0xx00000x

Xin Wu,[a] Bo Li,[b] Zonglong Zhu,*[a,d] Chu-Chen Chueh*[c] and Alex. K.-Y. Jen*[a,b,d,e]

Hybrid metal-halide perovskite solar cells (PVSCs) have drawn unprecedented attention during the last decade due to their superior photovoltaic performance, facile and low-cost fabrication, and potential for roll-to-roll mass production and application for portable devices. Through the collective composition, interface, and process engineering, comprehensive understanding of the structure-property relationship and carrier dynamics in perovskites have been established to help achieve a very high certified power conversion efficiency (PCE) of 25.5%. Apart from material properties, the modified heterojunction design and device configuration evolution also play a crucial role in enhancing the efficiency. The adoption and/or modification of heterojunction structure have been demonstrated to effectively suppress the carrier recombination and potential losses in PVSCs. Moreover, the employment of multijunction structure has been shown to reduce thermalization losses for achieving a high PCE of 29.52% in perovskite/silicon tandem solar cells. Therefore, understanding the evolution of device configuration of PVSCs from single junction, heterojunction to multijunction is helpful for the researchers in this field to further boost the PCE to beyond 30%. Herein, we summarize the evolution and progress of the single junction, heterojunction and multijunction designs for high-performance PVSCs. A comprehensive review of the fundamentals and working principles in these designs is presented. We first introduce the basic working principles of single junction PVSCs and the intrinsic properties (such as crystallinity and defects) in perovskite films. Afterwards, the progress of the diverse heterojunction designs and perovskite-based multijunction solar cells is synopsized and reviewed. Meanwhile, the challenges and strategies to further enhance the performance are also summarized. At the end, the perspectives on future development of perovskite-based solar cells are provided. We hope this review can provide the readers to a quick catchup on this emerging solution-processable photovoltaic technology, which is currently at the transition stage towards commercialization.

1. Introduction

Photovoltaics (PV) has one of the most important technologies for human not only for it to serve as a clean energy source to address the needs of the rapidly developing world but also help ensure a sustainable environment compared to other traditional fossil fuels. To facilitate the large-scale deployment of solar cells, it requires the PV systems to have continuously reduced levelized cost of electricity (LCOE).[1, 2] Reducing the cost of raw materials combined with enhancing the power conversion efficiency (PCE) and lifetime of PV modules play a decisive role in lowering the non-module cost. In the past decade, perovskite solar cells (PVSCs) have drawn unprecedented attention due to their extraordinary optical and electronic properties, including ambipolar transport characteristics, high absorption coefficients, low exciton binding energies, high carrier mobilities, long carrier lifetime, and high defect tolerance.[3, 4] The PCEs of PVSCs have soared from 3.8% to a certified value of 25.5% within a decade of development, which can rival the performance of commercial inorganics-based counterparts.[5, 6] Apart from the promising performance, the facile, low-cost fabrication, and diverse applications of PVSCs render them as a perfect candidate for the next-generation PV technology.[7-10] In spite of all these aforementioned merits, there is still a strong need to further improve the device performance and stability of PVSCs in order to meet the specs set for commercialization.

Perovskites are typically processed through facile solution-based techniques, resulting in heterogeneity from short length scales (<100 nm) to ranges (>10 μm).[11] Due to the defects,[12-14] such as vacancies, interstitials, and anti-site substitutions at grain boundaries, the grain-to-grain interfaces in the polycrystalline perovskite film dramatically influence the charge dynamics and recombination, ion migration, and the infiltration of external species.[15-18] The control of crystallization and passivation of defects in single junction PVSCs is important. Meanwhile, the interfaces between perovskite and charge-

[a] Department of Chemistry, City University of Hong Kong, Kowloon 999077, Hong Kong. Email: zonglzhu@cityu.edu.hk, alexjen@cityu.edu.hk
[b] Department of Materials Science and Engineering, City University of Hong Kong, Kowloon 999077, Hong Kong.
[c] Department of Chemical Engineering and Advanced Research Center for Green Materials Science and Technology, National Taiwan University, Taipei, 10617, Taiwan. Email: cchueh@ntu.edu.tw
[d] Hong Kong Institute for Clean Energy, City University of Hong Kong, Kowloon 999077, Hong Kong
[e] Department of Materials Science & Engineering, University of Washington, Seattle, Washington, 98195, United States

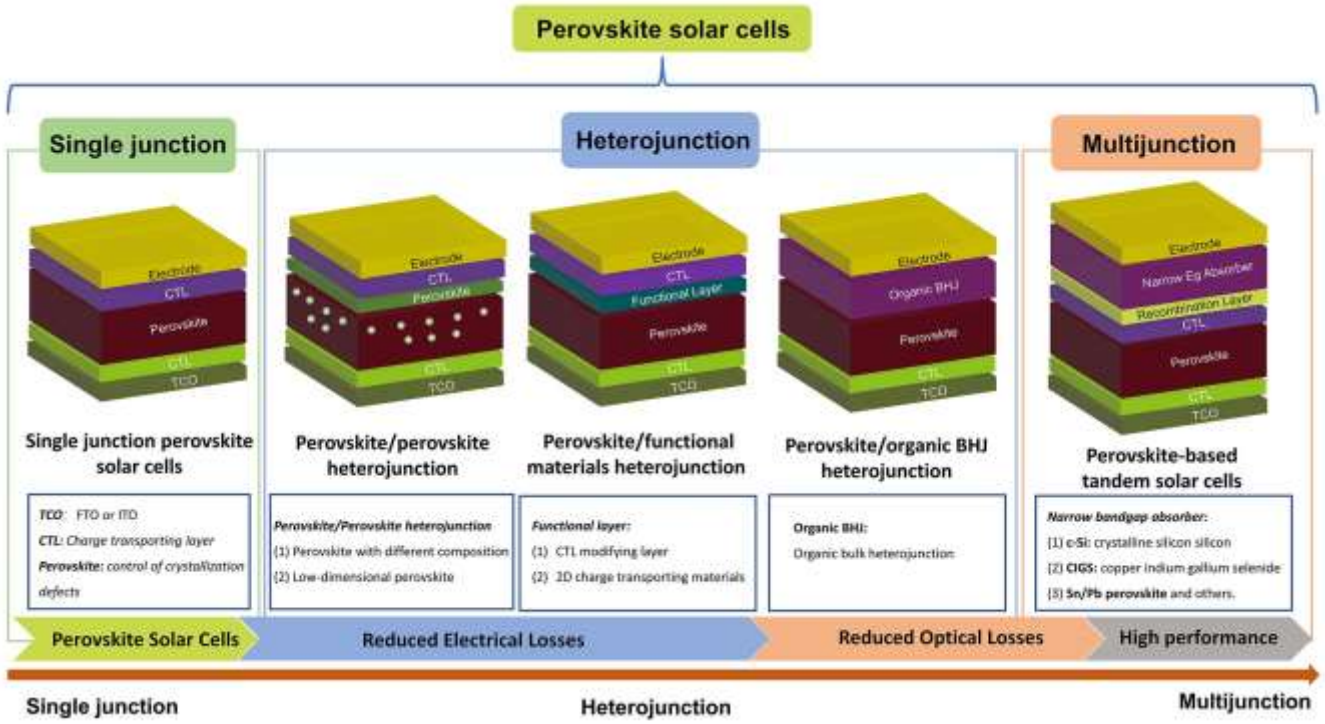

Fig. 1 Device evolution of perovskite solar cells from single junction, heterojunction, to multijunction designs.

transporting layers are also crucial for the performance because they influence the built-in electric field and the accumulation of charges and defects.[19-21]

As the defects in the bulk of perovskites and at the interfaces both cause the non-radiative recombination and instability, modifying the heterointerfaces of PVSCs becomes more pivotal to enhance device performance compared to other photovoltaic technologies. Myriads of strategies have been developed to alter the heterojunction designs of perovskites, including composition engineering to construct gradient perovskite (or perovskite/perovskite) heterojunction, interfacial modifications, development of new charge transporting materials (CTMs) to form perovskite/functional layer heterojunction, and employment of organic bulk-heterojunction as CTMs to reduce the optical losses, which can dramatically enhance the device performance by reducing the energy losses in PVSCs. (Fig. 1).

Although the advanced heterojunction designs of perovskites have enabled PCEs to reach as high as 25.5 % for PVSCs, exceeding 75% of 75% of their S-Q limit (Fig. 2), their theoretical maximum efficiency is still limited by the Shockley-Queisser (S-Q) limit.[22, 23] To break the S-Q limit for achieving PCE > 30%, it requires the further exploration of strategies in multijunction design. In principle, a multijunction solar cell comprises both wide-bandgap and narrow-bandgap absorbers to provide the complementary coverage of absorption for the solar spectrum, which can not only effectively reduce the below E_g loss for the wide E_g absorber but also suppress the thermalization loss for the narrow E_g absorber, resulting in the increment of maximum efficiency.[24, 25] The tunable E_g of perovskite materials from 1.2 eV to 2.3 eV makes them ideal absorbers in multijunction solar cells.[26] In the past five years, wide E_g perovskites have been combined with silicon, copper indium gallium selenide (CIGS), narrow E_g perovskites and organic bulk-heterojunction (BHJ) to realize high-performance multijunction solar cells (Fig. 1).[27, 28] Through sophisticated optimization of sub cells and interlayers, an unprecedented PCE of 29.52 % has been achieved recently in a two-terminal perovskite/silicon tandem solar cell,[29] confirming that the simultaneous optimization of heterojunction and multijunction design is promising for further improving solar cell performance.

As illustrated in Fig. 1, the advanced heterojunction designs and their evolution to multijunction designs in PVSCs

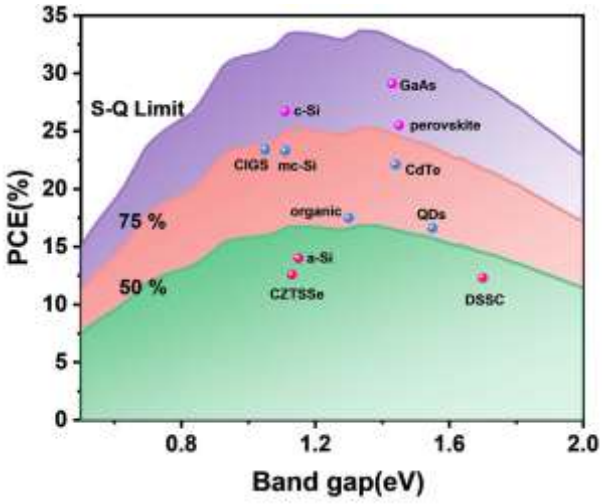

Fig. 2 S-Q limits with the record efficiencies of different PV technologies plotted as a function of bandgap.[6]

have efficiently reduced energy losses from different paths and successfully improved PCE close to 30%. A comprehensive review of such device evolution can provide researchers with better guidance for the further advancement of this field. Hence, we systematically introduce the fundamentals and experimental progresses of heterojunction and multijunction designs in perovskite solar cells in this review. First, the working mechanism of single junction PVSCs and the key points to achieve high-quality perovskite materials are introduced, followed by reviewing the heterojunction designs, including gradient perovskite (or perovskite/perovskite) heterojunction design to enhance charge carrier extraction and suppress non-radiative recombination, perovskite/functional layers heterojunction design for interfacial modifications, and perovskite/organic BHJ heterojunction to realize panchromatic light-harvesting. Afterwards, the working principles and potential of perovskite-based multijunction solar cells are discussed, and their representative progresses, including perovskite/silicon, perovskite/CIGS, perovskite/perovskite, and other tandem solar cells, are summarized. Finally, an outlook for PVSCs is provided to offer a guideline for further development of this field.

2. Design, Fabrication and Application for Single Junction, Heterojunction and Multijunction High-Performance PVSCs

2.1 Single Junction PVSCs.

2.1.1 Basic working principles.

In single junction PVSCs, the free-carrier model is always used for understanding the fundamental properties of perovskites, and the charge transport and dissociation happened at the heterointerfaces in the device.[30] To better understand the working mechanism of PVSCs, a comprehensive understanding of the basics of heterojunction is required. Fig. 3 showed three types of heterojunctions, in which E_0 represents the vacuum level, E_C and E_V are the conduction band edge and

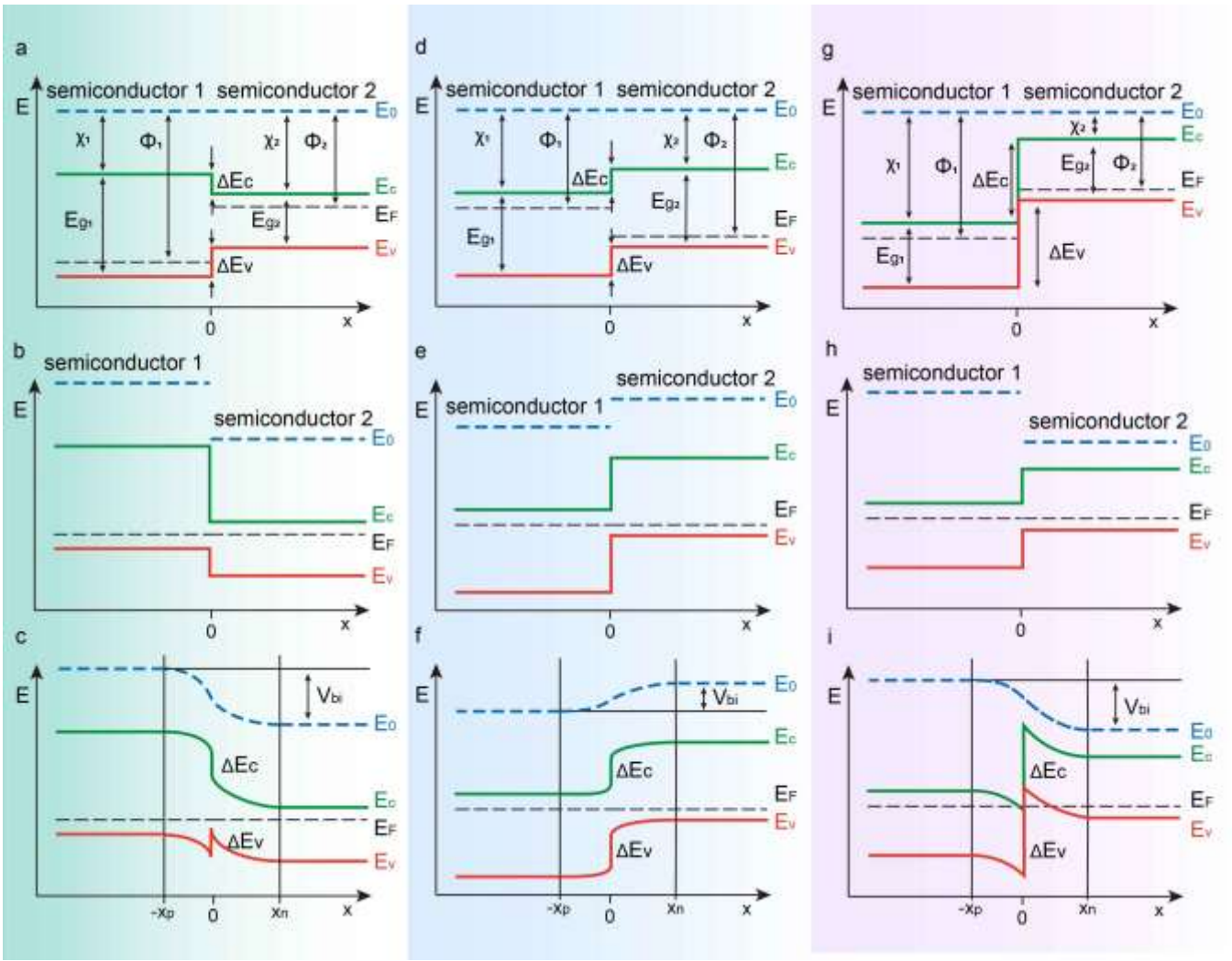

Fig. 3 Schematic band diagrams for three typical heterojunctions with aligned vacuum level E_0 (a: type I-straddled, d: type II-staggered, g: type III-broken gap), brought into thermodynamic equilibrium resulting in an aligned Fermi level (E_F) (b, e, h), and brought into contact with compensating space-charge regions (c, f, i).

valence band edge respectively, E_F refers to the fermi level, Φ is the work function and equals to E_0-E_F, χ is the electron affinity which equals to E_0-E_c, and E_g is the bandgap of semiconductors. When two semiconductors with different bandgaps are in contact, a heterojunction is formed, band bending and built-in electric field will occur. Depending upon the difference between χ_1 and χ_2, there are three types of possible band lineups of semiconductor heterojunctions: (a) type I alignment (straddled configuration), (d) type II (staggered), (g) type III (misaligned, broken gap) (Fig. 3).

When a p-doped semiconductor (semiconductor 1) contacts with an n-doped semiconductor (semiconductor 2), the E_F is not uniform throughout the junction, carriers will then exchange between both sides to reach thermal equilibrium. Here, type II heterojunction is taken as an example to explain the establishment of the equilibrium, for which it appears more frequently and is the efficient structure encountered in PVSCs.[31] In type II heterojunction (Fig. 3d), there are more electrons in the semiconductor 1 (n-side) than in the semiconductor 2 (p-side), the electrons will thus diffuse from the n-side to the p-side. As a result, a net positive charge density appears on the left side of the interface (x < 0). Holes in p-side transport in a similar way and result negative charge density on the right side. An electric field is therefore created which points from n-side to p-side due to charge densities on left and right sides, causing the drift of the electron and hole currents in a direction opposite to the diffusive currents.

When more charged carriers diffuse, the electric field is gradually enhanced until the drift components are equal to the opposite diffusive components. Then, the junction is in equilibrium (Fig. 3e) and E_F is flat and constant throughout the heterojunction. Notably, the electrostatic potentials are required to be added to the energies in band structure because E_0 is not equal in two materials. While inside the depletion regions, the occurrence of band bending affirms the existence of an electric field and electrostatic potential as well as the vacuum level also bend in response to the electric field, as shown in Fig. 3f, where the built-in electric field qV_{bi} equals the difference in the E_F of the two semiconductors under thermal equilibrium condition.

For single junction PVSCs, there are two common device structures (Fig. 4a, b): conventional (n–i–p) and inverted (p–i–n) structures and the basic working principle is illustrated in Fig. 4c. When light passes through the perovskite layer, excitons are generated and immediately dissociate into electrons and holes due to the low binding energy (~0.03 eV).[32-34] These free carriers travel through the perovskite film efficiently to charge-transporting layers (CTLs) due to the long carrier diffusion lengths.[35, 36] The favorable energy level alignment at the CTL/perovskite interface (heterointerface) enables the effective extraction of electrons and holes by electron-transporting layer (ETL) and hole-transporting layer (HTL). In this process, ETL also serves as a hole-blocking layer to prevent charge carrier from recombining by forming an energy barrier. Then, the carriers are collected by two electrodes and transport through the external electric circuit and load to produce electricity.

Different from the thermal equilibrium mentioned in Fig. 3, when absorbing photons and generate carriers, the thermal equilibrium of heterojunctions is broken, which changes the populations of electrons in the conduction band (CB) and valence band (VB) respectively. Under this circumstance, the E_F of perovskite under thermal equilibrium is not applicable. As the relaxation time for electrons within each band is much lower than across the band gap, the CB and VB finally reach an individual population which is internally in equilibrium. Therefore, quasi Fermi level was defined to describe this quasi thermal equilibrium state, in which the quasi-fermi level of electrons ($E_{F,e}$) and quasi-fermi level of holes ($E_{F,h}$) quantitatively indicating the density of the free photogenerated electron (holes) in the conduction (valence) band. The difference between $E_{F,e}$ and $E_{F,h}$ is defined as quasi-Fermi level splitting (QFLS).

In single junction PVSCs, the absolute positions of $E_{F,e}$ and $E_{F,h}$ are not easy to be measured, and the QFSL that can be calculated from photoluminescence quantum yield (PLQY) is thus used for characterizing the recombination losses. Theoretically, the QFSL represents the internal voltage (V_{int}) of

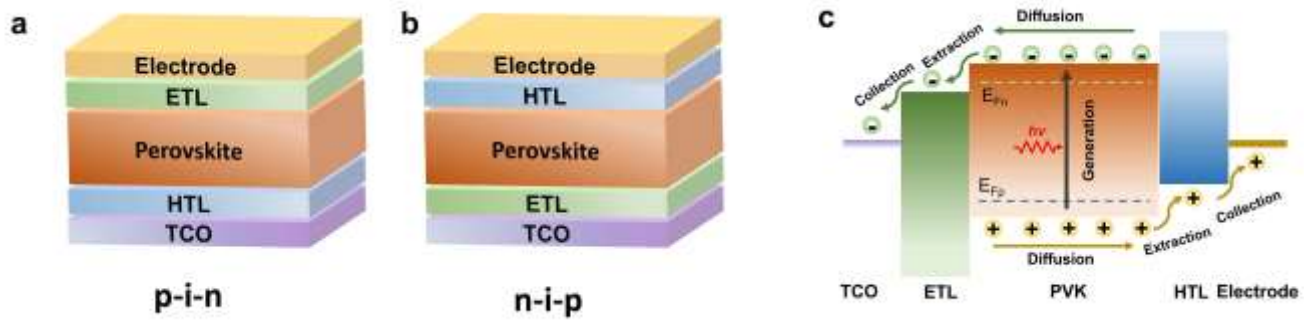

Fig. 4 Device configuration of (a) n-i-p structured and (b) p-i-n structured PVSCs. (c) Charge carrier dynamics of a PVSC.

the device and should equal the device's external open-circuit voltage (V_{OC}). It can be calculated through equation (1) according to the literature,[37] where *k* represents Boltzmann's constant, n_{id} is the ideality factor which describes the deviation from the ideal diode condition where only pure bimolecular recombination is considered, J_{ph} is the photocurrent at V_{OC}, and J_0 is the total dark current. This equation indicates that both QFLS and *Voc* are mainly affected by the light intensity which also influence J_{ph}, carrier density, and the radiative/non-radiative charge recombination. Given that radiation recombination is the same for a certain system due to the S-Q limit, suppressing the non-radiative recombination caused by defects in perovskites is of great importance to achieve high-performance PVSCs.

$$V_{OC} = \text{QFLS} = \frac{n_{id}kT}{q}\ln\left(\frac{J_{ph}(V_{OC})}{J_0} + 1\right) \quad (1)$$

However, Neher *et. al* found that the QFSL not equals V_{OC} in real situations.[38] As compared with QFLS (Fig. 5a, b), a lower V_{OC} is always attained due to the energetic misalignment at perovskite CTL/interface. This misalignment, instead of the defects in the perovskite film, induces the non-radiative recombination loss. Therefore, perfectly aligned and fully blocking transport layer is essential for constructing an ideal perovskite/CTL heterojunction to lessen the QFLS-V_{OC} mismatch and to enhance the *V*oc in real situations.

In view of aforementioned working mechanism, to reduce the energy loss and enhance efficiency of single junction PVSCs, there are mainly two aspects to note. First, CTLs with high carrier mobility and aligned energy levels to perovskite materials should be used to ensure adequate built-in electric field and efficient charge carrier extraction and transport. Second, the defects density of perovskite films should be low to reduce the recombination loss. To achieve this, both the perovskite film and CTLs should be defect-free.

2.1.2 Defects in perovskites.

Understanding the defect nature of perovskites is an important issue in single-junction PVSCs. Due to the polycrystalline nature, the properties of defects in perovskite films are crucial for the carrier diffusion length and performance of devices. The commonly used perovskite for device fabrication has an ABX_3 3D crystal structure with an A-site cation ($CH_3NH_3^+$, $CH\text{-}(NH_2)_2^+$, Cs^+, or Rb^+), a B-site metal cation (Pb^{2+} or Sn^{2+}), and three halide anions X^- (I^-, Br^-, or Cl^-). For an ideal perovskite crystal, every ion is located at the equilibrium site. Nevertheless, in fact, it is inevitable to form a great number of structural defects induced by the solution process and post treatments. Defects can be simply classified into shallow-level defects and deep-level defects according to their formation energy. Meanwhile, defects in semiconductors are classified into point defects (vacancies, interstitials, and anti-site substitutions) and higher dimensional defects (dislocations, grain boundaries, and precipitates).[13]

The defects in perovskite films are mainly composed of point defects, two-dimensional defects (such as grain boundaries and surface defects), and three-dimensional defects (such as lead clusters).[14] For example, in a $MAPbI_3$ film, points defects are the dominating defects, including vacancies (V_{MA}, V_{Pb}, V_I), interstitials (MA_i, Pb_i, I_i), cation substitutions (MA_{Pb}, Pb_{MA}), and anti-site substitutions (MA_I, Pb_I, I_{MA}, I_{Pb}). Yin *et al.* have calculated the formation energies of each kind of defects (Fig. 6a, b).[12] Some defects occupy shallow levels have low formation energies, such as V_{MA}, V_{Pb}, V_I, MA_i, I_i, and MA_{Pb}. Other defects are deep-level defects that have high formation energies, including I_{MA}, I_{Pb}, Pb_i, and Pb_I.

Generally, when carriers are trapped by shallow-level defects, they are more likely to be de-trapped back to the conduction (valence) band by phonon absorption due to its

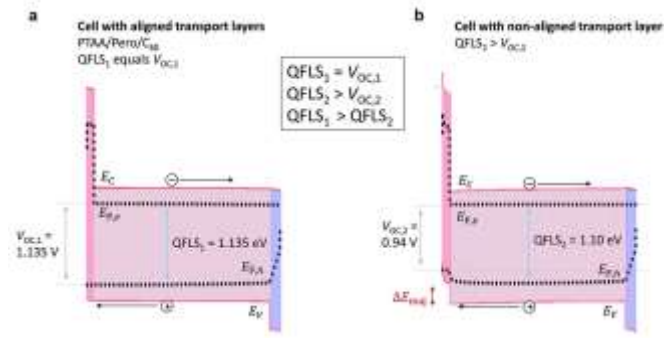

Fig. 5 Simulation of the QFLS and V_{OC} of pin-type devices using SCAPS from ref 38. (a) The simulated quasi-Fermi level splitting (QFLS) in junctions with aligned transport layers (PTAA/perovskite/C60) is equal to eV_{OC} but not in case of energetically mis-aligned transport layers (b) where the hole QFL bends at the interface to the hole transport layer which causes a QFLS–V_{OC} mismatch. The dashed lines exhibit the electron and hole quasi-Fermi levels ($E_{F,e}$ and $E_{F,h}$), the resulting QFLS in the absorber and V_{OC} at the contacts. The HTL (red) and ETL (blue) are represented by their bandgaps in between the highest occupied and lowest unoccupied molecular orbitals. Reproduced from ref 38 with permission from Royal Society of Chemistry, copyright 2019.

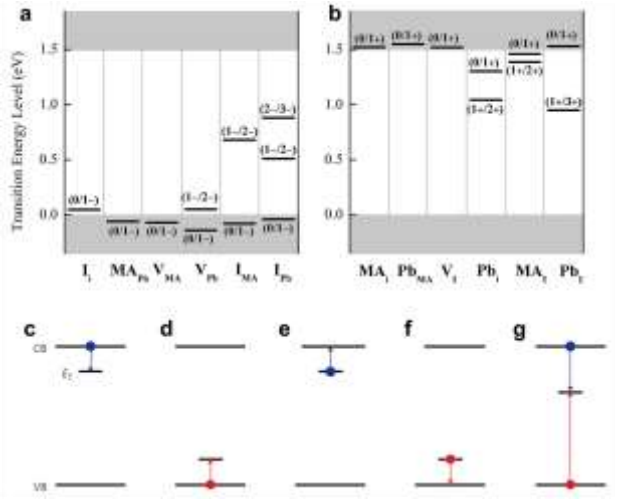

Fig. 6 Transition energy levels of (a) intrinsic acceptors and (b) intrinsic donors in $MAPbI_3$. Reproduced from ref 12 with permission from AIP Publishing LLC, copyright 2014. (c) Electron capture and (d) hole capture by a defect of energy trap between the conduction band (CB) and valance band (VB). (e) Electron emission and (f) Hole emission. (g) Electron and hole capture by a recombination center in a trap-assisted recombination event. Reproduced from ref 13 with permission from Nature Publishing Group, copyright 2016.

small activation energy (Fig. 6c-f). Therefore, shallow-level defects are not responsible for non-radiative recombination. In contrast, the carriers trapped by deep-level defects are more likely to recombine with an opposite carrier, causing non-radiative recombination (Fig. 6g). During the operation of a PVSC, the photo-generated carriers cause the splitting of quasi-E_f of electrons and holes. The quasi-E_f splitting (QFLS) theoretically determines the obtained open-circuit voltage (V_{OC}). When the charge generation rate equals the charge recombination rate, the QFLS is affected by the charge density.

The trap-assisted non-radiative recombination reduces charge density and causes reduction of QFLS. As a result, the V_{OC} and PCE are reduced. Fortunately, only deep-level defects serve as the non-radiative recombination center in PVSCs and their density is low in the perovskite films, therefore, perovskites are considered as defects tolerant materials. Although shallow-level defects are not responsible for non-radiative recombination, they tend to ionize at room temperature and serve as dopants of perovskite semiconductor. Besides, the migration of shallow-level defects causes device's hysteresis behaviours, phase segregation, and degradation of devices *via* ion migration. Therefore, proper defect passivation becomes essential for realizing high-performance and stable PVSCs.

2.1.3 Deposition techniques and crystallization modification of perovskite films.

In single junction PVSCs, the preparation of high-quality perovskite films with controllable morphology and high coverage with minimum pinholes remain to be very challenging. Some key factors affect the photovoltaic performance of PVSCs, such as charge dissociation efficiency, carrier transport and diffusion length, are related to the morphology and crystallinity of the films.[39-41] Crystallization is a complex process involving crystal nucleation and growth, which is highly dependent on the solution supersaturation.[42] In the perovskite precursor solution, the supersaturated state promotes nucleation and forms nuclei-clusters that are conducive to crystal growth.

Nucleation can occur homogeneously or heterogeneously from a continuous phase.[42] Homogeneous nucleation determined by the total excess free energy is only an intrinsic material process. In contrast, heterogeneous nucleation that occurs on a foreign nucleus or surface needs to consider the surface or interface contact energy due to wetting on the foreign surface.[43] Therefore, the factors influencing surface properties, such as surface chemistry, material type, surface heat treatment, surface morphology, etc., are very relevant in addressing these nucleation issues. The crystal growth, followed by the nucleus formation, is produced as the clusters diffuse to the surface of the existing nucleus and combine with the crystal lattice structures.[44] The transport of clusters can be controlled by diffusion and convection, which are driven by the molecular thermal motion and energy gradient in the system.[45] In general, fast nucleation can increase the coverage of perovskite thin films, and controlling crystal growth contributes to the formation highly crystalline materials. In this section, the recent reports of modifying the perovskite film morphology and crystallization will be reviewed based on different film deposition techniques.

2.1.3.1 One-step solution deposition method. The morphology and crystallization kinetics of perovskite materials are highly dependent on the film deposition techniques, solvents and additives. The perovskite precursor solutions can either be deposited simultaneously or sequentially, which leads to a series of perovskite thin-film deposition techniques. In the one-step method, perovskite precursor solution composed of metal halides and organic halides in a proper solvent is directly deposited on the substrate. Generally, without any modification to the composition or modulation to the crystallization process, the one-step deposition method produces more uncontrollable crystal nucleation and growth, resulting in poor coverage and morphologies, and thus an inferior photovoltaic performance.

Incorporating molecular additives in perovskite films is one of the most common strategies to modulate the perovskite film morphology. The excellent coordination capability of lead cations and iodide anions with molecules (functional groups) makes this approach quite effective. Pb^{2+} is considered as a Lewis acid and coordinates with N-donor, O-donor, S-donor in polar solvents (such as DMSO, DMF, NMP, etc.) to form Lewis acid-base adducts, which significantly influence the crystallization of perovskite.

As the affinity of different Lewis bases with PbI_2 differs with each other (donor capability with PbI_2: S > O > N), simply changing the solvent or proper employing intramolecular exchange process enables the control of crystallization of perovskite.[46, 47] Various additives have been employed to alter the crystallization by tuning the precursor, forming intermediate phase during the film formation, reacting with perovskite composition, interacting with perovskite via chemical bonds, or tailoring the contact between perovskite and substrate.[48, 49]

Tuning the colloid distribution in perovskite precursor solution is an effective strategy to control the crystallization. The colloid distribution in a precursor is crucial for the film quality due to its role as nucleation sites for perovskite, which is easily influenced by the aging time and heating of solution.[50-52] Acids (such as HI, HBr, HCl, and NH_3SO_3) have been added into perovskite precursors to induce small colloids with uniform distribution, thereby slowing the crystallization process due to the reduced nucleation sites.[52-55] Most additives are based on the coordination chemistry to modify the crystallinity of perovskites. It has also been reported that the acid additives induce the hydrolysis of DMF and produce dimethylamine to assist the dissolution of colloids.[52]

Another strategy to modulate the perovskite morphology is via coordination effects. Organic molecular additives with functional groups composed of lone pairs electrons can interact with Pb^{2+} to slow down the crystallization process, enhancing the crystallinity of the perovskite film. Various polar solvents have been used as additives to modify the crystallization).[56-59] Molecules with halogen, carbonyl group, sulfonate group, or nitrogen atoms are also widely used to slow down the crystallization of perovskite by forming Lewis acid-base adduct

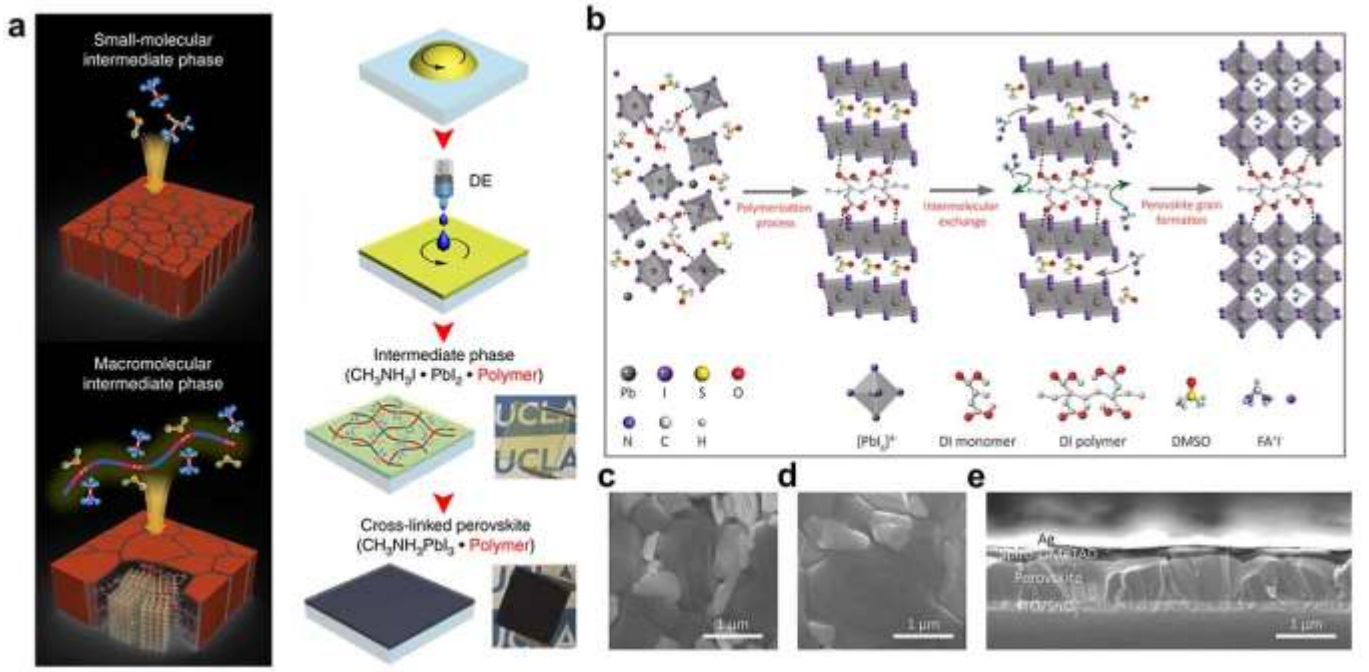

Fig. 7 (a) Schematic diagram of the perovskite crystallization induced by small molecular and macromolecular intermediate phase. Reproduced from ref 74 with permission from Springer Nature Limited, copyright 2019. (b) Schematic illustration of the polymerization-assisted grain growth (PAGG) strategy. Top-view SEM images of perovskite film without (c) and with (d) PAGG. Cross sectional SEM image of perovskite solar cell with PAGG. Reproduced from Ref 75 with permission from Wiley-VCH, copyright 2020.

intermediate phases.[60-65] Some small molecules containing donor groups were employed to modulate the crystallization process of perovskites and remain in the perovskite films after crystallization. For example, Zhou *et al.* employed 4-(1H-imidazol-3-ium-3-yl)butane-1-sulfonate (IMS) in perovskite precursor to alter the crystal orientation of $MAPbI_3$ film. The oxygen atom of sulfonate group within IMS can coordinate with which Pb^{2+} ions and form $MAPbI_3$–IMS intermediate phase before annealing, which slowed down the crystallization process and enabled the ordered grain growth.[61]

Although some additives are left in the perovskite film after annealing to passivate the defects, most additives should be removed after the film formation via volatilization or solvent extraction to avoid doping effects, especially for the insulating ones. Therefore, volatile additives are preferably employed in perovskite film formation. MAAc, $Pb(SCN)_2$ and MACl have been reported as effective additives to induce large perovskite grains.[57, 66, 67] The mechanism can be attributed to the formation of intermediate phase and/or the lowering of perovskite formation energy, which enables the reduced nucleation density and the growth of larger perovskite grains. It worthy to note that MACl has become an essential additive to fabricate ultra-high performance $FAPbI_3$-based PVSCs, due to their effectiveness in altering the perovskite grain size.[68] Meanwhile, $Pb(SCN)_2$ has also been reported to interact with MAI to form MASCN, which is readily decomposed into volatile HSCN and MA gas, resulting in large perovskite grains.[69, 70]

Some nonvolatile ionic liquids (ILs) were employed as additive to modify the morphology of perovskite films.[71, 72] Moore et al. incorporated methylammonium formate (MAFa) as solvent in perovskite film to control the crystallinity of perovskite and produce high-quality perovskite films.[73] Differently, Seo et al. employed small amount of MAFa as additives instead of solvent in perovskite precursor to modify the crystallization. The $HCOO^-$ in MAFa could coordinate with Pb^{2+} in precursor at the early stage of crystal growth and replaced by I^- ions during the annealing process, therefore, slowing down the crystallization process and resulting in enlarged grain sizes.[63]

In addition, polymers have also been employed as heterogeneous nuclei or template to control the crystal nucleation and growth to induce high-quality perovskite films. Han et al. introduced a long-chain polymeric Lewis base, poly (propylene carbonate) (PPC), to accomplish an inter-grain cross-linking of perovskite (Fig. 7a).[74] Due to the strong Lewis acid–base adduct induced by the interaction of carbonate groups with perovskite and the enlarged grain size, the PCE was raised from 17.88% to 20.06% with outstanding stability owing to the hydrophobic nature of PCC. Similarly, Zhao *et al.* introduced a polymerization-assisted grain growth (PAGG) strategy by incorporating small monomers, dimethyl itaconate (DI), in the PbI_2 solution in the sequential deposition of perovskite (Fig. 7b). The monomers were polymerized during the thermal annealing of PbI_2 film, with the bulkier polymer located at grain boundaries. The strong interaction between PbI_2 and polymer causes higher energy barrier to form perovskite crystals during the second step reaction, contributing to improved morphology and enlarged grain size from 0.75 μm to 1.25 μm (Fig. 7c-e). A remarkable efficiency of 23% was achieved along with superior stability.[75]

2.1.3.2. Sequential solution deposition method. Sequential solution deposition provides superior control over the reaction of perovskite precursors and the crystallization of perovskite

materials, which is conducive to the formation of high-quality perovskite thin films with high surface coverage. The metal halides with layered crystal structures provide a three-dimensional framework for the intercalation of organic or cesium cations. For the traditional sequential deposition method, metal halides are firstly deposited on the mesoporous scaffold, then, react with the organic-ammonium halides to form perovskites within a few seconds by immersing the substrate in the organic-ammonium halide solution. However, in the inverted perovskite devices with planar structures, due to the lack of mesoporous scaffolds, metal halides are prone to form dense films, resulting in an inadequate reaction between the perovskite precursors, and thus the residue of metal halides in the final perovskite films. The residual metal halides in inverted devices can reduce light-trapping ability and increase charge carrier transport resistance. Therefore, compared to the one-step solution deposition method, the key of sequential solution deposition method is to control the crystallization of metal halides and to achieve complete reaction between metal halides and organic-ammonium halides.

Solvent engineering by applying DMSO instead of the commonly used DMF to dissolve metal halides is demonstrated an effective approach to modulate the crystallization of metal halides. The coordination ratios between Pb and the solvents (DMF and DMSO) are 1:1 and 1:2, and the Pb-O bond lengths for DMF and DMSO are 2.431Å and 2.386Å, respectively, suggesting that DMSO has stronger coordination with PbI_2 compared to that of DMF. The strong interaction between Pb^{2+} and DMSO can slow down the crystallization rate of PbI_2, thus forming a uniform and amorphous PbI_2 film.[76]

For achieving the complete reaction of perovskite precursors, the interdiffusion approach is applied to fabricate perovskite thin films in an inverted planar configuration. Basically, organohalide is spin-coated on the top of metal halide layer to form a stacked film. Driven by thermal annealing, metal halides and organic-ammonium halides are diffused together and reacted with each other to form perovskites. The complete conversion of the two precursor materials could be achieved by precisely controlling the film deposition thickness. Huang *et al.* developed the interdiffusion method to fabricate $MAPbI_3$ thin films at the early stage of perovskite photovoltaics.[77] Attributed to this method, the morphology of MA-based perovskite film shows obviously improvement, and the FF of perovskite devices increases significantly.

In addition to optimizinging the deposition method, the construction of mesoporous metal halide films is also an effective way to promote the conversion of metal halide to perovskite. For depositing $MAPbI_3$, the porous PbI_2 scaffold provides voids that serve as channels for the effective penetration of MAI into PbI_2. These voids can also provide space for crystal expansion to reduce the lattice strain during the perovskite growth. The porosity of PbI_2 film can be adjusted by controlling the solvent evaporation rate of the solvent to optimize the photovoltaic performance of the devices. Choy *et al.* developed a self-assembled porous PbI_2 structure by incorporating small amount of 4-tert-butylpyridine (TBP) additive into the PbI_2 precursor solutions, which significantly promoted the conversion of perovskite without any PbI_2 residue.[78]

2.1.3.3. Vacuum deposition method. Vacuum deposition methods are usually carried out in a vacuum chamber and perovskite precursors can be thermal-evaporated simultaneously or sequentially to deposit on the substrate. The perovskite precursors react initially during the deposition, and undergo thermal annealing to promote crystal growth. Regardless of the surface wettability of the substrate, the vacuum deposition technique ensures the preparation of a high-quality perovskite thin film. One of the main advantages of vacuum deposition method is that the perovskite film thickness can be precisely modulated as required, which provides the feasibility to study the relationship between the film parameters and the device performances. For instance, Bolink *et al.* applied the vacuum deposition method to prepare both n-i-p and p-i-n architectures, allowing direct comparison of these two designs.[79] The average PCEs of p-i-n and n-i-p structures are 15% and 18%, respectively, making the vacuum-deposited PVSCs closer to their solution-processed equivalents. Another advantage of the vacuum deposition method is conductive to the fabrication of large area perovskite photovoltaic modules. Although the vacuum deposition method provides a simple and more reproducible way to fabricate compact and uniform perovskite films, more attention still needs to be paid to find better solution processing methods, since they can offer diverse alternatives to prepare PVSCs via more cost-effective and high-throughput approaches.

2.1.4 Defects passivation of perovskite films.

The non-radiative recombination in the bulk and on the surface of perovskite films cause devastating effects on device performance and stability. In perovskites, nonradiative recombination mainly refers to Shockley-Read-Hall (SRH) trap-assisted recombination as Auger recombination is not dominant and can be neglected.[80-82] The SRH non-radiative recombination is induced by defects, which can be effectively suppressed by defect passivation. As introduced above, deep-level defects have high formation energies and serve as non-radiative recombination centers and shallow-level defects have low formation energies and are not considered as SRH recombination centers, but they can cause unintentional doping due to their charged nature. A large number of shallow-level defects will accelerate ion migration and cause instability. Therefore, it is equally important to passivate both shallow- and deep-level defects.[13]

Lewis acids and Lewis bases, as electron acceptors or donors, are often employed to passivate negatively and positively charged defects, respectively. Fullerene and its derivatives are representative Lewis acid commonly used to passivate the negative defects (such as under-coordinated halide ions and Pb–I antisites) due to their superior electron accept ability.[83-85] Xu *et al.* and Chiang *et al.* have separately proved that the incorporation of PCBM at grain boundaries is beneficial for passivating defects, the trap density could be reduced and carrier lifetime could be prolonged, resulting in

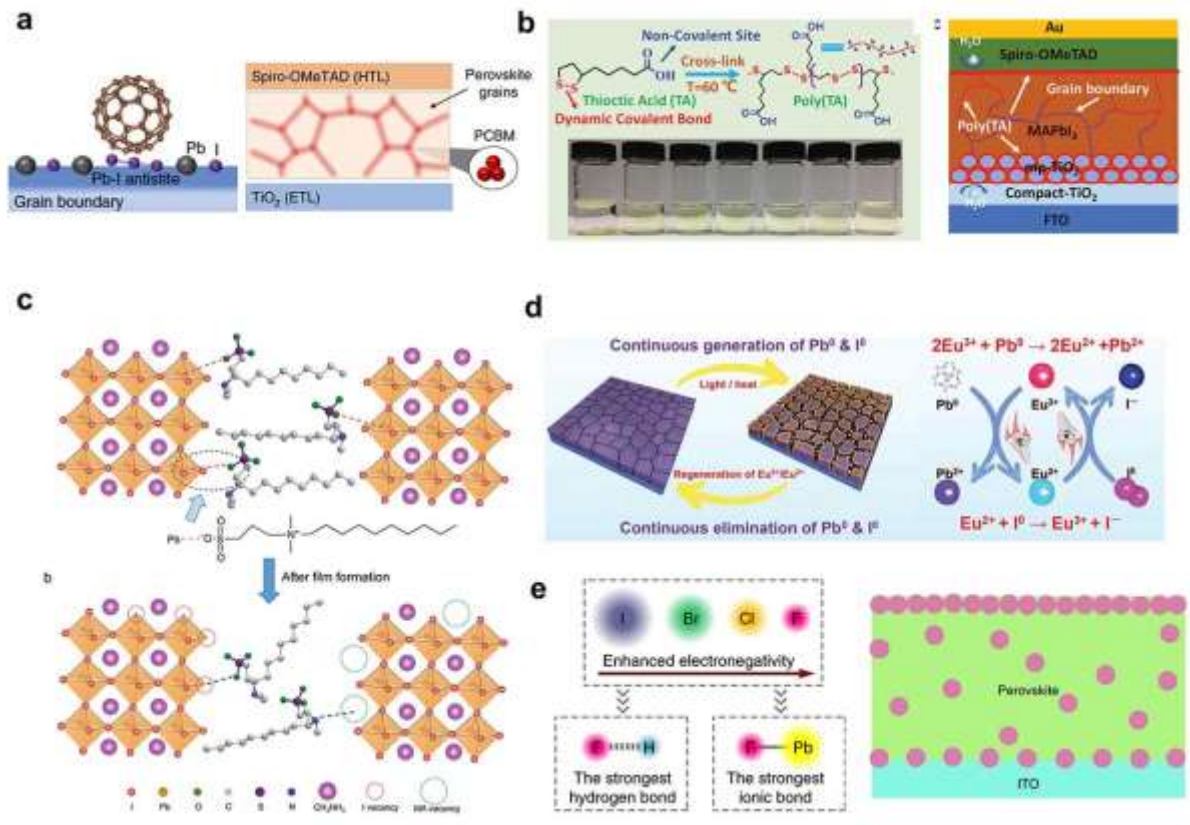

Fig. 8 (a) Schematic of the passivation effects by PCBM. Reproduced from ref 86 with permission from Macmillan Publishers Limited, copyright 2015. (b) Scheme of crosslinking polymerization process of TA under thermal conditions and device structure with Poly TA. The photographs display TA dissolved in different solvents. Reproduced from ref 90 with permission from Wiley-VCH, copyright 2019. (c) Scheme of DPSI mediated perovskite growth and defect passivation. Reproduced from ref 99 with permission from Wiley-VCH., copyright 2018. (d) Possible mechanism of cyclically reduction of Pb^0 and I^0 defects and regeneration of Eu^{3+}-Eu^{2+} metal ion pair. Reproduced from ref 103 with permission from The American Association for the Advancement of Science, copyright 2019. (e) Scheme of the hydrogen bond between the halogen and MA/FA ions and strengthening the ionic bond between the halogen and metal ions, and scheme of the potential position of NaF in the perovskite films. Reproduced from ref 104 with permission from Springer Nature, copyright 2019.

enhanced carrier lifetime (Fig. 8a).[86, 87] Another kind of Lewis acid passivator is fluoro-containing molecules, in which the strong electronegative fluoro atoms induce a positive charge on the other side of the molecule, providing the molecule with electron-accepting ability. For example, Iodopentafluorobenzene (IPFB) was employed by Abate *et al.* to passivate the under-coordinated halide ions by constructing strong halogen bonding. The supramolecular halogen bond complexation between the Iodopentafluorobenzene (IPFB) and perovskite enables reduced trap density and longer carrier diffusion lengths.[88]

Lewis base with N, O, S, P atoms as electron donors (such as pyridine and thiophene) can be used to passivate the positively charged defects such as under-coordinated Pb^{2+}. For instance, thiophene and pyridine have been reported to sufficiently passivate perovskite film through their coordination with uncoordinated Pb^{2+}. Jung *et al.* have employed a Lewis base molecule, hexamethylphosphoramide (HMPA) with three nitrogen atoms and one oxygen atom as donor, to efficiently coordinate with under-coordinated Pb^{2+}, which not only could modify the crystallization process, but also passivate defects.[58] DeQuilettes *et al.* have reported the use of trioctylphosphine oxide (TOPO) to passivate the defects at grain boundaries of perovskite, the reduced trap density contributes to prolonged carrier lifetime and enhanced photoluminescence quantum yield (PLQY).[89] Recently, Chen *et al.* incorporated a monomer, thioctic acid (TA), at both the perovskite/TiO_2 interface and the bulk of perovskite. TA is crosslinkable at low-temperature, resulting in crosslinked Poly(TA) both at the interface and grain boundaries, which can passivate the defects of TiO_2 and perovskite via the interaction between the -COOH and -C-S groups in Poly(TA) and under-coordinated lead in perovskite as well as the Ti^{4+} in TiO_2, leading to a champion PCE of 20.4% (Fig. 8b).[90] Yang *et al.* designed a small molecule named as D4TBP, which contains 4-tert-butylphenyl, amine, and carboxyl groups, to effectively passivate different kinds of defects in perovskites, leading to a high V_{OC} of 1.23 V with a low potential loss of 0.34V.[91] Yang *et al.* have also employed octylammonium sulfate to treat the surface of CsFAMA perovskite.[92] The *in-situ* reaction between SO_4^{2-} and Pb^{2+} led to the formation of water insoluble lead (II) oxysalts, which not only effectively passivated the defects in grain boundaries, but also endowed perovskite with better resistance to water. Consequently, the efficiency of device was improved from ~ 18% to > 21% with better stability. Apart from the use of single component Lewis acid or Lewis base as passivators, the synergistic effects of them are also

investigated. Zhang *et al.* have simultaneously employed bis-PCBM mixed isomers as the Lewis acid in the antisolvent and N-(4-bromophenyl)thiourea (BrPh-ThR) as the Lewis base in the perovskite precursor to passivate Pb^{2+} and PbX_3 antisite defects, meanwhile, improving the perovskite film quality.[93]

Ionic bonds between perovskites and passivators can also be used for defects passivation. Alkylammonium halogen salts have become very popular passivators due to their effectiveness in enhancing device performance. Such materials can passivate both the positively and negatively charged defects via hydrogen bonding and ionic bonds. Zhao *et al.* have systematically investigated the passivation effect of different diammonium salts ($NH_3I(CH_2)_4NH_3I$ (C4), $NH_3I(CH_2)_8NH_3I$ (C8), and $NH_3I(CH_2)_2O(CH_2)_2NH_3I$ (EDBE)) by a simple post-treatment process.[94] They found that the anti-gauche isomerization in C8 necessitates an additional energy barrier for the phase transformation from 3D perovskite to 2D perovskite. This means that C8 would stay on the surface of 3D perovskite to efficiently passivate defects on the surface and at the grain boundaries, while C4 and EDBE didn't show the same effect. Jiang *et al.* have adopted phenylethylamine (PEA) on FA/MA mixed-cation perovskite films to passivate surface defects, resulting in a PCE of 23.32%.[95] They pointed out that PEA can passivate the iodide vacancies only when there was no annealing post treatment as annealing caused the formation of 2D perovskite. Lately, Li *et al.* have employed phenylethylamine chloride (PEACl) to passivate the surface defects of 1.75 eV wide-bandgap PVSCs. The reduced energy loss and suppressed phase segregation enable devices to have a high V_{OC} of 1.26 V with excellent stability.[96] Jen *et al.* have designed and applied a bifunctional molecule, piperazinium iodide (PI), which can simultaneously passivate the positively and negatively charged defects via its electron-donating and electron-accepting groups, achieving a high PCE of 23.37% in a p-i-n inverted device.[97]

Zwitterions have also been used for bulk defects passivation, which can simultaneously passivate both negatively charged defects and positively charged defects through the positively and negatively charged functional groups in the molecule.[98] Huang group has introduced a sulfonic zwitterion, 3-(decyldimethylammonio)-propane-sulfonate inner salt (DPSI), as an additive to modify the perovskite crystallization and passivate defects (Fig. 8c). The positively charged quaternary ammonium group and negatively charged sulfonic group in DPSI can neutralize the charged defects at the surfaces and grain boundaries, resulting in an efficiency of 21.1%.[99] Wang *et al.* have mixed a zwitterionic molecule, bethanechol chloride (BTCC), with organic salts in IPA during the sequential deposition of PVSCs, the passivation effects exerted by BTCC enable an enhanced PCE of 20.45%.[100] Zheng *et al.* have reported quaternary ammonium halides, L-α-phosphatidylcholine, choline chloride, and choline iodide, as zwitterions to passivate surface defects of perovskite. The positive charged quaternary ammonium group ($–N(CH_3)_3^+$) and negatively charged anions (phosphate and halides) can simultaneously passivate the positively and negatively charged defects. A high PCE of 21.0% was achieved with $V_{oc,deficit}$ of 0.39 V when using choline chloride as a passivator.[101] Similarly, Wang *et al.* have employed choline iodide to perform the surface passivation on all-inorganic perovskite $CsPbI_3$, and achieved a record PCE of 18.4% for all-inorganic PVSCs.[102]

Small amounts of inorganic salts can also be integrated into perovskite films to enhance the device performance and stability. Wang *et al.* have reported that the europium ion pair, Eu^{3+}-Eu^{2+}, works as the "redox shuttle" to selectively oxidize lead defects and reduce iodide defects in perovskite in a cyclical transition (Fig. 8d).[103] Li *et al.* have employed NaF as an additive to perform the passivation by forming strong hydrogen bonds (N–H···F) with organic cation (MA/FA) and strong ionic bonds with lead in the perovskite films, which simultaneously passivated both halide anion vacancies and organic cation vacancies according to the high electronegativity of fluoride (Fig. 8e). [104]

Functionalized ionic liquids (ILs) have also been employed to passivate the surface defects of perovskites. Huang *et al.* have used methyltrioctylammonium trifluoromethanesulfonate (MATS) to passivate the surface defects of p-i-n structured PVSCs. The low vapor pressure and non-volatile nature allow the IL to remain on the surface of perovskite after thermal annealing. The interaction between the $CF_3SO_3^-$ with MA^+ and Pb_6^{4-} enables effective passivation of defects.[105] Zhang *et al.* have employed 1-butyl-2,3-dimethylimidazolium chloride ([BMMIm]Cl) IL to passivate the surface defects of $CsPbBr_3$ perovskite in carbon-based hole transporting layer free PVSCs, enhancing the PCE from 6.15% to 9.92%.[106] The employment of 1-butyl-3-methylimidazolium tetrafluoroborate ($BMIMBF_4$) IL to alter the surface by Wang *et al.* has enabled the simultaneously enhanced efficiency and stability of all-inorganic PVSCs.[107] Recently, Zhu *et al.* have utilized 1,3-dimethyl-3-imidazolium hexafluorophosphate ($DMIMPF_6$) IL to passivate the surface defects of perovskite film by forming electrostatic interaction between undercoordinated Pb^{2+} ions and $DMIMPF_6$. Meanwhile, the IL can tune the interfacial electronic properties to form a favorable energy level alignment at the perovskite/HTL interface, leading to a high efficiency of 23.25%.[108]

In summary, the defects in perovskite polycrystal film can be passivated through coordinate bonding or ionic bonding, Lewis acid, Lewis base and ammonium salts. The development of multifunctional molecules that can simultaneously passivate different types of defects in perovskites will play a big role in this research field.

2.2 Heterojunction Designs for PVSCs.

As mentioned in Section 2.1.1, the heterojunction in PVSCs is crucial for charge carrier separation and the suppression of non-radiative recombination, therefore, influencing the device performance. Despite high-quality perovskite films can be obtained via the strategies in Section 2.1.3 and 2.1.4, PVSCs cannot be realized without the construction of ideal heterojunctions. In this section, we will introduce the heterojunction constructed between pristine perovskites and charge transporting layers (CTL) to provide a comprehensive understanding of heterojunction designs in PVSCs. Here, the heterojunction means the interface between two

semiconductors with unequal bandgaps. Perovskite/perovskite heterojunction, perovskite/functional layer heterojunction and perovskite/organic BHJ heterojunction will be reviewed, respectively.

2.2.1 Gradient perovskite heterojunction (perovskite/perovskite heterojunction).

At the early stage, single junction PVSC is merely composed of a layer of 3D perovskite with single component as active materials. Although the crystallization and defects density can be well controlled through aforementioned strategies, such modification cause neglectable influence on the heterojunction properties. With the development of perovskite device configurations, gradient perovskite heterojunction (or perovskite/perovskite heterojunction) has been constructed to alter the charge carrier dynamics between perovskite and charge transporting layers. Here, the perovskite/perovskite heterojunction refers to two or more kinds of perovskites with different composition/dimension, and function as the photoactive layer in PVSCs. The employment of perovskite/perovskite heterojunction can tune the energy level alignment and defects density at interfaces, therefore, affecting the device performance. In this section, we will review the recently reported perovskite/perovskite heterojunctions and briefly introduce the mechanism behind them.

2.2.1.1. Multi-composition perovskite heterojunction. The preparation of perovskite layer with multi-composition has been employed to construct perovskite/perovskite heterojunction, which can form better-matched band structure in perovskites to facilitate charge extraction and reduce energy loss from non-radiative recombination. Chemical vapor deposition (CVD) is considered as a suitable tool to construct gradient perovskites as it can avoid damage to the underlayer perovskite during the deposition. Tong *et al.* have developed a stack sequence physical-chemical vapor deposition (SS-PCVD) method to deposit perovskite with gradient compositions and bandgaps.[109] They have first prepared CsBr and $PbBr_2$ films via physical vapor deposition, followed by depositing perovskite via CVD in the FAI atmosphere (Fig. 9a). As-prepared perovskite film consists a wide E_g $CsPb_2Br_5$ perovskite at the interface of TiO_2/FA-based perovskite (Fig. 9b). $CsPb_2Br_5$ not only can suppress the non-radiative recombination, but also can form a favorable energy band alignment for charge extraction, resulting in enhanced device performance and stability.

Cation exchange reaction is another method to form graded distributed heterojunction. Wu *et al.* have constructed a perovskite graded heterostructure (GHS) by using a sequential cation exchange reaction between $FASnI_3$ perovskite and the bulky 4-(trifluoromethyl) benzyl ammonium cations ($TFBA^+$), in which the pre-deposited $FASnI_3$ film was immersed into TFBAI/chloroform solution followed by annealing. The cation

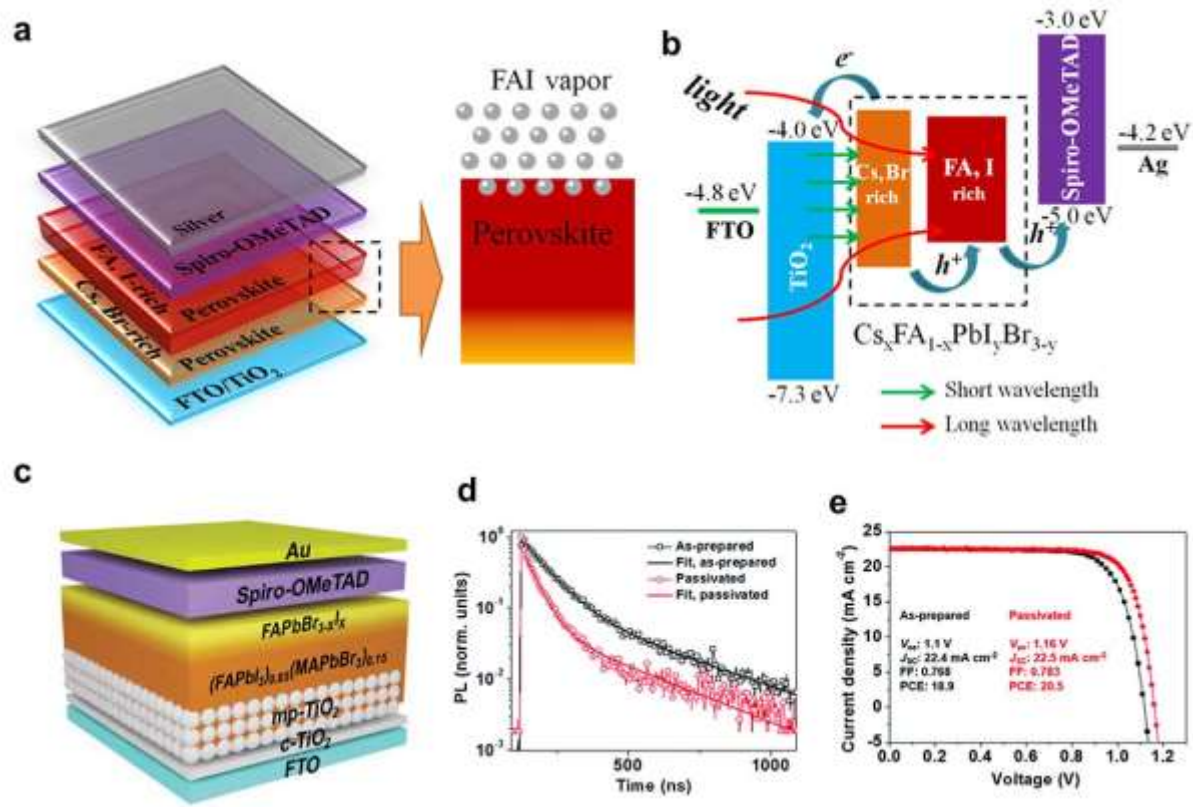

Fig. 9 (a), (b) Schematic illustration of the formation of FA-based perovskite/$CsPb_2Br_5$ ultra-thin film heterojunction, the vapor doping process and energy level alignment of the PVSCs via the SS-PCVD process. Reproduced from ref 109 with permission from Elsevier Ltd, copyright 2018. (c) Device configuration of composition gradient distributed PVSCs. (d) Time-resolved PL decays of the perovskite films with and without surface passivator. (e) *J-V* of PVSCs with and without surface passivator. Reproduced from ref 112 with permission from the Royal Society of Chemistry, copyright 2017.

exchange between FA^+ and $TFBA^+$ enables a gradiently distributed wide-E_g Sn perovskite from bulk to surface, which accelerated the carrier extraction at perovskite/ETM interface, reduced the density of trap states, and acted as an energy barrier to prevent the oxidation of Sn^{2+}, resulting in a remarkable efficiency of 11% for pure Sn-based PVSCs.[110]

Kim *et al.* have deposited perovskite with gradient Br concentration by treating $MAPbI_3$ with vaporized hydrobromic. HBr can be oxidized by O_2 to convert into Br_2, which substitutes I^- with Br^-. The various diffusion rates into different thicknesses of perovskites resulted in a gradient distribution, causing a graded band structure and enhanced device performance.[111] Cho *et al.* have constructed a $FAPbBr_{3-x}I_x$ layer on top of the pristine $(FAPbI_3)_{0.85}(MAPbBr_3)_{0.15}$ film by simply spin-coating a FABr layer onto the pristine film with excess PbI_2. The FABr reacted with PbI_2 to form graded distributed wide-E_g perovskite from bulk to surface (Fig. 9c). The optimized band structure resulted in a prolonged carrier lifetime and a PCE of 21.3% (Fig. 9d, e) .[112]

Ion diffusion can also result in a gradient distribution of perovskite compositions. Liu group has deposited a low-cost lanthanide halide, $SmBr_3$ before the preparation of perovskite film. $SmBr_3$ can diffuse into perovskite and dope it to form a gradient energy band structure, which facilitates effective charge extraction and suppresses non-radiative recombination, resulting in a high PCE of 10.88% for $CsPbI_2Br$-based PVSCs.[113] Different from the diffusion method, Qiao *et al.* have directly added the "intolerant" trivalent metal cations, Sb^{3+} and In^{3+}, into perovskite precursor. Dopants spontaneously separated and located at the interfaces of perovskite/TiO_2 and Ag/spiro-OMeTAD, owing to the dissimilar cation sizes and charge states, resulting in graded energy band alignment between perovskite and ETL and contributing to a PCE over 21%.[114]

2.2.1.2. Multi-dimensional perovskite heterojunction. Low-dimensional perovskites (2D, quasi-2D, 1D or 0D perovskites) have attracted significant attention of researchers because of their excellent stability owing to their hydrophobicity and superior thermal stability.[39] Nevertheless, their large bandgaps, anisotropic charge transport and large exciton binding energies result in lower PCEs which strongly limits their potential as active material for photovoltaic applications. Combining low-dimensional perovskites with 3D perovskites to form 3D perovskite/low-dimensional perovskite heterojunction has been widely reported as an effective strategy to resolve the stability problems of PVSCs and enhance device performance due to improved charge transfer through the heterojunction. Such heterojunctions can either be formed through the direct use of 3D perovskite precursor solution to react with low-dimensional perovskite additives or constructed by the post-treatment of perovskite films, with the former results in bulk heterojunction and the latter leads to planar heterojunction. Usually, low dimensional perovskites not only can modulate the crystallization through their functional groups on large cations, but also can passivate defects at grain boundaries and facilitate the charge transfer through the favorable energy level alignment. The planar heterojunction will dramatically reduce the surface defects of perovskite, however, the formation of low-dimensional layers is challenging since the 3D perovskites should be intact after the film preparation. In this section, we will introduce i) bulk and ii) planar 3D/low-dimensional perovskites heterojunction respectively, and briefly review their merits and challenges.

i) 3D/low dimensional perovskites bulk heterojunction. Incorporating a small amount of low-dimensional perovskites to grow along the grain boundary in 3D perovskites can effectively passivate defects at the grain boundaries and potentially modulate the crystallization of 3D perovskites to enable enhanced device performance and stability. As low-dimensional perovskites have high exciton binding energy, the amount of loaded low-dimensional perovskites and their compositions are critical, therefore should be carefully considered. To simultaneously obtain high efficiency and stability, a delicate balance of the 2D and 3D perovskite compositions and their structural configurations is required so that the optimum contribution from each perovskite phase can be achieved.

Normally, a small amount of excess PbI_2 can be used in the precursor to form an intrinsic heterointerface at perovskite films for fabricating high-performance PVSCs. Recently, Rothmann *et al.* have employed atomic-resolution transmission

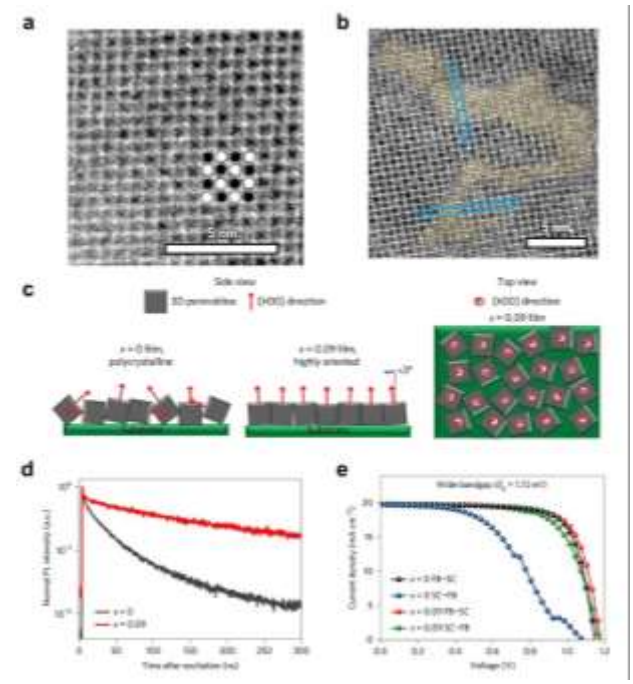

Fig. 10 Atomic-resolution STEM images of (a) checkered intensity pattern formed upon electron beam exposure with ~200 e $Å^{-2}$ for $FAPbI_3$ perovskite and (b) native intergrowth between PbI_2 (shaded yellow) and $FAPbI_3$ within the perovskite film. Reproduced from ref 115 with permission from the American Association for the Advancement of Science, copyright 2020. (c) Scheme of a preferential orientation for the [h00] direction to align out-of-plane and no preferential orientation within the plane of 2D/3D perovskite. (d) Time-resolved PL spectra for 3D perovskite film with and without 2D perovskite. (e) *J–V* curves for PVSCs using large-bandgap $FA_{0.83}Cs_{0.17}Pb(I_{0.6}Br_{0.4})_3$ (x = 0) and $BA_{0.09}(FA_{0.83}Cs_{0.17})_{0.91}Pb(I_{0.6}Br_{0.4})_3$ (x = 0.09) perovskite. Reproduced from ref 116 with permission from Macmillan Publishers Limited, part of Springer Nature, copyright 2017.

electron microscopy to investigate the microstructure of perovskites.[115] They have observed a perfect crystallographic alignment between the PbI_2 and $FAPbI_3$ perovskite at the material heterointerface between excess PbI_2 and the $FAPbI_3$ grains with undetectable lattice misfit (Fig. 10a, b), without creating any detrimental effect to device performance.

The advantage of using mixed 3D/low-dimensional perovskite heterojunction is the device performance can be improved through enhanced crystallinity, passivated defects, and better energy level alignment. At the early stage, Snaith *et al.* found that the introduction of n-butylammonium (BA) cations into $FA_{0.83}Cs_{0.17}Pb(I_yBr_{1-y})_3$ perovskite will form two-dimensional perovskites dispersed within the 3D perovskite film to attain enhanced performance.[116] The 3D perovskite showed a preferential orientation for the [100] direction (Fig. 10c). With the plate-like 2D-phase perovskite standing up between the 3D perovskite grains, the crystallization was enhanced, and the grain boundaries were passivated, resulting in enhanced carrier lifetime and device performance (Fig. 10d, e). Lee *et al.* have added a small amount of PEA^+ into 3D perovskite precursor to afford modified morphology and passivated grain boundaries to result in enhanced device performance and stability. They found that the addition of PEAI led to the formation of quasi-2D perovskite near the perovskite/TiO_2 interface. This formation of preferred orientation of quasi-2D perovskites might be due to the hydrogen bonding between the amino group in PEAI and TiO_2, indicating that the interfacial materials can affect the formation of quasi-2D/3D perovskite heterojunction. The quasi-2D perovskites not only promote the crystallization of perovskite but also result in a more preferred orientation at (110) plane. Meanwhile, the quasi-2D perovskites at grain boundaries effectively passivate defects, leading to much improved device performance.[117] Grancini *et al.* have incorporated 3 mol% of aminovaleric acid iodide (AVAI) in $MAPbI_3$ perovskite via directly mixing (AVAI:PbI_2) with $MAPbI_3$ precursor to induce 2D/3D structure. The 3D perovskite exhibited preferred orientation along the <hk0> direction with 2D perovskite additives, meanwhile, an electron recombination barrier was formed due to the lower CBM of 2D perovskites. Fabricated carbon-based perovskite solar modules showed high PCE of 11.2% with excellent stability of over 10,000 h under one sun illumination.[118] Yao *et al.* incorporated β-guanidinopropionic acid (β-GUA) into an MA-free $FA_{0.95}Cs_{0.05}PbI_3$ perovskite to induce 2D/3D heterostructure. The quasi-2D perovskite showed face-on orientation at the grain boundaries, the three amine groups on the same molecule enable β-GUA based quasi-2D perovskite to be effective in passivating defects via the coordination of nitrogen atoms with under-coordinated lead, resulting in suppressed non-radiative recombination and reduced energy losses.[119] Recently, Liu *et al.* developed a class of aromatic formamidiniums as organic spacers in 2D/3D perovskites, which facilitated better crystal growth and orientation, reduced defect density, enhanced the carrier lifetime, contributing to a champion PCE of 23.36%.[120]

1D perovskites, which are 1D quantum confined materials that show unique optical and electrical properties due to the intense quantum confinement, were also used to assemble heterojunctions with 3D perovskites. Liu *et al.* utilized 1D-$Tpy_2Pb_3I_6$ and 2D-$TpyPb_3I_6$ (Tpy; terpyridine) perovskites to assemble 1D/2D/3D heterojunction with 3D all-inorganic perovskites. The incorporation of low-dimensional perovskites is beneficial to release residual strain, and form effective charge transport channels, resulting in an enhanced PCE of 16.1%. Benefitted by the hydrophobicity of low-dimensional perovskites, the stability of $CsPbI_2Br$-based PVSCs under humidity was greatly enhanced with unencapsulated devices stable in ambient environment for over 1000 h.[121]

Another merit of 3D/low-dimensional perovskites is the greatly enhanced long-term stability, mainly due to the intrinsic hydrophobicity and thermal stability of low-dimensional perovskites, as well as the capability to block ion migration. Zhang *et al.* incorporated small amount of bicationic 2D perovskite of $EDAPbI_4$ (EDA: ethylenediamine) into 3D $CsPbI_3$ perovskite precursor. The two terminal NH_3^+ group in 2D perovskite can crosslink the 3D grains to stabilize the cubic phase $CsPbI_3$. Excellent long-term stability could be achieved under humid and thermal conditions.[122] Niu *et al.* also employed n-butylammonium (BA)-based 2D perovskites to form a 2D/3D ($FAPbI_3$) heterostructure to enhance the device longevity. Ruddlesden–Popper (RP) phase perovskites were interspersed at 3D grain boundaries, resulting in more stable black phase perovskite and higher hydrophobicity, leading to superior long-term stability with a T_{80} lifetime over 2880 h for unencapsulated devices under ambient conditions (40% RH, 25°C).[123] Ruggeri *et al.* incorporated PEAI into Sn-Pb 3D perovskites with NH_4SCN as additive to alter the crystallization. The addition of NH_4SCN slows down the nucleation and crystallization of 3D perovskite and homogenize the crystal structure as they can bind to the early colloids in precursor. As-prepared 2D perovskites mainly exist on the surface and at grain boundaries of 3D perovskites, leading to the enhancement of ambient stability of Sn-Pb PVSCs.[124]

3D/1D perovskites have also been reported to enhance device longevity. 3 mol% aliphatic fluorinated amphiphilic additive, 1,1,1-trifluoro-ethyl ammonium iodide (FEAI), has been incorporated into 3D perovskite to form the 3D/1D heterostructure. The 1D perovskite was formed due to the larger size of fluoro group in FEAI than hydrogen, increasing the tolerance factor to 1.09. The addition of FEAI resulted in more hydrophobic perovskite films and more stable PVSCs due to the hydrophobicity of fluoro alkyl group.[125] Fan *et al.* introduced 2-(1H-pyrazol-1-yl)pyridine (PZPY) into 3D perovskites to form thermodynamically self-healing 1D/3D hybrid PVSCs. The result from high-resolution transmission electron microscopy (HRTEM) confirmed the existence of heterostructure between 1D FAI-PbI_2-PZPY and 3D $Cs_{0.04}MA_{0.16}FA_{0.8}PbI_{0.85}Br_{0.15}$ perovskites. On the one hand, the 1D perovskites enhance the hydrophobicity of film and function as a barrier to suppress the moisture permeation. On the other hand, they can block the ion migration of A-site ions and passivate defects, enabling excellent performance and stability to be realized for the fabricated devices.[126] Liu *et al.* developed a new type of 1D/3D perovskites by introducing 1D PbI_2- bipyridine BPy into the 3D perovskite solution. The resulting 1D/3D perovskites showed

superior long-term operational stability in the humid environment under external applied electric field.[127]

As reviewed above, 3D/low dimensional perovskites bulk heterojunction is an effective way to improve the efficiency and stability of PVSCs. To construct state-of-the-art bulk heterojunctions, several issues should be considered. First, since low-dimensional perovskites usually have high exciton binding energy, the amounts of low-dimensional perovskites should be controlled carefully in order to achieve high charge transfer efficiency. The functionalization of organic cations in low-dimensional perovskites can potentially lower their binding energy. Second, the orientation and crystallization of low-dimensional perovskites should be altered to ensure efficient charge transfer towards electrodes. Third, the employment of suitable organic cations that can passivate defects of 3D perovskites is beneficial for suppressing non-radiative recombination, resulting in enhanced device performance. Fourth, it is important to explore suitable organic cations that possess supramolecular interactive forces, such as hydrogen bonding or metal-organic coordination can potentially enhance the stability of devices.

ii) 3D/low dimensional perovskites planar heterojunction. *3D*/low dimensional perovskites planar heterojunction is also a facile and effective strategy for enhancing the performance and stability of PVSCs. Unlike the bulk heterojunction, most 3D/low dimensional perovskite planar heterojunctions are constructed based on using a low-dimensional perovskite layer on/under 3D perovskites. Different from the bulk heterojunction, such layer

Table 1 Summary of reported 3D/low-dimensional planar heterojunction perovskite solar cells.

Perovskite	Device structure	PCE (%)	Ref
$MAPbI_3/PEA_2Pb_2I_4$	FTO/NiO_x/perovskite/PCBM-PN4N/Ag	19.89%	128
$MAPbI_3/PEA_2Pb_2I_4$	FTO/TiO_2/perovskite/Spiro-OMeTAD/Au	18.51%	134
$(AVA)_2PbI_4/MAPbI_3$	$FTO/TiO_2/ZrO_2$/perovskite/carbon	12.9%	135
$FASnI_3/(PEA)_2(FA)_{n-1}Sn_nI_{3n+1}$	ITO/PEDOT:PSS/perovskite/C_{60}/BCP/Ag	6.98%	136
$MAPbI_3/(AVA)_2PbI_4$	FTO/TiO_2/perovskite/Spiro-OMeTAD/Au	18.0%	137
$PEA_2MA_{n-1}PbnI_{3n+1}/MAPbI_3$	FTO/TiO_2/perovskite/Spiro-OMeTAD/Ag	19.10%	138
$Cs_{0.1}FA_{0.74}MA_{0.13}PbI_{2.48}Br_{0.39}/PEA_2Pb_2I_4$	FTO/TiO_2/perovskite/Spiro-OMeTAD/Au	20.10%	139
$PEA_2FASn_2I_7/PEA_2SnI_4/FASnI_3$	ITO/NiO_x/perovskite/PCBM/BCP/Ag	9.41%	129
$Cs_{0.17}FA_{0.83}Pb(I_{0.6}Br_{0.4})_3/BA_y(Cs_xFA_{1-x})_{1-y}Pb_2(Br_{0.4}I_{0.6})_7$	ITO/SnO_2/perovskite/Spiro-OMeTAD/Au	19.4%	140
$MAPbI_3/(BA)_2(MA)_{n-1}Pb_nI_{3n+1}$	$FTO/TiO_2/C_{60}$/perovskite/Spiro-OMeTAD/Au	16.50%	141
$MAPbI_3$-$(BA)_2(MA)_{n-1}Pb_nI_{3n+1}$	FTO/TiO_2/perovskite/Au	16.13%	142
$(CsPbI_3)_x(FAPbI_3)_y(MAPbBr_3)_{1-x-y}$/ $PEA_2Pb_2I_4$	ITO/PTAA/Perovskite/PCBM/ZnO/Ag	21.31%	143
$(CsPbI_3)_x(FAPbI_3)_y(MAPbBr_3)_{1-x-y}/(PNA)_2FA_{n-1}Pb_nI3_{n+1}$	ITO/SnO_2/perovskite/Spiro-OMeTAD/Ag	22.62%	144

has neglectable influence on the crystallization of 3D perovskites, but plays the role of passivating the surface defects and modifying the energy level alignment to enhance device performance. The superior stability of low-dimensional capping layer can also serve as a protection layer to improve the stability. A summary of high-performance 3D/low-dimensional perovskite planar heterojunction based PVSCs reported as shown in Table 1.

3D/2D perovskite planar heterojunction is the most reported dimensional planar heterojunction. Bai *et al.* have applied 2D/3D PVSCs in an inverted PVSC architecture by dripping the solution of phenethylammonium iodide (PEAI) onto the surface of 3D perovskite to realize a PCE of 19.89%.[128] Mixed-cation devices with a PCE of 21.7% have also been realized when bulky iso-butylammonium iodide (iBAI) and FAI were used by Cho *et al.* to modify the surface of bulk $(FAPbI_3)_{0.85}(MAPbBr_3)_{0.15}$.[118] Ning *et al.* have realized an improved efficiency of 9.41% for Sn-based 2D/3D PVSCs by using a 2D-quasi-2D-3D hierarchy structure. [129]

Lately, Zhang *et al.* have replaced the organic hole-transporting material (HTM) with p-type 2D perovskites to carry out a graded band structure (Fig. 11a, b).[130] 2D perovskites on the surface exhibit a larger bandgap and higher valence band maximum (VBM) to form an energy panel for efficient hole extraction, resulting in a PCE of 16.13% for HTM-free PVSCs (Fig. 11c). Liu *et al.* have adopted pentafluorophenylethylammonium (FEA) as a fluoroarene cation to organize a thin 2D perovskite layer on the surface of 3D perovskites via a simple immersing method.[131] The perfluorinated benzene moiety provides the space layer with hydrophobic property to prevent the perovskite from being damaged in ambient environment. Both enhanced PCE (from 20.6% to 22.2%) and stability were obtained in unencapsulated devices, indicating the superior function of 2D interfacial layer.[131] Zhou *et al.* have adopted 2-thiophenemethylammonium (ThMA) as the spacer cation for preparing bulk 2D/3D PVSCs (Fig. 11d, e).[132] The VBM and CBM of the 2D/3D perovskites match well with HTM and ETM,[51] facilitating efficient charge transport. Furthermore, the incorporation of 2D spacer cation optimizes the crystal growth and orientation, alleviates the undesirable ion motion, and facilitates better charge extraction and device stability. The champion 2D/3D PVSC showed a PCE of 21.49% with improved stability under continuous light soaking compared to 3D PVSC (Fig. 11f). Recently, Jang *et al.* employed a solid-state in-plane growth (SIG) method to grow a stable and highly crystalline 2D perovskite film on 3D perovskites, in which solid-state 2D perovskites film was firstly stacked on 3D perovskite film, followed by applying heat and pressure to induce the formation of a new 2D film. The SIG strategy avoids the formation of unintended perovskite phase, meanwhile, can control the final thickness of 2D perovskites. Constructed 2D/3D heterojunction greatly enhanced the built-in electric field and enabled a certified PCE of 24.35% for PVSCs.[133]

Recently, 2D perovskites have been deposited under 3D perovskites as interfacial layers. Wu *et al.* have incorporated large alkylammonium interlayers between perovskite and underlayer PTAA to simultaneously reduce the non-radiative recombination loss on top and bottom interfaces of the 3D perovskites, achieving high PCE of 22.31%.[145] Li *et al.* have constructed 2D/3D bottom-up structure through spin-coating a 2D perovskite precursor on PEABr. An enhanced PCE of 19.46% was achieved owing to the reduced trap states.[146]

1D perovskite has also been employed as interfacial layer to enhance the performance and stability of PVSCs. Kanatzidis *et al.* have prepared wide bandgap 1D perovskite capping layer on 3D perovskites based on thiazole ammonium (TA). As-

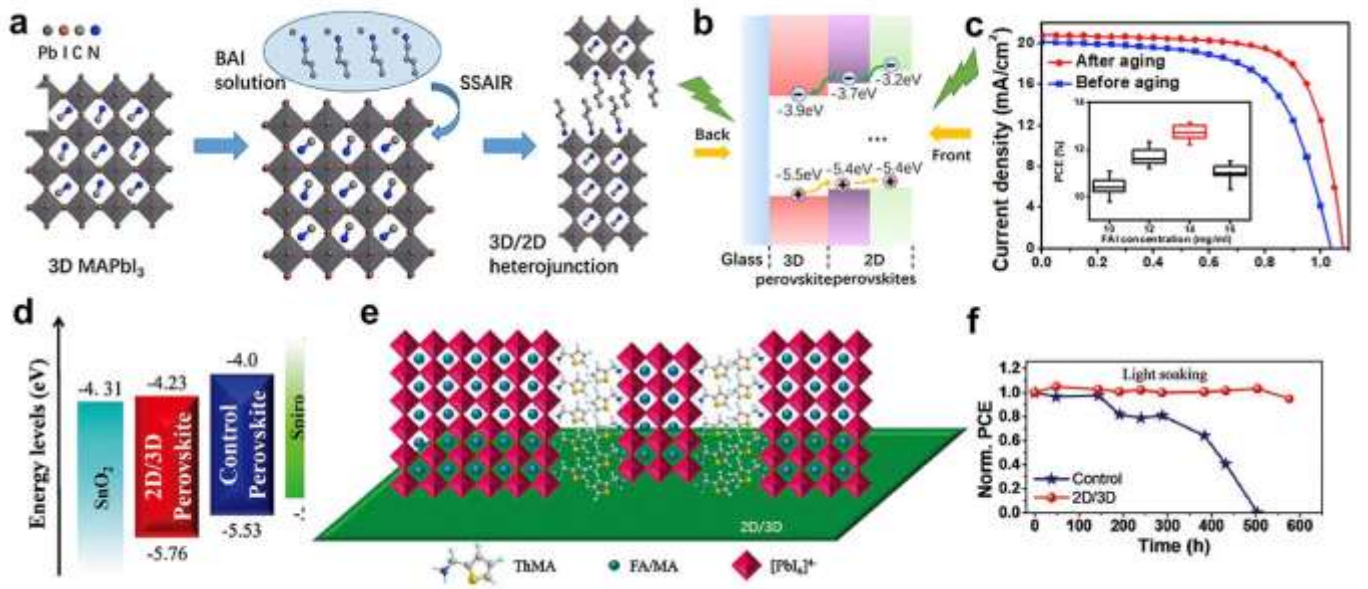

Fig. 11 2D/3D perovskite boost the performance and stability of PVSCs. (a) (b) Schematic diagram and band diagram of the growth of $MAPbI_3/(BA)_2(MA)_{n-1}Pb_nI_{3n+1}$ 2D/3D heterostructure, and (c) *J-V* curves of 3D/2D heterojunction PVSCs. Reproduced from ref 130 with permission from Elsevier Inc, copyright 2018. (d) Energy level diagram of optimized ThMA-based PVSCs with 2D/3D perovskite and 3D perovskite. (e) Scheme of the ThMA-based 2D/3D perovskite structure. (f) Stability of unencapsulated devices exposed to continuous one sun illumination in N_2. Reproduced from ref 132 with permission from Wiley-VCH, copyright 2019.

prepared 1D capping layer not only promotes the charge carrier extraction at interface, but also blocks the ion migration to enhance device stability, realizing an efficiency of 18.97% with superior stability.[147] Elsenety *et al.* have constructed a (FA/MA/Cs)$PbI_{3-x}Br_x$/$(CH_3)_3SPbI_3$ bilayer structure to effectively enhance the long-term stability.[148] Recently, Chen group has introduced a crosslinkable propargylammonium (PA^+) onto the 3D perovskite film to form a 1D/3D perovskite heterostructure. The 1D perovskite was formed by reacting PAI with excess PbI_2 on the surface of 3D perovskite. Moreover, the treatment of PA^+ released the residual strain of 3D perovskite, improving the efficiency to 21.19% with superior stability.[149]

The stability and performance of PSCs can also be improved through 0D perovskite quantum dots (QDs) owing to their similar lattice constants and compatible processing to 3D perovskite films. Cha *et al.* have deposited a layer of $MAPbBr_{3-x}I_x$ quantum dots on 3D $MAPbI_3$ perovskite, the well-matched energy level alignment promoted charge carrier extraction at the perovskite/HTM interface and enhanced device performance.[150] Que *et al.* have introduced $Cs_xFA_{1-x}PbI_3$ QDs with high x value on the surface of 3D $FAPbI_3$ perovskite. QDs not only passivated the surface defects, but also induced a better-matched energy alignment to enhance performance. In addition, the superior stability of QDs prolonged the lifetime of fabricated devices.[151] Zheng *et al.* have used oleic acid (OA) ligand-capped $CsPbBrCl_2$QDs as an antisolvent suspension to deliver molecular surface modifiers. Besides the -COOH group can bond to Pb^{2+} for passivating defects, the hydrophobic chain left on the surface can inhibit moisture penetration, which results in a high efficiency of 21.5% with excellent stability.[152] Zhang *et al.* employed amphiphilic star-like poly(acrylic acid)-block-polystyrene (PAA-b-PS) diblock copolymers as nanoreactor to template the nucleation and growth of stable and uniform $CsPbBr_xI_{3-x}$ QDs. The PS-ligated $CsPbBr_xI_{3-x}$ QDs was deposited between $MAPbI_3$ perovskite and Spiro-OMeTAD, which dramatically enhanced device performance due to the passivation of surface defects of 3D perovskites by as-prepared QDs as well as their cascade energy band alignment with perovskite and the HTL.[153] Zhang *et al.* have constructed a multigraded 3D-2D-0D (bulk-nanosheet-quantum dot) perovksite heterostructure in $CsPbI_2Br$-based PVSCs. The graded energy alignment enhanced the electric field at the interface and facilitated the carrier extraction, resulting in improved performance.[154]

Although the 3D/low-dimensional perovskites planar heterojunctions have great potential to be used for achieving high-efficiency PVSCs and overcoming stability challenges, there are several aspects that need to be considered in order to realize superior performance and stability. First, the deposition of low-dimensional perovskite must be carefully performed without damaging the 3D perovskites layer. Second, the orientation and amounts of low-dimensional perovskites should be carefully controlled to avoid impeding the charge transfer. Third, the tremendous structural diversities of low-dimensional perovskites need to be comprehensively understood in order to further improve device performance and stability. Modifying organic cations in low-dimensional perovskites with passivating capability or dipoles may be beneficial for enhancing of charge transfer and suppressing non-radiative recombination at the interface.

2.2.2 Perovskite/functional materials heterojunction.

In PVSCs, charge carrier extraction, transport, and recombination are mainly happened at the heterointerfaces. However, the trap density is concentrated on the surface as the charge transporting materials (CTMs) may also have defects, causing serious non-radiative recombination. Apart from the performance, the trap states at interfaces can also lead to poor stability and hysteresis due to ion migration. [155, 156] Therefore, to achieve high efficiency and stability, it is critical to modify the interface. In general, functional interlayers are inserted into perovskite/charge transporting layer (CTL) interfaces to

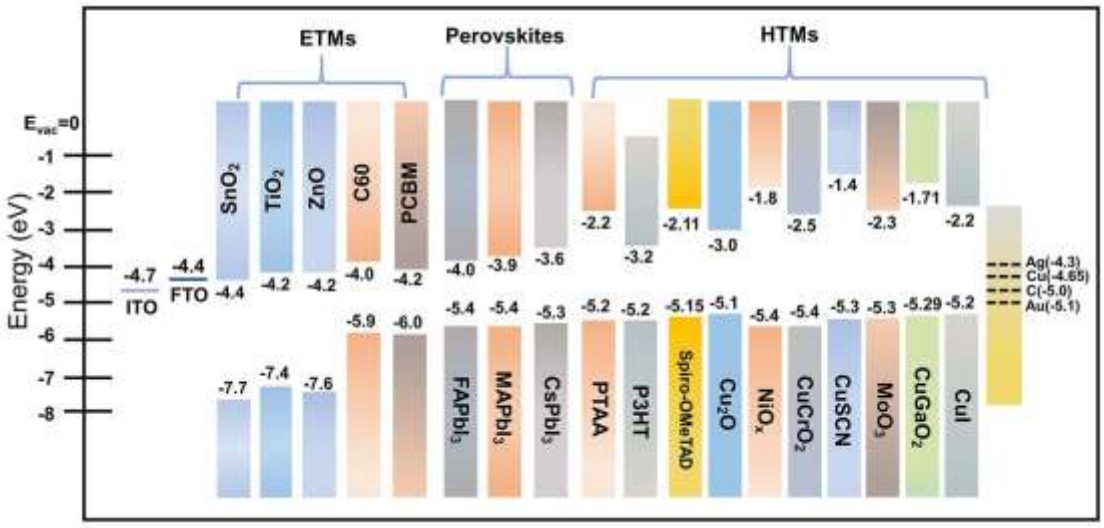

Fig. 12 Energy level diagram of hybrid perovskite with different compositions and different HTMs and CTMs.

passivate the defects, tuning the band energy offsets, block the ion migration, or constructing a barrier to protect the perovskite from ambient environment. Interlayers under perovskite can also serve as templates to modulate the film quality of perovskite. It was reported that 0.2 eV is a proper energy offset to enable efficient charge carrier extraction at the CTL/perovskite interfaces,[157] the modification of the band level of CTLs are important for enhancing device performance.[158] Interfacial materials consist of CTL modifiers and low-dimensional materials will be reviewed in detail in this section.

2.2.2.1 Perovskite/charge-transporting material (CTM) heterojunction. The energy-level alignment between the perovskite and CTM is crucial for device performance. On the one hand, the mismatched energy levels will cause inferior charge extraction efficiency, resulting in charge accumulation and recombination at interfaces. On the other hand, the intrinsic defects of CTMs will also serve as non-radiative recombination centers, leading to serious energy loss. Therefore, interfacial modification of CTMs to enable better energy-level alignment across associated interfaces and to reduce the defect density will contribute to the reduction of recombination loss. The energy levels of commonly used CTMs and perovskites are shown in Fig. 12.

i) Perovskite/electron transporting material (ETM) heterojunction. Defect-free ETM/perovskite interface with a favorable band alignment is crucial to realize high-performance and stable PVSCs. In the normal configuration, TiO_2 is the most used ETM due to its high electron mobility, well-matched energy level, and good contact with perovskite. [159-161] Therefore, electrons can be efficiently extracted in devices with ETM composed of compact TiO_2 layer as blocking layer and mesoporous TiO_2. However, the generation of defects by UV light exposure to TiO_2 causes charge recombination losses.[162] In the defective TiO_2 crystals, the point defects caused by the absence of O atom lead to a defect level below the conduction band, which serves as electron traps.[163, 164] Similar understanding of defects has also been developed for SnO_2.[165] Therefore, relevant interfacial engineering has been studied to address these issues. The reported PVSCs with modified inorganic ETMs are summarized in Table 2.

Recently, You *et al.* have introduced a biopolymer heparin sodium (HS) (Fig. 13a) interlayer onto the surface of TiO_2 to anchor the perovskite and TiO_2 in $MAPbI_3$ solar cells.[166] Interactions between the functional groups ($-COO^-$, $-SO_3^-$, or Na^+) in HS with Pb^{2+} and I^- in $MAPbI_3$ and Ti^{4+} in TiO_2 resulted in the passivated perovskite and TiO_2. The surface wettability of TiO_2 was improved and thus beneficial to form perovskite films with reduced pinholes and roughness. The PCE was enhanced from 17.2% to 20.1% with suppressed hysteresis (Fig. 13b). Liu *et al.* have employed a multifunctional molecule, 5-amino-2,4,6-triiodoisophthalic acid (ATPA), to anchor on TiO_2, which can simultaneously react with dangling -OH on TiO_2 surfaces and passivate the defects of all-inorganic perovskite through its carboxylic acid and amine groups.[167] Cui *et al.* synthesized a variety of gold nanoparticles (Au NPs) with precisely controlled dimensions and structures and inserted them between two layers of TiO_2 ETM. They found that for the Au/SiO_2 core shell NPs, when the thickness of SiO_2 shell is below the critical value, the hot electrons are easily transferred from Au core to TiO_2, resulting in enhanced electron mobility and upshifted Fermi level of TiO_2. As a consequence, devices with sandwich-like

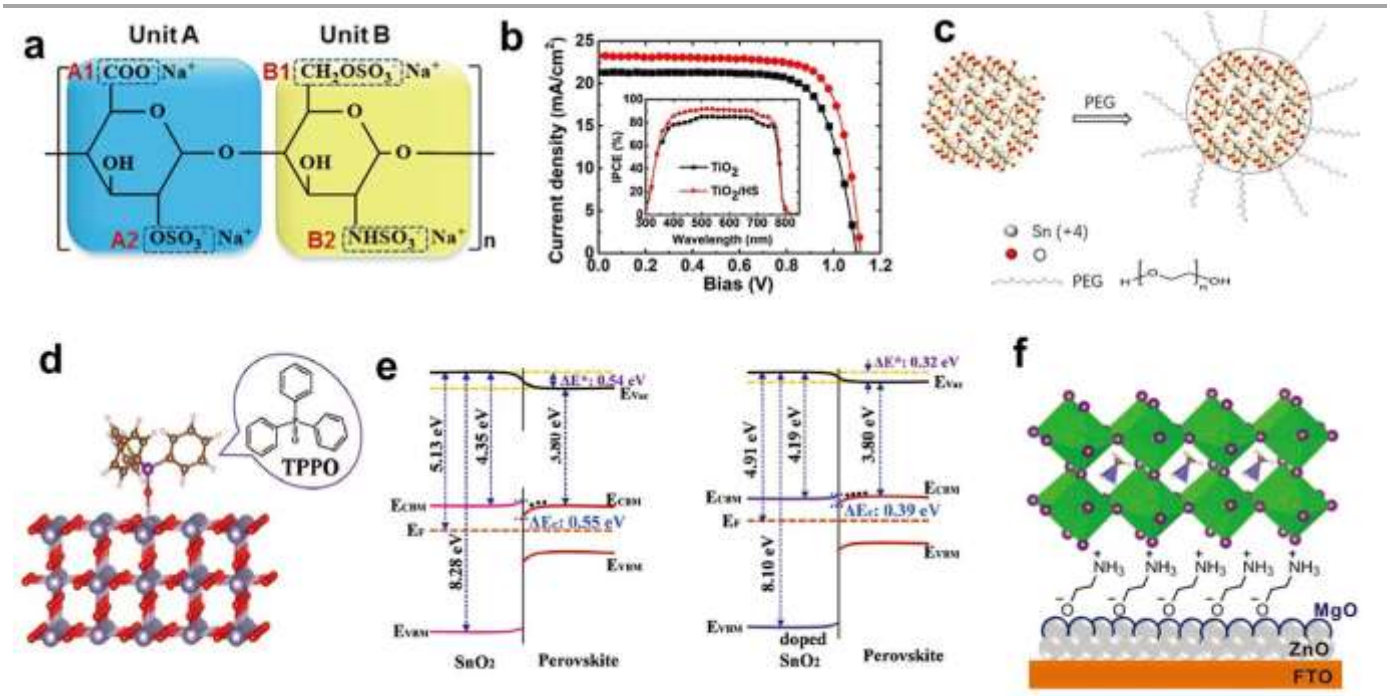

Fig. 13 (a) Chemical structure of heparin sodium salt (HS). (b) *J–V* curves of $MAPbI_3$ devices without and with HS layers. Inset: IPCE spectra of corresponding devices. Reproduced from ref 166 with permission from Wiley-VCH, copyright 2019. (c) Schematic of the interaction between PEG and SnO_2. Reproduced from 170 with permission from Wiley-VCH, Copyright 2018. (d) The model of TPPO molecule absorbed on SnO_2 surface. (e) Energy level diagram of SnO_2/CsFAMA heterojunction before and after doping with TPPO. Reproduced from ref 171 with permission from Wiley-VCH, copyright 2018. (f) Schematic of ZnO–MgO and ZnO–Mg–EA^+. Reproduced from ref 173 with permission from Wiley-VCH, copyright 2018.

TiO_2/Au NPs/TiO_2 ETM exhibited both greatly enhanced J_{SC}, V_{OC}, and PCE.[168] Wang *et al.* developed an acid-treatment method to create an amorphous TiO_2 buffer layer on the anatase TiO_2. As-prepared amorphous TiO_2 layer showed increased electron density due to the presence of oxygen vacancies, resulting in enhanced charge transfer between perovskite and TiO_2. TiO_2 ETL with the amorphous buffer layer realized enhanced J_{SC} and PCE.[169] Wei *et al.* have designed a SnO_2-in-polymer matrix (water soluble polymer PEG) to improve the quality of SnO_2 film and facilitate electron extraction (Fig. 13c).[170] The PEG molecules function as ligands around SnO_2 nanoparticles and hydrogen bonding between PEG and SnO_2 nanoparticles was able to prevent the aggregation of SnO_2 nanoparticles. The alleviated aggregation and enhanced wetting ability contributed to the formation of a compact and pinhole-free SnO_2 layer. The average PCE was improved from 16.2% to 19.5% with enhanced reproducibility. Tu *et al.* have reported the n-doping of SnO_2 with triphenylphosphine oxide (TPPO) molecule (Fig. 13d).[171] The doping led to enhanced conductivity and decreased work function of SnO_2. The energy barrier at SnO_2/perovskite interface was decreased from 0.55 to 0.39 eV (Fig. 13e), facilitating electron transfer at the interface and preventing charge accumulation. As a result, the efficiency was increased from 19.01% to 20.69% with an enhanced V_{OC} from 1.079 V to 1.106 V.

The performance of ZnO-based devices was limited by serious surface recombination, which mainly originates from the intrinsic defects, the surface states of ZnO and the defects formed during the deposition process. Yao *et al.* have developed fullerene-anchored core-shell ZnO as an efficient and stable ETM, in which ZnO was anchored with fullerene nano-shell to suppress trap states and passivate hydroxyl groups on ZnO surface. Devices realized a high efficiency of 21.1%.[172] Cao *et al.* have introduced a thin layer of MgO and protonated ethanolamine (EA) for passivating ZnO (Fig. 13f).[173] The incorporation of MgO-EA^+ resulted in the decreased work function of SnO_2 for better energy alignment with perovskites, and the transmission was also enhanced to improve the light harvest of perovskites. Fabricated devices with graphene encapsulation showed a champion PCE of 21.1% and excellent stability in air for more than 300 h.[173]

In comparison to the more widely used binary metal oxides, ternary metal oxides such as $BaSnO_3$, Zn_2SnO_4 and $SrTiO_3$ offer greater degrees of freedom by simply adjusting their chemical stoichiometry to obtain various properties.[174-176] $BaSnO_3$ is a transparent semiconductor oxide with a wide bandgap of 3.1 eV and high electron mobility. Shin *et al.* have reported a compact La-doped $BaSnO_3$ transport layer via a superoxide colloidal solution method in PVSCs.[174] The La-doped $BaSnO_3$ single crystal and epitaxial thin films represent ultrahigh electron mobility of 320 and 70 $cm^2\ V^{-1}\ s^{-1}$, respectively. The fabricated PVSCs with $BaSO_3$ showed a champion PCE of 21.2% and retained 93% of its initial performance after 1000 h illumination operation. In addition to improving carrier transport, $BaSnO_3$ ETM has been demonstrated as an excellent substitute for TiO_2 owing to its better moisture resistance and light stability.[177] Zhang *et al.* prepared network-like, hierarchical, porous nanospheres Zn_2SnO_4 through a facile and robust polymer-templating method. When applied in PVSCs as ETM, the Zn_2SnO_4 nanospheres can promote the growth of perovskite film, enhance the light absorption and charge extraction, leading to superior device performance in comparison with Zn_2SnO_4 without using the polymer-templating method.[178]

ii) Perovskite/hole-transporting materials (HTMs) heterojunction. Although the perovskite/HTMs interface seems to be less problematic for charge separation, it is still important to perfect this interface to suppress recombination and improve stability. For the p-i-n structured devices, NiO_x, PTAA, and PEDOT:PSS are among the most commonly used HTMs (Table 3). A properly designed functional layer between HTM and perovskite not only can suppress recombination but also can modulate the crystallization of perovskites.

Yao *et al.* have developed a bilayer structure combining p-type Cu:NiO_x nanoparticle-based mesoporous and Cu-doped NiO_x blocking layers to realize efficient hole extraction in inverted PVSCs.[219] The p-doping of NiOx gave rise to the high hole conductivity and the meso-structure with high intensity of pores was beneficial for the deposition of high-quality perovskite. As a result, the series resistance of devices was reduced and the *FFs* were improved to as high as 82%. Large-area devices (1.08 cm^2) exhibited a high efficiency of 18.1%. He *et al*. have designed a 2,2'-(perfluoronaphthalene-2,6-diylidene)dimalononitrile (F6TCNNQ) molecular doped NiO_x HTM to reduce the energy level offset between the VBMs of perovskite and NiO_x from 0.18 to 0.04 eV.[220] The F6TCNNQ molecule can be strongly absorbed by NiO_x ETM and electrons can transfer from NiO_x ETM to F6TCNNQ, realizing the p-type doping of NiO_x. Consequently, the average PCE of mixed cation PVSCs was boosted by 7% and a champion PCE of 20.86% was achieved.

PTAA and PEDOT:PSS are common HTM in p-i-n structured PVSCs due to their suitable HOMO level and high hole mobility. Recently, self-assembled monolayers (SAMs) have become a substitute for traditional HTM in p-i-n PVSCs due to their unique and multifunctional chemical and physical interface properties. Magomedov *et al*. have reported a phosphonic acid-functionalized carbazole derivative SAM to replace the commonly used polymer or inorganic HTM in p-i-n PVSCs.[221] The SAM can function as an undoped hole selective contact, boosting its J_{SC} by 0.3 mA cm^{-2} compared to that of PTAA based devices, and the average FF was close to 80%. Yalcin *et al*. have successfully designed two SAM organic molecules, TPA and MC-43, as WF modifiers and efficient substitutes of PEDOT:PSS on ITO electrodes.[222] The replacement ensured the uniform formation of perovskite layer, reduced charge loss and improved contact selectivity, which resulted in a significant increase in PCE from 9.59% to 17.3%. Recently, Al-Ashouri *et al*. have reported a self-assembled, methyl-substituted carbazole monolayer Me-4PACz as the hole-selective layer in the PVSCs, which obtained 84% FF in single junction PVSCs and a tandem open-circuit voltage of 1.92 V.[29] The Me-4PACz SAM provided fast carrier extraction and effective passivation at the hole

selection interface, allowing lower transmission loss due to its ultra-thin thickness and more suitable energy level alignment.

Table 2 Representatives of perovskite/functional ETMs through modification

ETM	Modification	structure	PCE (%)	Ref
TiO_2	Biopolymer heparin sodium (HS) interfacial Layer	n-i-p	20.1%	179
	K-TFSI treated TiO_2	n-i-p	21.1%	180
	chlorine-capped TiO_2 colloidal nanocrystal film	n-i-p	20.1%	181
	dopamine-capped TiO_2 nanoparticles	n-i-p	21%	182
	Lanthanides doped TiO_2	n-i-p	20.57%	183
	CsBr-Modified Mesoporous TiO_2	n-i-p	21%	184
	C-TiO_2/a-SnO_2	n-i-p	21.4%	185
SnO_2	SnO_2-in polymer (PEG) matrix	n-i-p	20.8%	186
	triphenylphosphine oxide doping SnO_2	n-i-p	20.69%	187
	atomic layer deposition (ALD) of the SnO_2	n-i-p	20%	188
	C9 anchored SnO_2	n-i-p	21.3%	189
	ammonium chloride induced coagulated SnO_2 colloids	n-i-p	21.38%	190
	SnO_2/TiO_2	n-i-p	21.65%	191
ZnO	MgO and EA^+ passivated ZnO	n-i-p	21.1%	173
	sulfur passivation of solution-processed ZnO	n-i-p	19.65%	192
	fullerene-anchored core-shell ZnO nanoparticles	p-i-n	21.1%	193
	ZnO–ZnS interface	n-i-p	20.7%	194

Table 3. Representatives of high-performance PVSCs with different HTMs.

category	HTM	HOMO (eV)	Device structure	PCE (%)	Ref
Small molecule	FDT	-5.16	FTO/TiO_2/Perovskite/FDT/Au	20.2%	195
	DM	-5.27	FTO/TiO_2/Perovskite/DM/Au	23.2%	196
	Z26	-5.16	FTO/TiO_2/Perovskite/Z26/Au	20.1%	197
	X55	-5.23	FTO/TiO_2/Perovskite/X55/Au	20.8%	198
	OMe-TATPyr	-5.4	ITO/SnO_2/Perovskite/OMe-TATPyr/Au	20.6%	199
	G2	-5.22	FTO/TiO_2/Perovskite/G2/Au	20.2%	200
	XPP	-5.15	ITO/SnO_2/C60/Perovskite/XPP/Ag	19.5%	201
	MPA-BTTI	-5.24	ITO/MPA-BTTI/Perovskite/C60/BCP/Ag	21.17%	202
	Spiro-mF	-5.19	FTO/TiO_2/Perovskite/Spiro-mF/Au	24.82%	203
Polymer	P3HT	-5.2	FTO/TiO_2/perovskite(NBH&WBH)/P3HT/Au	22.7%	204
	PTAA	-5.2	FTO/TiO_2/Perovskite/PTAA/Au	22.1%	205
	PEDOT:PSS	-5.2	ITO/PEDOT:PSS/Perovskite/PCBM/Au	18.1%	206
	PCDTBT1	-5.38	ITO/TiO_2/Perovskite/PCDTBT1/MoO_3/Au	19.1%	207
	DTB	-4.96	FTO/TiO_2/Perovskite/DTB/Au	19.68%	208
	PTEG	-5.40	FTO/TiO_2/Perovskite/PTEG/Au	19.8%	209
Inorganic HTM	CuSCN	-5.3	FTO/TiO_2/Perovskite/CuSCN/rGO/Au	20.4%	210
	$CuGaO_2$	-5.29	FTO/TiO_2/Perovskite/$CuGaO_2$/Au	18.51%	211
	$CuCrO_2$	-5.4	ITO/$CuCrO_2$/Perovskite/PCBM/BCP/Ag	19.0%	212
	Cu_2O	-5.28	FTO/TiO_2/Perovskite/Cu_2O/Au	18.9%	213
	CuO_x	-5.4	ITO/CuO_x/$MAPbI_3$/$PC_{61}BM$/ZnO/Al	17.43%	214
	NiO_x	-5.4	FTO/NiO_x/$FAPbI_3$/PCBM/TiO_x/Ag	20.65%	215
complex	CuPc	-5.2	FTO/TiO_2/Perovskite/CuPc/Au	18.8%	216
	CuPc-OBu	-5.11	FTO/TiO_2/Perovskite/CuPc-OBu/Au	17.6%	217
	NiPc-$(OBu)_8$	-5.06	FTO/TiO_2/perovskite/NiPc-$(OBu)_8$/V_2O_5/Au	19.4%	218

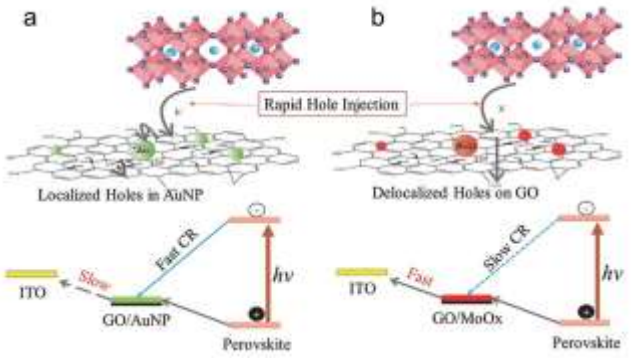

Fig. 14 Schematic illustration of the hole transport mechanism in a) GO-AuNP and b) GO-MoO_x devices. Reproduced from ref 227 with permission from Wiley-VCH, copyright 2018.

In the n-i-p structured devices, Spiro-OMeTAD is the most common HTM used for high-performance PVSCs. However, the low intrinsic mobility of Spiro-OMeTAD requires doping, which causes instability. The modification of perovskite/HTM plays a critical role for realizing stable and efficient PVSCs. Abdi-Jalebi *et al.* have adopted a thermally evaporated dopant-free tetracene at the interface between perovskite and Spiro-OMeTAD to form graded HTMs, which offers a superior hole extraction capability with reduced interfacial defects. Devices exhibited an enhanced V_{OC} of 1.18 V than those with neat Spiro-OMeTAD as HTM (1.13V).[223] Habisreutinger *et al.* have adopted the P3HT-wrapped single-walled carbon nanotubes (SWNTs) as interlayer between perovskite and undoped Spiro-OMeTAD. The reduced series resistance and enhanced hole mobility of undoped Spiro-OMeTAD led to a PCE of 18.8% without any dopants.[224] They also substituted Spiro-OMeTAD with P3HT/SWNTs and PMMA bilayer to improve the thermal stability of devices. PMMA functioned as an effective perovskite protective layer due to its hydrophobicity and thermal stability.[225]

2.2.2.2 Perovskite/2D interfacial materials heterojunction. As mentioned above, the energy level alignment and charge carrier mobility of interfacial materials are crucial properties that influence device performance. 2D materials, including graphene and its derivatives, transition metal dichalcogenides (TMDs), black phosphorus (BP) and Mxenes, have been increasingly developed to modify the CTMs or directly serve as CTMs due to their high conductivity, tunable energy level, excellent chemical, defect-free nature and mechanical properties in recent years.[226]

i) Graphene and its derivatives. Graphene and its derivatives are employed as interfacial materials in PVSCs due to their excellent electrical properties and optical properties in addition to mechanical toughness. They are ambipolar so they can efficiently transport both holes and electrons. Their energy levels and charge carrier mobility can be easily tuned. Besides, the high optical transparency in the wide range of spectrum can help avoid potential parasitic absorption in solar cells.

Reduced graphene oxide (rGO) has been used in PVSCs. Jokar *et al.* have thoroughly investigated the carrier dynamics using GO and rGO as HTM in inverted PVSCs. They found that

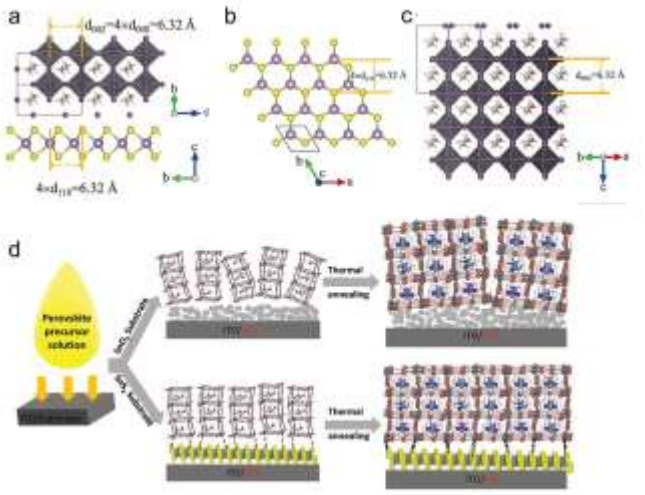

Fig. 15 (a) The side view of atomic crystal heterojunction of $MAPbI_3$ and MoS_2. Atomic crystal structure of the (001) plane of MoS_2 (b) and the (110) plane of perovskite (c). Reproduced from ref 232 with permission from Wiley-VCH, copyright 2019. (d) The crystallization process of perovskite on SnO_2 and SnS_2 substrates. Reproduced from ref 233 with permission from Wiley-VCH, copyright 2018.

although GO can extract holes from perovskite more efficiently, the holes were trapped on the localized oxygen atoms to cause severe non-radiative recombination. The reduction of GO reduced the charge extraction efficiency but suppressed the recombination at the interface. Controlling the degree of reduction to balance the charge extraction efficiency and recombination is crucial for the device performance.[228] Yang *et al.* employed rGO to replace PEDOT:PSS as HTM in inverted PVSCs as its high work function is beneficial for the enhancement of built-in electric field at the perovskite/HTM interface.[229]

Decorated GO have been used as CTMs in PVSCs. Bhosale *et al.* successfully employed MoO_x nanoparticles to functionalize GO, which not only down shifted the work functions of GO, but also suppressed the hole trapping in the GO film. (Fig 14a, b). As a result, the built-in electric field and charge transfer efficiency were simultaneously enhanced, leading to improved $V_{OC,}$ J_{SC} and PCE.[227] Du *et al.* reported $(NiCo)_{1-y}Fe_yO_x$ decorated GO as an effective hole-transporting layers in carbon-based PVSCs. The charge localization on GO surface was suppressed as partial electrons on GO surface would spontaneously transfer to the inorganic nanoparticles due to the variation of electron confinement and the dipole formed from GO to $(NiCo)_{1-y}Fe_yO_x$.[230]

In addition to the employment of graphene and its derivatives as CTMs, these materials are also inserted into the perovskite/CTMs interface to modify the heterojunction. For instance, Han group constructed a Pb-rich perovskite/chlorinated graphene oxide (Cl-GO) heterostructure to enhance the device performance and stability. The proper HOMO level of Cl-GO between VBM of perovskite and HOMO of Spiro-OMeTAD provides an efficient charge extraction pathway for holes from perovskite. The strong bond of Pb-Cl and Pb-O

between perovskite and Cl-GO resulted in the enhancement of device stability.[231]

ii) Transition metal dichalcogenides (TMDs). TMDs are a kind of 2D materials with the formula MX_2, where M represents transition metal such as Mo and W, and X is chalcogen (e.g., S, Se, or Te)). TMDs have tunable electronic and optical properties to show either semiconducting or metallic properties by altering the metal and chalcogen compounds or varying the number layers, which have drawn great attention to form perovskite/TMDs heterojunction in PSVCs recently.

MoS_2 has high carrier mobility and suitable energy level as an effective interfacial material for perovskite/HTM interface. *Tang et al.* firstly reported the vdW epitaxial growth of $MAPbI_3$ perovskite on MoS_2 flakes/PTAA substrate, which results in highly oriented perovskite films with large grain sizes and low defect densities. The enhanced crystallinity of perovskite results from the perfect match between (008) plane of perovskite and the (110) plane of MoS_2 (Fig. 15a, b, c), which promoted the out-of-plane growth of perovskite films with preferential orientation along (110). The HOMO level of MoS_2 lies between the VBM of perovskite and HOMO of PTAA, which facilitates the hole extraction at the interface. The employment of MoS_2 leads to an enhanced PCE from 18.12% to 20.55%.[232] Agresti *et al.* employed a thermal-assisted spray coating method to insert chemically functionalized MoS_2 at the interface of perovskite/Spiro-OMeTAD to fabricate high-performance perovskite solar modules (PVSMs). The functionalization of MoS_2 by connecting thiol group of 3-mercaptopropionic acid (MPA) moieties to the MoS_2 surface via S−S van der Waals physisorption effectively tuned the energy level to match well with perovskite and HTM, enhancing the hole extraction efficiency and resulting in high efficiencies of PVSM of 13.4% and 15.3% at active areas of 108 cm^2 and 82 cm^2.[234]

SnS_2, with layered structure that tin atoms are sandwiched between two layers of hexagonal sulfur atoms through van der Waals interaction, has been introduced as CTMs in PVSCs. Zhao *et al.* employed a Langmuir–Blodgett (LB) self-assembly stacking deposition strategy to form few-layer SnS_2 with flat surface. The dense and smooth SnS_2 film promotes the heterogeneous nucleation upper layer perovskite film and enables uniform deposition of large grains (Fig 15d). Meanwhile, the high transparency (~90% over the visible light range), superior conductivity relative to SnO_2, and suitable level of conduction band minimum ensure efficient charge extraction and transport at perovskite/SnS_2 interface, contributing to a remarkable efficiency of over 20% for n-i-p PVSCs.[233]

TiS_2 is another TMDs employed to construct perovskite/2D materials heterojunction in PVSCs. Yin *et al.* reported a low-temperature solution-processed TiS_2 as ETM in conventional structure PVSCs and realized a decent efficiency of 17.37%.[235] Later, Huang *et al.* incorporated TiS_2 as an interlayer between perovskite/SnO_2 interface to passivate the surface defects of SnO_2 and with better energy matching with perovskite to realize an efficiency of 21.7%.[236]

WS_2 was used as p-type interfacial material in PVSCs due to its high carrier mobility and well-matched energy level with perovskites. Cao *et al.* and Liu *et al.* have separately employed 2D WS_2 flakes to alter the energy level diagram of PTAA/perovskite interface, modify the crystallization of perovskite and passivate defects of perovskite. The defect-free WS_2 surface served as a template for van der Waals epitaxial growth of perovskite films, contributing to highly oriented perovskite grains. The facilitated hole extraction at interface and reduced defects density enables an remarkable PCE of 21.1%.[237] Zhou *et al.* incorporated 2D WS_2 nanoflake into the ETM/$CsPbBr_3$ interface to trigger the vander Waals epitaxy of $CsPbBr_3$ perovskite, which dramatically reduced the interfacial tensile strain due to the interfacial lattice movement via the weak interaction between WS_2 and perovskite, resulting in an ultrahigh V_{OC} of 1.70 V.[238]

iii) Black phosphorus (BP). BP has great potential to be used as interfacial material in PVSCs due to its adjustable bandgap from 0.33 eV (for bulk BP) to 2.0 eV (for single-layer phosphorene) and high carrier mobility (up to 1000 $cm^2 V^{-1} S^{-1}$).[239] Zhang *et al.* introduced 3- to 4-layer-thick BP at ETM/perovskite interface and 1-layer-thick BP at perovskite/HTM respectively. The tunable bandgap of BP through the precise control of its thickness and ambipolar property enables the simultaneously promoted carrier extraction at both interfaces, leading to an enhanced PCE of 19.83% from 16.95%.[240]

iv) MXenes. MXenes are 2D inorganic compounds with a formula of $M_{n+1}X_nT_x$, in which the M represents early transition metal, X is nitrogen or carbon, a, and T stands for a functional group (e.g. O, F, OH, Cl). MXenes combine metallic conductivity of transition metal carbides and hydrophilic nature because of their hydroxyl or oxygen terminated surfaces, making them promising interfacial materials in PVSCs. Several groups have mixed MXenes with traditional ETMs to enhance their conductivity and enhance device performance.[241, 242] Carlo group has employed MXenes with different functional groups to simultaneously tune the work function of perovskite and CTMs, which resulted in more favorable energy level alignment and enhanced device performance.[243-245]

2.2.3 Perovskite/organic bulk heterojunction (BHJ) heterojunction.

In above sections, the modifications of device structures to reduce the electrical losses are introduced. However, these structures are still limited by the thermodynamic principle. The Shockley-Queisser (S-Q) limit indicates that the maximum efficiency for a single-junction solar cell is 33.7%. To break the S-Q limit, multiple photo-responsive materials have to be stacked to reduce thermalization. One simple structure is to directly deposit one absorber on top of the other absorber to form heterojunction. However, such a structure requires compatible deposition methods to avoid damages to the underlying absorber. Besides, the E_g of two absorbers should be complementary to absorb different ranges of light. Recently, bulk heterojunction (BHJ) organic solar cells (OSCs) have been integrated with PVSCs to fabricate devices with such a stacking structure (Fig. 16a). In such a device, two photoactive layers (perovskite as the bottom layer and bulk-heterojunction (BHJ) organic as the top layer) are directly fabricated by sequential

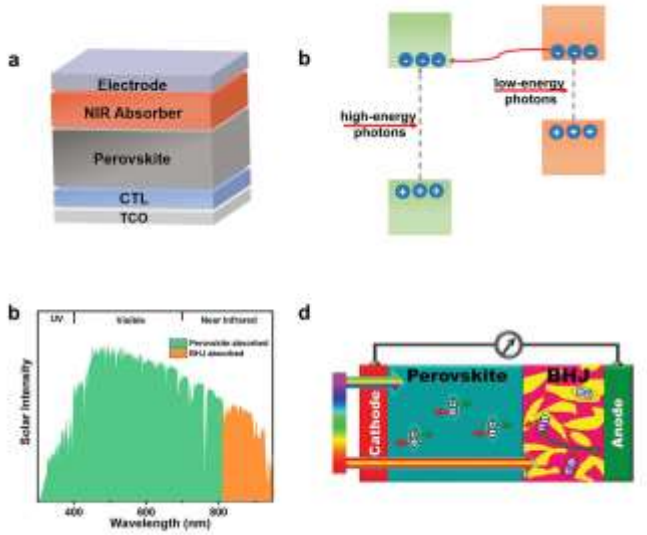

Fig. 16 (a) Schematic of device structure of perovskite/BHJ hybrid solar cells. Schematic of (b) charge transfer and (c) light absorption of perovskite/BHJ hybrid solar cells. (d) Carrier dynamics of perovskite/BHJ hybrid solar cells. Reproduced from ref 246 with permission from WILEY-VCH, copyright 2019.

solution deposition of the two light absorbing layers. Because the perovskite layer and the organic BHJ layer have complementary light absorption, this type of hybrid solar cell not only can reduce the spectral losses but also save the fabrication cost compared to the typical tandem cells.

In a perovskite/BHJ hybrid solar cell, the narrow E_g BHJ absorber is deposited on top of perovskite. The incident light first passes through the large E_g perovskite, where the high-energy photons are absorbed, followed by the low-energy photons absorbed by the narrow E_g BHJ film (Fig. 16b, c). The sufficient harness of photons reduces thermalization loss and transmission loss when compared to the single junction PVSC. Yang group has found that the V_{OC} is determined by PVSCs but the J_{SC} is determined by both absorbers, making such structure possible to break the S-Q limit.[247]

The carrier dynamics of the perovskite/BHJ hybrid solar cells are shown in Fig. 16d. [246] When light passes through the system, the perovskite and BHJ film generate excitons, respectively. For the perovskite film, photo-generated excitons can easily dissociate into electrons and holes due to the low binding energy. For the BHJ film, excitons dissociate at the donor-acceptor (D-A) interfaces. Then, the donor in the BHJ film serves as the HTM, whose HOMO level must be higher than the valence band of perovskite. On the same token, the acceptor in the BHJ film acts as the ETM and its LUMO should match with the CBM of perovskite. Meanwhile, the energy level of donor and acceptor should match with each other to ensure efficient charge separation. Finally, carriers transport across the perovskite and BHJ film and be collected by the respective electrodes. As there are two types of perovskite structures, p-i-n and n-i-p, the BHJ can be employed separately in both structures.

To achieve high performance, several key points should be noted. First, the PVSC should have a high V_{OC} as they determine the V_{OC} of whole device; therefore, strategies introduced in previous sections are also applicable here. Second, the BHJ film should have a narrow E_g and high EQE at the NIR region because it directly affects the J_{SC} of the device; therefore, it is critical to exploit high-performance narrow E_g organic solar cells (OSCs) in this hybrid structure. Third, the energy levels between perovskite and BHJ film should be matched to ensure proper charge carrier dynamics. Finally, the BHJ film should have high charge carrier mobilities closed to those of perovskite. With the rapid development of narrow E_g acceptors, Y6 and its derivatives have achieved both NIR absorption and high EQE compared to previously reported systems (such as IEICO-4F, 6TIC-4F).[248-250] Jen group has recently reported a non-fullerene acceptor, CH1007, with enhanced intermolecular π-core interaction and an absorption edge of 950 nm. The BHJ device based on CH1007 can reach efficiency as high as 17.2%.[251] All these will facilitate the development of perovskite/BHJ hybrid solar cells. In the following part, we will systematically introduce the reports on perovskite/BHJ hybrid solar cells to provide some specific examples.

2.2.3.1 In n-i-p device structure. The early reports mainly employed fullerene acceptor-based BHJ film. In 2014, Yang *et al.* have incorporated a PBDTT-SeDPP/$PC_{71}BM$ BHJ film onto PVSCs to replace the traditional HTM. The BHJ film not only transports charges but also functions as a light absorber to complement the absorption loss of PVSCs in the near-infrared (NIR) region.

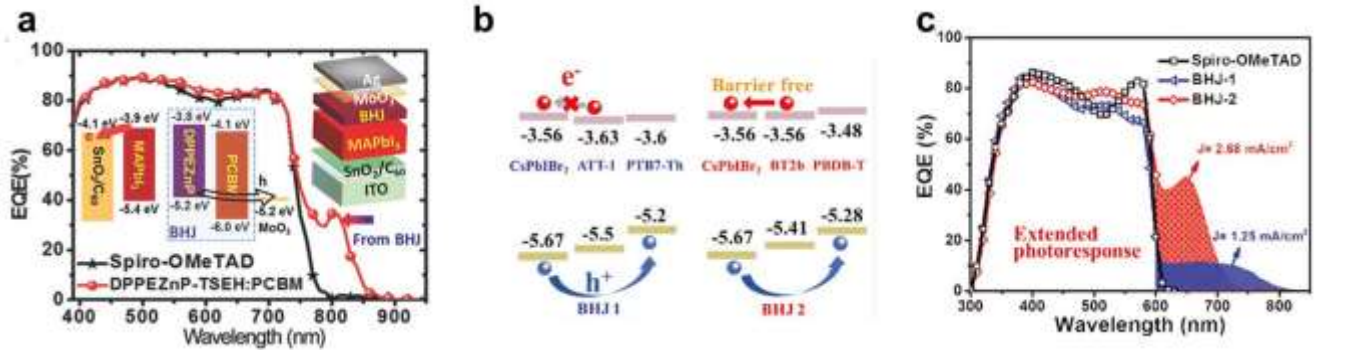

Fig. 17 (a). EQE spectra of perovskite/BHJ hybrid solar cells in comparison to PVSCs with spiro-OMeTAD as HTM; the inset exhibits device structure and energy level diagram. Reproduced from ref 4 with permission from Willey-VCH, copyright 2017. (b) Energy level alignment and EQE spectra (c) of $CsPbIBr_2$-based hybrid solar cells with different BHJ films. Reproduced from ref 256 with permission from Willey-VCH, copyright 2020.

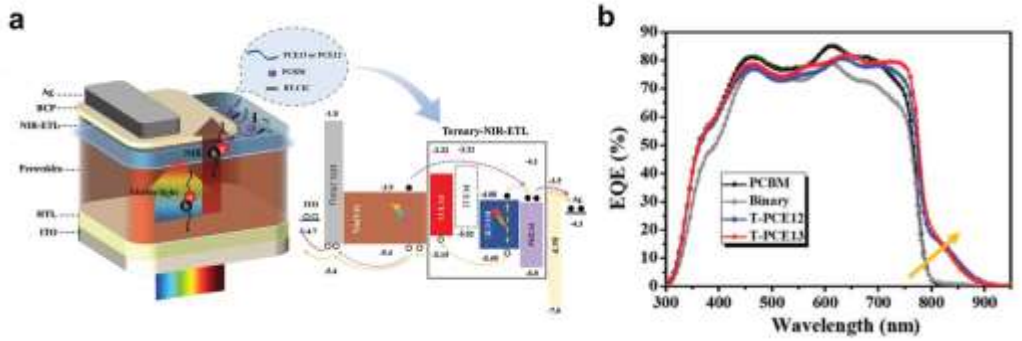

Fig. 18 (a) Device configuration and energy-level alignment of inverted PVSCs with BHJ as ETM and the proposed mechanism of exciton formation and carrier dynamics. (b) EQE spectra of devices using different BHJ films. Reproduced from ref .260 with permission from WILEY-VCH, Copyright 2019.

The absorption edge was extended to over 900 nm, resulting in an enhanced J_{SC} from 19.3 mA/cm^2 to 21.2 mA/cm^2.[252] In 2016, Sun *et al.* have introduced an A-D-A small molecule and $PC_{70}BM$-based BHJ on the surface of perovskite and successfully extended the photovoltaic response to 900 nm.[253] Jen group has successfully fabricated a high-performance perovskite/(DPPZnP-TSEH-PCBM) based hybrid solar cell with a PCE of 19.2%, which is among the highest PCEs reported for the perovskite/organic hybrid solar cells (Fig. 17a). The alkyl-sulfide thienyl electron-donating groups in DPPZnP-TSEH help tune the HOMO level to match with that of perovskite; meanwhile, the S atoms on the molecule serve as Lewis base to passivate perovskite. The strong molecular interaction results in high mobility and *FF* of the devices. The EQE was extended to the NIR range, leading to enhanced current density.[254]

Recently, the BHJ films have also been integrated with large E_g all-inorganic perovskites to enhance J_{SC}. Guo *et al.* integrated BHJ film, PBDTTT-E-T:IEICO, with $CsPbI_2Br$ to broaden the light absorption. The photo response was extended to 900 nm, resulting in an enhanced J_{SC} from 14.78 to 15.98 mA/cm^2. The hydrophobic BHJ film also endows the device with better stability in air.[255] Recently, Chen *et al.* have combined different BHJ films with $CsPbIBr_2$ to fabricate integrated devices. They found PTB7-Th:ATT BHJ has energy barrier to suppress the electron transport from BHJ to perovskite. In contrast, PBDB-T:BT2b system showed well-matched energy level alignment (Fig. 17b). As a result, the EQE at the NIR region is much higher for $CsPbIBr_2$/ PBDB-T:BT2b than $CsPbIBr_2$/PTB7-Th:ATT (Fig. 17c). Moreover, a recast method was developed to modify the morphology and the D/A distribution in a BHJ film to facilitate charge extraction. Consequently, an additional J_{SC} of 2.32 mA/cm^2 was achieved with a PCE of 11.08%.[256]

2.2.3.2 In p-i-n device structure. Ye *et al.* have integrated $MAPbI_{3-x}Cl_x$-based PVSCs (ITO/PEDOT:PSS/Perovskite/PCBM) with PDPP3T and PCBM-based BHJ to achieve an EQE up to 46% in the 800-1000 nm region, contributing to an additional J_{SC} of ~5 mA cm^{-2} for the pure PVSC.[257] Zhang *et al.* have integrated a 90-110 nm PDPP3T:PCBM BHJ film with $MAPbI_3$ perovskite to extend the absorption to 950 nm. The favorable energy level alignment between perovskite and BHJ enables efficient charge transport.[258] Kim *et al.* have blended a diketopyrrolopyrrole (DPP)-based low E_g polymer (LBP) DT-PDPP2T-TT (TT) and $PC_{71}BM$ with a novel n-type polymer, N2200, to enhance electron transport, leading to well-distributed bicontinuous networks and high electron mobility. An enhanced J_{SC} of 20.04 mA/cm^2 was achieved due to the extended absorption.[259] Chen *et al.* have employed a ternary BHJ film (PCE13:BTCIC:PCBM) as an ETL in the inverted-structured PVSCs. They found that the energy level-alignment is crucial for the *FF* and V_{OC}. PCE 13 has a lower HOMO level than PCE 12, better facilitating the hole transport from BHJ to perovskite (Fig. 18a, b). By modifying the morphology of BHJ film, the device showed enhanced NIR photo-response and demonstrated a 40% EQE in the range between 800 nm and 950 nm, which accounts for ~9% of the overall photocurrent.[260]

Recently, Zhao *et al.* have found that the incorporation of a narrow E_g molecule (IEICO-4F) into perovskite film can extend the photo-response to the NIR region. IEICO-4F is also a Lewis base which can passivate the defects at grain boundaries to result in a high PCE of 21.6%.[261] Daboczi *et al.* have found that the interfacial energetics play a key role on the performance of hybrid solar cells. When there is an energy barrier, the device shows reduced V_{OC} and *FF*, even though the J_{SC} was enhanced.[262] Recently, Chen *et al.* have reported a record *Jsc* of 28.06 mA/cm^2 by integrating a 1.60 eV perovskite with a ternary BHJ (S1:Y6:PCBM). However, the integrated device showed a low *FF* of 67.3% and a slightly reduced V_{OC} of 1.09 V, which may be due to not well-matched energy level. This work indicates the effectiveness of enhancing photo-response in the NIR region by Y6-based BHJ, but the interfacial energetics should be carefully modified.[263]

2.3 Multijunction Designs for PVSCs.

The efficiency of current PV technologies is approaching the S-Q limit of single junction cells. Up to now, the efficiency of c-Si solar cells has been stagnant at ~26% for quite a long time. Apart from the perovskite/BHJ hybrid solar cells introduced in Section 2.2.3, the performance limitation of a single-junction cell can also be alleviated by using devices with tandem structures, which combines two or more photovoltaics semiconductors with complementary absorption properties. Tandem solar cells can minimize the thermalization losses of

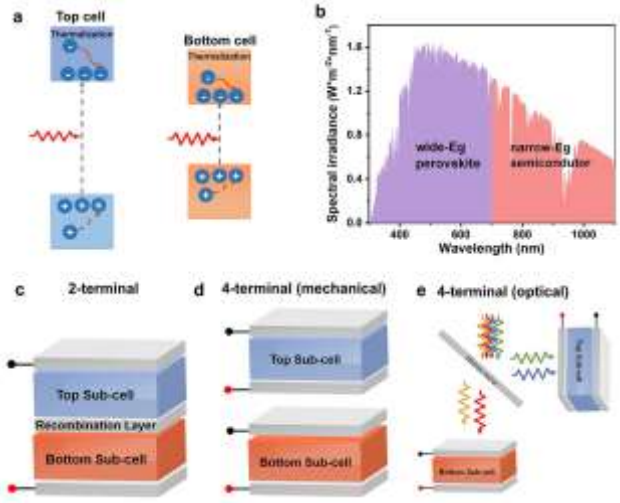

Fig. 19 (a) Tandem solar cells reduce the thermalization loss. (b). The complementary absorption of two sub cells in a tandem cell. Device configuration of (c) two-terminal (2T) and (d) (e) four-terminal (4T) tandem solar cells.

high-energy photons by employing semiconductor layers with matched E_g, providing an up-and-coming approach to realize enhanced performance (Fig. 19a). In a tandem cell, the 'top cell' with a wide E_g semiconductor absorbs high-energy photons but allows the low-energy photons to transmit and be absorbed by the 'bottom cell' with a low E_g semiconductor. The top and bottom cells should be designed based on their spectral efficiency (Fig. 19b).

The monolithic two-terminal (2T) and mechanically stacked four-terminal (4T) configurations are the two main branches of tandem cells (Fig. 19c, d, e). The 2T configuration contains the *in-situ* fabrication of series-connected sub-cells with complementary bandgaps. The sub-cells are often bridged monolithically by an interconnecting layer; therefore, only one of the two external electrical contacts is required to be transparent to ensure the transmission of light into absorber layer. On the contrary, the two sub-cells of 4-T tandem are deposited on respective substrates, and physically connected to each other by four external contacts. Three of them should be semi-transparent to make sure the light passes through both sub-cells. As the parasitic absorption and reflection may occur at the interconnecting layer and interfaces, the more semi-transparent electrical contacts of 4-T tandem are not ideal for practical efficiency. Although 2-T tandem exhibits more potential for high-performance tandem cells, fabricating 2T cells is quite challenging, especially for solution-processed 2T tandem cells, in which the solvents employed for depositing the upper layer may erode the underlying cell.

Fig. 20a, b illustrates the maximum theoretical efficiency according to the E_g of the sub-cells for 2-T and 4-T tandem, respectively. The selection of sub-cells with appropriate bandgaps is vital for the performance of tandem cells. The maximum efficiency for a two-junction tandem device is 47% under one sun illumination when combing the E_g of 1.63 eV for the top cell and 0.96 eV for the bottom cell. Three junctions would result in 52% efficiency and infinite junctions would result in 86% efficiency. In a 2T structure, the series-connected design of the sub-cells enables high voltages as the voltages

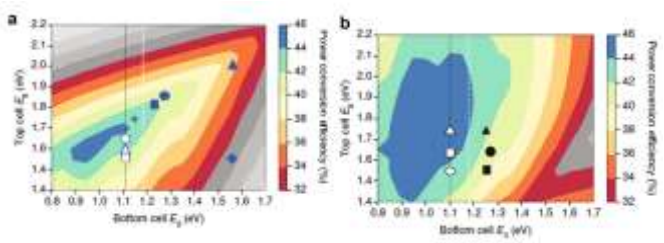

Fig. 20 The maximum theoretical efficiency of (a) 2T tandems and (b) 4-T tandems. Reproduced from ref 27 with permission from Springer Nature, copyright 2018.

produced by each sub-cell are added. Meanwhile, the current through each sub-cell must be identical to meet the 'current matching' requirement. As the sub-cells harvest independent range of the solar spectrum, realizing photocurrent matching at the maximum power point (MPP) condition requires careful bandgap selection and interface engineering. In contrast, the current matching is not required for 4-T tandems, as the sub-cells are fabricated separately and then connected, which is the advantage of 4-T tandem cells.

Previously, tandem solar cells usually consist of III–V compound semiconductors, c-Si, CdTe, and CIGS. Recently, a PCE of 32.8% has been achieved for a multi-junction tandem combining III–V compound and Si.[264] Although the tunable E_g of III–V compound semiconductors make them ideal candidates for high-performance tandem cells, the complex manufacturing processes hinder their development towards market.[265-267] Solution-processed PVSCs with tunable E_g have recently attracted tremendous attention as a promising candidate for fabricating tandem solar cells, due to their unique optoelectronic properties and simple-fabrication process from low-cost precursors. By composition engineering, the tunable E_g of perovskite ranges from 1.17 eV to over 2.3 eV, and almost the full range of available E_g can reach > 50% of its S-Q limit.[26, 27] Therefore, perovskite-based tandem cells have been seriously considered for the fabrication of high-performance devices in both hybrid configuration and all-perovskite structure.

In the 2-T tandem structure, in addition to the two sub-cells, the protective buffer layer and recombination layers are also crucial. Typically, a 5-30 nm transparent buffer layer (MoO_x, NiO_x, VO_x) is deposited through a mild process to prevent the sputter damage of transparent conducting electrode to the underneath soft layers consisting of PVSCs. The recombination layer (such as PEDOT:PSS and SnO_2) was deposited to allow current to pass across the two sub-cells by promoting the opposite carriers from the two sub-cells to recombine in a highly conductive layer. Therefore, the design of a proper 2T configuration is crucial for the device performance. The materials used for recombination layer should have high optical transparency to avoid parasitic absorption, excellent conductivity to facilitate the hole-electron recombination, proper deposition method that does not damage the underlying layers and the barrier effects to stop the solvent penetration.[268-273]

At present, the mostly explored perovskite-based tandem solar cells employed large E_g perovskite (1.6 eV to 1.80 eV) as the top absorbers and silicon, CIGS, narrow E_g perovskite or BHJ as bottom absorbers. In this hybrid structure, the incorporation

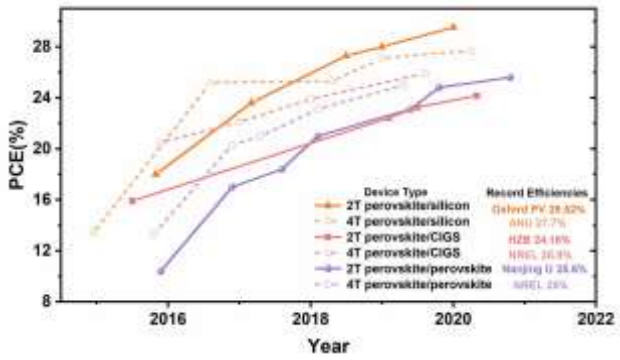

Fig. 21 Efficiency evolution of perovskite-based tandem solar cells. [274-298]

of PVSCs not only contributes to an enhanced efficiency, but also reduces device fabrication cost, providing an effective strategy to prepare high-efficiency panels for Si-based and thin-film based solar cells. The efficiency evolution of different kinds of tandem solar cells is shown in Fig. 21. Perovskite–Si tandem solar cells have recently reached a PCE of ~29.52 % in a 2-T configuration.[29] All-perovskite tandem also presents great opportunities for high-performance panels with low cost, high throughput and potentials of flexible applications. The progress of perovskite-based tandem solar cells will be reviewed in the following sections.

2.3.1 Perovskite/silicon tandem solar cells.

As mentioned earlier, c-Si PV technology accounts for 90% of the PV market share and the certified efficiency has been over 25%, indicating that it has already approached its S-Q limit. To further increase its efficiency, perovskite/Si tandem cells adopting wide E_g PVSCs as the top cell and Si solar cells as the bottom cells to break the S-Q limit. With only a few years, the perovskite/silicon tandem solar cells have already shown a record PCE of 29.52%.[29] To further enhance the efficiency, some challenges should be overcome, including reducing optical losses, electrical losses, and processing damages.

One of the crucial aspects of fabricating high-performance perovskite/silicon tandem solar cells is to reduce optical losses. The optical losses of perovskite/ silicon solar cells mainly originated from several aspects: First, the absorption of two sub cells should be complementary, as the E_g of silicon is ~1.1 eV, the perovskite sub cells should have a E_g of ~1.7 eV. Employing perovskite with other E_g will cause lower J_{SC} and poor performance. For example, some early works used 1.5~1.6 eV perovskite as top absorber, limiting the J_{SC} to only 15~16 mA/cm^2 and PCEs of 20%-22%, which is even lower than the single-junction PVSCs.[299-302] The optimization of wide E_g PVSCs is one of the driving forces that advance the perovskite/silicon tandem cells to the current status.

Second, the large number of interlayers in tandem solar cells causes optical interferences with great differences in refractive indices, resulting in unwanted reflection. The silicon has a refractive index over 3.0, which is much higher than that of perovskite, air, and transparent conductive oxide (TCO), leading to serious reflection when light passes into silicon. To solve this problem, one strategy is to use double-sided textured silicon as the bottom cell, which has been widely used in single-junction silicon solar cells. The challenge of such structure is to deposit conformal perovskite and CTMs on a textured substrate although it is calculated that nanotexture with a depth of ~150 nm is enough to reduce reflection losses in tandem structure. Ballif *et al.* have developed sequential deposition methods to gain conformal perovskite layers on textured silicon heterojunction (SHJ) bottom cells, in which top cells were fabricated on the double-side-textured SHJ bottom cell by thermal evaporation of an HTM and a porous PbI_2 (with CsBr) as template, followed by spin-coating the solution of FAI and FABr to acquire high-quality perovskite (Fig. 22a, b). The double side textured tandem showed a low current loss of 1.64 mA/cm^2 from reflection loss, which is much lower than those with only rear side textured device (3.14 mA/cm^2) (Fig. 22c). The champion tandem device realized a PCE of 25.2 % with an extremely high J_{SC} of 19.5 mA/cm^2.[303] Chen *et al.* have developed a nitrogen-assisted blading method to deposit conformal HTM and perovskite layer that fully covers the textured silicon, achieving an efficiency of 26% with a J_{SC} of 19.2 mA/cm^2.[305] Hou *et al.* have combined the solution-processed 1.1 µm perovskite with fully textured silicon heterojunction bottom cells to realize a certification PCE of 25.7% with a J_{SC} of 19.3 mA/cm^2. The thick perovskite layer enables a full coverage of textured silicon, and passivators guarantee a high carrier diffusion length for the carrier transport in the thick film (Fig. 22d, e).[304] Another strategy is to employ interconnecting layer

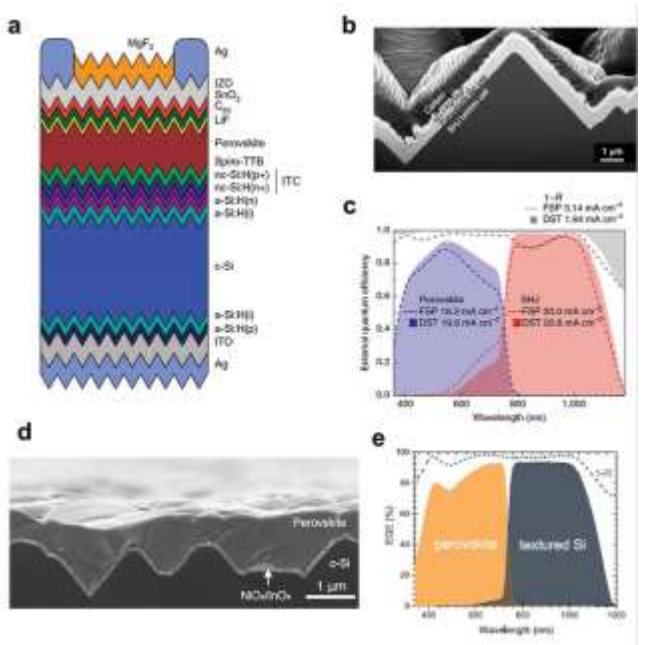

Fig. 22 (a) Device configuration of double-side-textured perovskite/silicon tandem solar cells. (b) Cross-section SEM image of the perovskite top cell deposited on the textured silicon bottom cell. (c) EQE of perovskite/silicon 2T tandem cells with double-side-textured or front-side-polished (FSP) bottom cells. Reproduced from ref 303 with permission from Nature Publishing Group, copyright 2018. (d) Cross-sectional SEM images of a textured c-Si covered with perovskite film. (e) EQE of the textured devices, 19.3 mA/cm^2 for the top cell and 19.2 mA/cm^2 for the bottom cell. Reproduced from ref 304 with permission from the American Association for the Advancement of Science, copyright 2020.

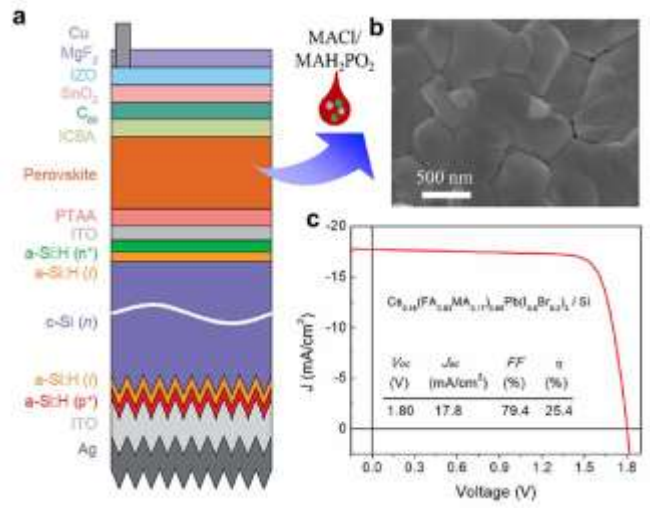

Fig. 23 (a) Device configuration of tandem solar cells with MACl/MAH_2PO_2 modified perovskite; (b) Top view SEM image of MACl/MAH_2PO_2 modified perovskite film. (c) *J-V* curve under forward and reverse scans of the champion $Cs_{0.15}(FA_{0.83}MA_{0.17})_{0.85}Pb(I_{0.8}Br_{0.2})_3$/Si tandem device. Reproduced from ref 313 with permission from Elsevier Inc, copyright 2018.

with similar refractive index to silicon or develop effective anti-reflection layers. Nanocrystalline silicon and nanocrystalline silicon oxide have both been reported as interconnecting layer materials to significantly mitigate reflection losses at perovskite/silicon interface.[306, 307] Additionally, the textured polydimethylsiloxane (PDMS) films have been reported as an efficient antireflection layer to reduce reflection loss at the front side of a tandem cell.[308, 309]

Third, the interconnecting layers and CTLs unavoidably have their own absorption, leading to parasitic absorption and causing optical losses, which is extremely serious in 4T tandem solar cells due to two transparent electrodes are incorporated in the devices. Therefore, choosing materials with low absorption as interlayers or simplifying the device structure can reduce the parasitic loss.[302, 310, 311]

To suppress the electrical losses is another important aspect for fabricating perovskite/silicon tandem solar cells. To achieve high performance, the two sub cells and recombination layers should be carefully designed to suppress electrical losses in the bulk and at the interfaces. The interconnecting layers should have low contact resistance but not too conductive to avoid shunt. The silicon solar cells should be efficient enough, in which heterojunction silicon solar cells have gradually replaced homojunction structure due to their superior performance, especially for their high performance.[312] For the wide-E_g PVSCs, the phase segregation induces rapid efficiency decays under illumination. Besides, their energy loss is serious compared with that of ~1.5 eV perovskite.

Recent reports have proved that both these two drawbacks of wide E_g perovskites originate from high defect densities. Therefore, effective passivation of perovskite is essential for enhancing the device performance and stability. Strategies such as composition engineering, surface passivation, and employing additives have been widely used to solve this problem.[314-317] For example, Huang *et al.* have employed MACl and MAH_2PO_2 as additives in perovskite precursor to improve the film quality of large bandgap perovskites (Fig. 23a) .[313] MACl slowed the perovskite crystallization process and enabled the deposition of smooth perovskite films with larger grains and preferential orientation (Fig. 23b). MAH_2PO_2 decreased the expelled rate of MACl from the film, and thus enhanced the effect of MACl on enlarging the grain sizes. The improved perovskite quality has contributed to a high PCE of 25.4 % for perovskite/Si tandem with improved V_{OC} of 1.80 eV (Fig. 23c).[313]

Recently, Xu *et al.* have incorporated chlorine into wide E_g perovskite to enhance the performance and stability. Instead of MACl, they found that the employment of $MAPbCl_3$ or $PbCl_2$ does not improve the grain size, and they tend to reside in the perovskite lattice after annealing. The incorporation of chlorine induces the enlargement of E_g; therefore, reducing the use of bromide to obtain the large E_g. As a result, the carrier lifetime and phase stability of as-prepared wide E_g PVSCs were dramatically enhanced, resulting in a high PCE of 27% for perovskite/silicon tandem solar cells with an area of 1 cm^2.[318] Kim *et al.* have employed anion engineered phenethylammonium-based 2D additives to passivate perovskite and realized a PCE of 26.7% for 2T-tandems.[285]

Moreover, it is important to overcome the processing challenges. In a tandem cell, the deposition of upper layer should not cause damage to the bottom layer. The silicon solar cell cannot bear temperature > 200°C, so the interconnecting layer and perovskite should be deposited at low temperature. Different from the single-junction PVSCs, the top transparent electrode in many tandem configurations, such as ITO, has to be deposited on top of the perovskite cell to ensure low energy photons cross over the PVSC sub-cell. To prevent sputtering damage to the underlying PVSCs, several research groups have developed 'sputter buffer' protective layers, which are often deposited at low temperature with mild precursors. MoO_x, NiO_x and VO_x are among the most used protective materials for this layer.

2.3.2 Perovskite/CIGS tandem solar cells.

The E_g of the CIGS absorber layer can be tuned between 1.05 and 1.65 eV by changing the ratios of In and Ga in the semiconductor.[319, 320] Currently, these materials are optimized for use in single junction devices with a E_g of 1.17 eV.[321, 322] The current record of highest PCE for perovskite/CIGS tandem cells is 24.16 %. The PVSCs and CIGS solar cells are both thin-film solar cells, which allows the fabrication of flexible devices with a high power-to-weight ratio.[323] In spite of these advantages, there are challenges remaining for the fabrication of high-performance perovskite/CIGS tandem cells.

There are several challenges to fabricate high-performance perovskite/CIGS tandem solar cells: (1) *Processing Challenges*. As the device structure of CIGS solar cells is substrate/Mo/CIGS/CdS/ZnO, only p-i-n structured PVSCs are suitable for fabricating perovskite/CIGS tandem solar cells. Besides, the CIGS can only withstand low temperatures, so the PVSCs and interlayers cannot be deposited with high temperatures. Moreover, the roughness of CIGS surface is 50~200 nm depending on the fabrication process, therefore, the PVSCs should be thick enough to fully cover the CIGS.

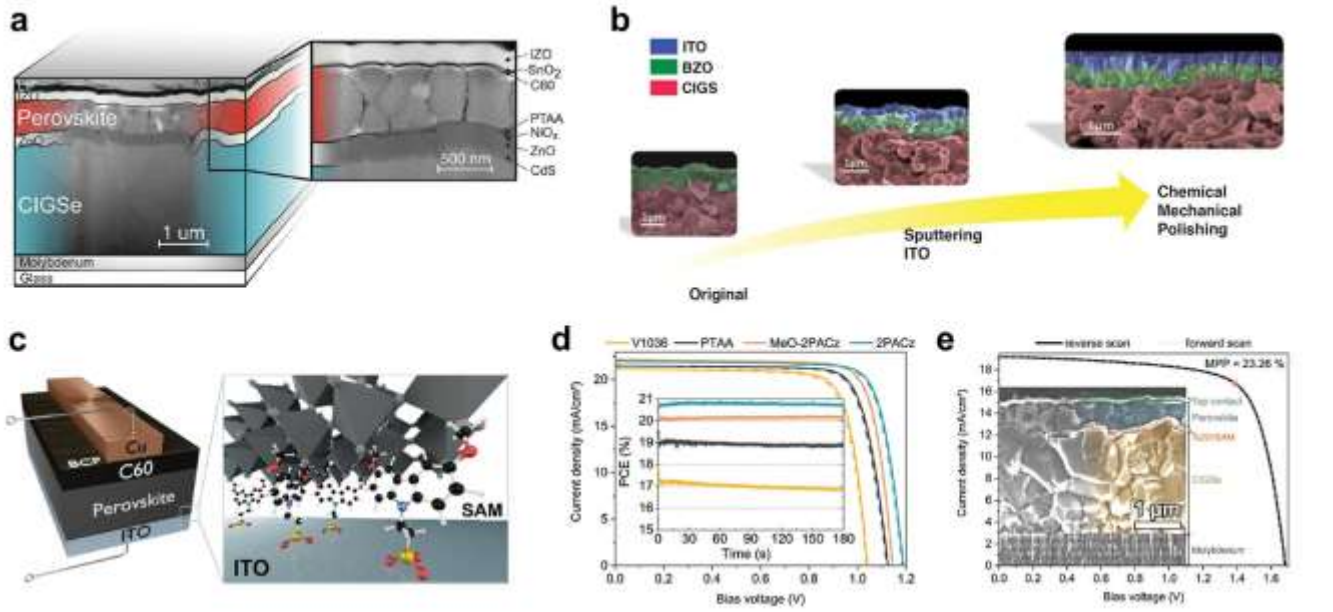

Fig. 24 (a) Device configuration and cross-sectional SEM image of perovskite/CIGS tandem solar cells with atomic layer deposited NiO_x. Reproduced from ref 324 with permission from American Chemical Society, copyright 2019. (b) Schematic illustration of the deposition of ITO via sputtering and post-treatment by chemical mechanical polishing. Reproduced from ref 298 with permission from the American Association for the Advancement of Science, copyright 2018. (c) Schematic illustration of the wide bandgap PVSC with SAM molecules attaching to the ITO surface. (d) *J–V* curves of single-junction wide bandgap PVSCs with different SAMs and PTAA as HTMs under one sun illumination with respective MPP tracks in the inset. (e) *J–V* curve of a monolithic CIGS/perovskite tandem solar cell with MeO-2PACz2PACz SAM as HTM. The inset showed the cross-section SEM image of devices. Reproduced from ref 325 with permission from the Royal Society of Chemistry, copyright 2019.

To conformally deposit perovskite/CIGS tandems, Jang et al. have deposited a layer of ZnO onto PCBM as a buffer layer to prevent damage the under layers when deposit AZO.[326] Albrecht *et al.* have deposited a fully covered thin layer of NiO_x through atomic layer deposition on CIGSe bottom cell to prevent the possible shunting owing to the rough CIGSe surface. It resulted in a high PCE of 21.6% for 2-T tandems **(**Fig. 24a).[324] Yang *et al.* have deposited a smooth ICL by chemical mechanical polishing (CMP) deposited ITO to reduce the surface roughness, which provided a smooth scaffold for fabricating PVSCs and a better ohmic contact for hole transport. The resulting tandem cells showed a high PCE of 22.43 % (Fig. 24b).[298]

(2) *Optical Management*. Similar to perovskite/silicon tandem solar cells, suppressing optical losses in perovskite/CIGS tandem is also crucial, although the reflection losses of perovskite/CIGS tandems are not as severe as perovskite/silicon tandems. However, the current matching for 2T tandems and reduction of parasitic absorption are still quite challenging for device performance. Meanwhile, the interlayers should have high transmittance to realize high J_{SC}. Todorov *et al.* have developed a reactor for precise control of the optical E_g of the perovskite layer via vapor-based halide exchange reactions at 100 °C, achieving an efficiency of 15.9%.[327] Uhl *et al.* have employed perovskite and CIGS with complementary E_g to achieve 2T tandems with a PCE of 18.5%.[328] Catchpole *et al.* have fabricated a semi-transparent PVSC with a champion PCE of 18.1% with the *bandgap* of 1.62 eV and then combined it with a 16.5% CIGS cell to form perovskite/CIGS tandem cells. The fabricated tandem devices exhibited a high PCE of 23.9%.[329]

(3) *Suppressing Electrical Losses*. As wide E_g is used in perovskite/CIGS tandems, the defects should be sufficiently passivated in PVSCs to reduce $V_{OC,loss}$ and alleviate phase segregation. In addition, a well-matched energy level alignment should be ensured throughout the whole device to promote the efficient work of devices. Recently, Albrecht *et al.* have replaced traditionally used HTM, PTAA, with a self-assembled monolayer through facile solution process, which demonstrated stronger hole-selectivity than PTAA (Fig. 24c, d). They realized an efficiency of over 21% for single-junction PVSCs and 23.26% for perovskite/CIGS 2T tandems (Fig. 24e).[325] Recently, Kim *et al.* employed bimolecular additives (PEAI and $Pb(SCN)_2$) to modify the crystallinity of wide-E_g perovskite, achieving a high PCE of 25.9% for 4T perovskite/CIGS tandem solar cells.[67]

2.3.3 All-perovskite tandem solar cells.

The bandgap tunability of perovskites along with their cost-effectiveness and facile production feasibility create a great opportunity for the development and commercialization of perovskite/perovskite tandem cells.[314] Rajagopal *et al.* have shown that the strive for high performance optically stacked and electronically connected 2-terminal devices necessitates the development of two essential requirements that are not adequately explored so far: (1) a high performance and stable narrow bandgap perovskite material; (2) an efficient charge recombination layer (CRL) with low optical and ohmic losses, utilizing a deposition process compatible with the underlying structure; (3) a high-performance and phase stable large bandgap perovskite solar cell.[330]

Thus far, the composition engineering toward smaller E_g has been achieved by incorporating tin-based perovskites but facing significant challenge of dealing with their oxidative sensitivity and processability. It has been shown that the

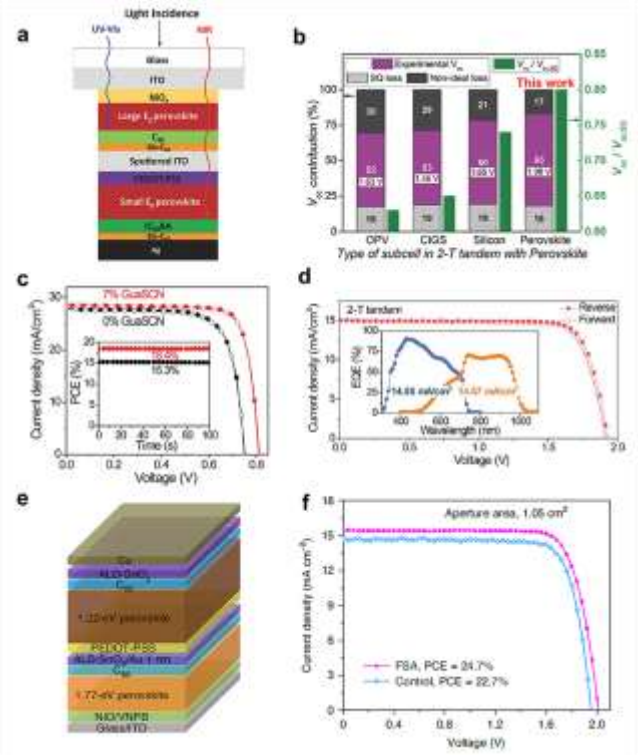

Fig. 25 (a) Device configuration of perovskite/perovskite tandem solar cells with optimized sub cells from the Jen group. (b) Fractional contribution of V_{OC} and associated losses with respect to bandgap for different high-performance perovskite-based tandem solar cells. Reproduced from ref 330 with permission from WILEY-VCH, copyright 2017. (c) *J-V* curves of narrow bandgap PVSCs with and without GuaSCN as additives. (d) *J-V* curves of the perovskite/perovskite tandem solar cells with GuaSCN additive and corresponding EQE spectra of the top and bottom sub-cells. Reproduced from ref 278 with permission from American Association for the Advancement of Science, copyright 2019. (e) Device configuration and (f) *J-V* curves of large-area all-perovskite tandem solar cells with formamidine sulfinic acid (FSA) additives. Reproduced from ref 280 with permission from Nature Publishing Group, copyright 2020.

additives of Cs and FA ions tend to stabilize and enhance the lifetime of the tin-based PVSCs. Pb and Sn binary perovskites showed an anomalous lower E_g than either of the pure phases and more stable than pure tin-based perovskites. All these features are beneficial to the development of all-perovskite tandem cells, which is more cost effective and proper for flexible application. Due to the achievable lowest E_g of perovskite is about 1.25 eV, the bandgap of perovskite in top cells is required to 1.75-1.80 eV, which are more unstable than those used in perovskite/silicon and perovskite/CIGS tandems. Therefore, achieving stable 1.75-1.80 eV perovskites and reducing the energy loss are quite crucial.

Currently, the research is mainly focused on the optimization of the two sub-cells. Snaith *et al.* have optimized the fabrication of small E_g PVSCs and employed a layer of SnO_2 with sputtered ITO as the recombination layer to prevent the underlying sub-cell from being damaged. Combining this small E_g sub-cell with a large E_g sub-cell based on $FA_{0.83}Cs_{0.17}Pb(I_{0.5}Br_{0.5})_3$ perovskite resulted in a 2-T tandem solar cell with a PCE of 17%.[275] Jen *et al*. have performed a dual optimization of the large E_g sub-cell and small E_g sub-cell to improve the performance of tandem solar cell to reach a high PCE of 18.5 % and V_{OC} of 1.98 V (~ 80% of the theoretical limit (Fig. 25a, b).[330] Their work indicates that the optimization of sub-cells is crucial for the enhancement of tandem devices.

Recently, Yan *et al.* have incorporated chloride into perovskite precursor to realize bulk-passivation and enhanced performance of PVSCs. They have successfully fabricated a narrow E_g PVSC with a thick absorber layer (~750 nm) and realized a PCE of 18.4%. By combining the prepared narrow E_g sub-cell with a large E_g (1.75 eV) sub-cell, the resulting 2-T tandem cells showed a high efficiency of ~21%.[331] Zhu *et al.* have further employed guanidinium thiocyanate (GuaSCN) as an additive in 1.25 eV bandgap perovskite to fabricate highly efficient small E_g PVSCs (Fig. 25c).[278] The SCN^- enabled the increase of grain sizes. The Gua^+ led to the formation of 2D structure at grain boundaries, which is beneficial for the defect passivation at grain boundaries and the suppression of Sn vacancies. Such incorporation of GuaSCN reduced defects density and prolonged the carrier lifetime to over 1 microsecond, resulting in a high PCE of 23.1% for 2-T tandem cells and 25% for 4-T tandem cells (Fig. 25d).[278] Lin *et al.* have employed Sn powder to suppress the oxidation Sn^{2+}, realizing a high PCE of 24.8% for 2T all-perovskite tandem solar cells.[332] Huang *et al.* have employed a simplified ICL with unintentionally n-doped $C_{60}/SnO_{1.76}$. The $SnO_{1.76}$ showed ambipolar carrier transport property due to the presence of a large amount of Sn^{2+}. Such ICLs demonstrated ohmic contact with both the top and bottom cells, realizing a high PCE of 24.4%.[271] Xiao *et al.* have used reductive surface-anchoring zwitterionic molecules to simultaneously passivate defects and suppress the oxidation of Sn^{2+} in narrow E_g sub cell, reaching a high PCE of 24.7% for 2T tandem solar cells with an active area of 1.05 cm^2 (Fig. 25e, f).[280]

2.3.4 Other type tandem solar cells.

As mentioned in Section 2.2.3, BHJ organic solar cells have tunable E_g, which can also be incorporated with perovskite to fabricate tandem solar cells. Moreover, organic solar cells are perfect candidates for fabricating flexible devices, which provide perovskite/organic tandem cells with various potential applications. Besides, the orthogonal solvents employed for organic solar cells and PVSCs facilitate the fabrication of tandem devices. There are several groups that have reported the fabrication of perovskite/organic tandem solar cells. In 2016, Liu *et al.* have combined $MAPbI_3$ perovskite with PBDTT-DPP:$PC_{70}BM$ to fabricate tandem solar cells and achieved an efficiency of 8.62%.[334] The unmatched E_g limits the J_{SC}. In 2018, Chen *et al.* have employed all-inorganic perovskite, $CsPbBr_3$, to fabricated tandem solar cells with an organic photoactive layer. The excellent stability of $CsPbBr_3$ perovskite enables it as an UV-filter to protect the BHJ film from UV light. As a result, the tandem devices showed superior stability.[335] Recently, Li *et al.* have fabricated flexible perovskite/organic tandem solar cells with a PCE of 13.61% and applied it to water splitting electrocatalysis, achieving a solar-to-hydrogen efficiency of 11.21%.[336] Xie *et al.* have fabricated $CsPbI_2Br$/PM6:Y6 based tandem solar cells with an efficiency of 18.38%.[337] Aqoma *et al.* have combined $CsPbI_2Br$ with PTB7-Th:IEICO-4F BHJ to realize

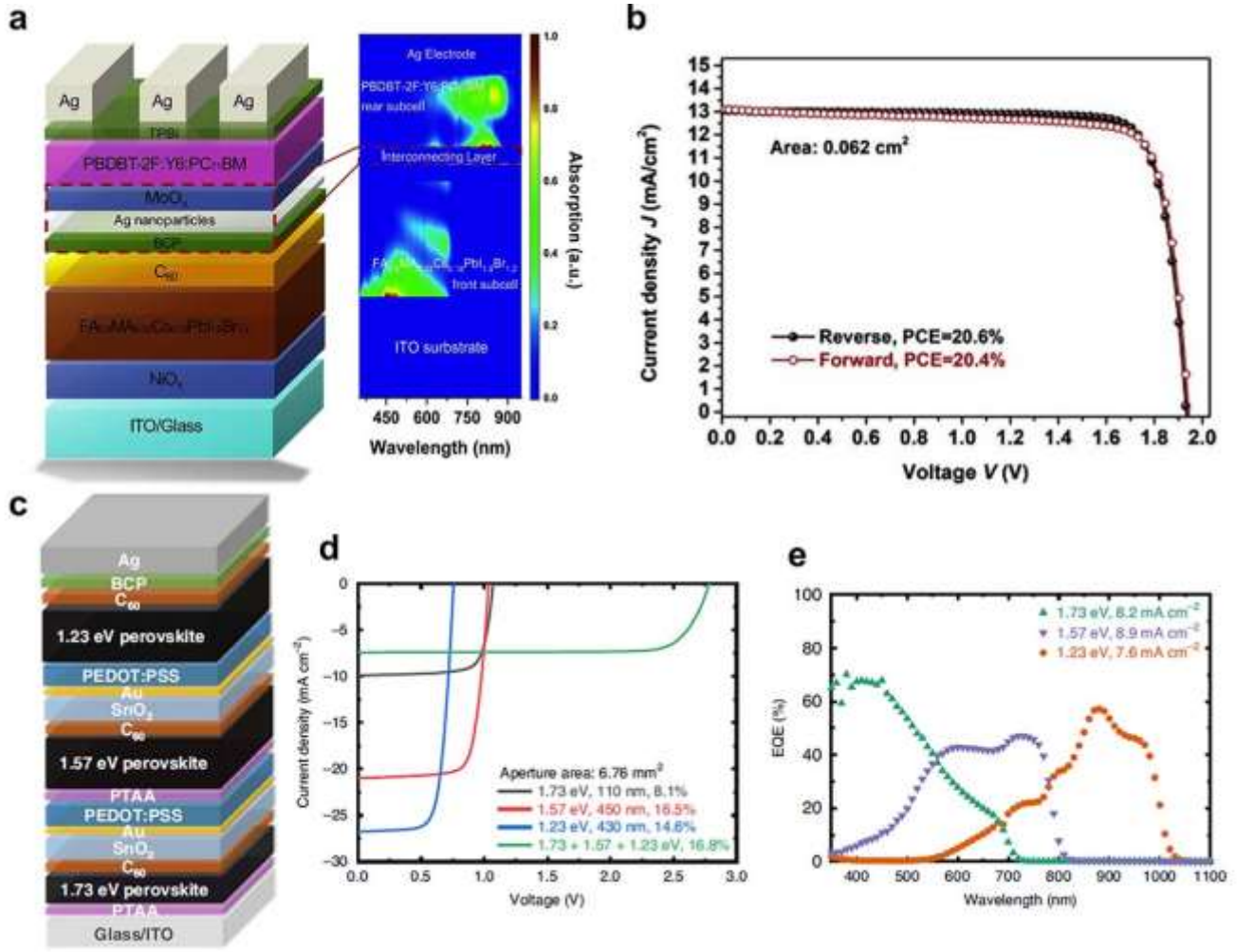

Fig. 26 (a) Device configuration of high-performance perovskite/organic tandem solar cells and simulated distributions of photon absorptions. (b) *J-V* curves of champion perovskite/organic tandem solar cells with forward and reverse scan. Reproduced from ref 339 with permission from Elsevier Inc, copyright 2020. (c) Device configuration of triple-junction all-perovskite tandem solar cells. (d) *J-V* curves of single-junction sub cells and tandem solar cells. (e) EQE of spectra of triple junction tandem solar cells. Reproduced from ref 340 with permission from Nature Publishing Group, copyright 2020.

an efficiency of 18.04%.[338] The highest efficiency of perovskite/organic tandem cells are obtained by Yang *et al.*, as they employed all-thermally evaporated ICLs, $FA_{0.8}MA_{0.2}Cs_{0.18}Pb_{2.8}Br_{1.2}$ perovskite and Y6-based ternary BHJ to reach a high PCE over 20%, proving the potential of fabricating high-performance tandem solar cells (Fig. 26a, b).[339]

There are also reports on triple-junction perovskite-based tandem solar cells. Although three junction perovskite tandem solar cells showed higher theoretical efficiency, there are very limited reports due to the difficulty involved in fabrication. Werner *et al.* have fabricated perovskite/perovskite/silicon tandem solar cells with a V_{OC} of 2.69 V by tuning the perovskite composition and modifying the recombination layers.[341] McMeekin *et al.* have fabricated the first triple-junction all-perovskite tandem solar cells through all-solution process, achieving a high V_{OC} of 2.83 V and a PCE of 6.7%.[342] Wang *et al.* have combined 1.73 eV/1.57 eV/1.23 eV perovskites to achieve a 16.8% efficiency for triple junction all-perovskite tandem solar cells (Fig. 26c-e).[340]

3. Conclusions and Outlook

In this review, we have systematically reviewed the evolution of PVSCs from single junction, heterojunction to multijunction. The passivation of defects and optimization of crystallization in single junction solar cells contributes to improved device performance. The modified heterojunction designs through perovskite/perovskite heterojunction, perovskite/functional layer heterojunction and perovskite/organic BHJ heterojunction enables the PCE to reach beyond 25%. The rising of perovskite-based multijunction solar cells makes it possible to achieve efficiency of > 30% *via* reducing thermalization loss. However, there are still several issues listed below that need to be resolved before PVSCs can be considered for commercialization.

Performance. To achieve a deeper understanding of carrier dynamics, defects nature, and how they influence the device performance are essential to continue enhancing the performance of PVSCs. To reduce the potential losses, further modifications of perovskite deposition, development of proper materials for defect passivation, exploration of optimal perovskite compositions, and development of CTMs will alleviate non-radiative recombination and prolong the carrier

lifetime in perovskites. To reduce optical losses, the parasitic absorption of CTMs at the front contact needs to be alleviated *via* more transparent materials. Light absorption enhancing materials (such as light conversion NPs, plasmonic NPs) can be incorporated into the perovskite films. The employment of textured perovskite films and the popularization of anti-reflection (AR) coating will also afford higher J_{SC}.

More attention should be paid on PVSCs-based multijunction solar cells, which possess the promising potential to achieve PCE > 30%. The relationship between defects, energy loss, and photo-induced phase segregation in wide E_g perovskites requires a deeper understanding and novel solutions. Strategies should be employed to optimize and stabilize wide E_g perovskite top cells, including composition engineering, defect passivation, and interface modifications. ICL materials with high transparency, suitable energy levels, conductivity, moderate deposition methods that don't damage the underlayer materials, and proper barriers to prevent the solvent penetration should be developed. Optimizing methods to deposit thick and compact perovskite layer on rough surface is beneficial for fabricating perovskite/textured silicon and perovskite/CIGS tandem solar cells. Exploring strategies to suppress the oxidation of Sn^{2+} and reduce the defects density in narrow E_g PVSCs are essential for improving the performance and stability of all-perovskite tandem solar cells. For perovskite/organic hybrid and tandem solar cells, the synthesis of narrow E_g acceptors with extended absorption and low energy loss is crucial for their development.

Stability. Long-term operational stability is crucial for PVSCs to get into market. IEC 61646 test certification was established by International Electrotechnical Commission (IEC) to evaluate the long-term operational stability of PV modules, including temperature cycling test (−40 to +85 °C for 200 cycles), humidity freeze test (−40 to +85 °C and 85% RH for 10 cycles), and damp heat test (+85 °C and 85% RH for 1000 h). The target for PVSCs is to meet these requirements. Generally, the instability of PVSCs is mainly originated from the degradation of perovskite and/or CTMs under external stimuli, such as oxygen, moisture, heat, and light. A more comprehensive understanding of the device degradation mechanisms is crucial for solving the stability issues. Several aspects can be focused to enhance the long-term operational stability: (1) Developing perovskite compositions with superior intrinsic stability; (2) Passivating various defects of perovskite films can efficiently enhance device stability because the charged defects are closely related to the ion migration; (3) Optimizing interfaces in PVSCs are extremely important because the instability is coming from the defects caused by ion migration, therefore, the exploration of more stable CTMs to replace traditional TiO_2 and Spiro-OMeTAD will help stabilize the whole device; (4) Minimizing the reactions between perovskite component and metal electrodes to avoid the degradation of device. Replacing metal electrode with robust materials, such as sputtered ITO, will benefit the long-term device stability; (5) Developing advanced encapsulation techniques will dramatically improve the device stability by preventing the penetration of oxygen and water. (6) For the multijunction devices, apart from continuously enhancing their performance, more attention should be paid to investigate their long-term operational stability. A deeper understanding of the degradation mechanism is needed to provide better guidance for enhancing device stability.

Scale-up. Fabricating large-area devices is the essential step for PVSCs to be developed for commercialization. Developing suitable techniques for depositing large-area perovskites with uniform and compact morphology in air is very critical because they are far different from those observed in lab devices. A comprehensive understanding of perovskite crystal growth and film formation will guide the scalable deposition of perovskites. Doctor blading, slot die coating, screen printing and vapor-assisted deposition methods are the commonly used technology for high-performance PVSCs and PV modules. The detailed studies and optimizations of the techniques will promote the scale-up of PVSCs. In addition, developing appropriate strategies to realize scalable deposition of CTMs and electrodes are also crucial for the scale-up of PVSCs.

Toxicity. The toxicity issue is very critical for PVSCs to become environmental-friendly PV technology. The potential leakage of lead into environment due to the damages caused by the irresistible natural factors will result in carcinogenic and polluting risk. To solve the problems of toxicity, lead-free Sn-based PVSCs have been developed, but their champion PCEs are lower than 15%.[343-345] Meanwhile, the poor stability due to the oxidation of Sn^{2+} strongly limits the application in the real world. Further enhancing the performance and stability of lead-free PVSCs are essential in order for them to be utilized. Another strategy is to employ a protecting layer (lead absorbing materials or encapsulation coatings) to prevent the lead leakage. Although several reports have demonstrated the effectiveness of this strategy, it still calls for more research on designing and synthesizing new materials with superior lead-capture capability.

Conflicts of interest

There are no conflicts to declare.

Acknowledgements

This work was supported by the APRC Grants of the City University of Hong Kong (9380086, 9610421), Innovation and Technology Bureau supported programs (ITS/497/18FP, GHP/021/18SZ), the Office of Naval Research (N00014-17-1-2201), National Science Foundation (DMR-1608279), Natural Science Foundation of Guangdong Province (2019A1515010761), Guangdong-Hong Kong-Macao joint laboratory of optoelectronic and magnetic materials (No. 2019B121205002), the ECS grant (CityU 21301319) from the Research Grants Council of Hong Kong, Guangdong Major Project of Basic and Applied Basic Research (No. 2019B030302007), and the Air Force Office of Scientific Research (FA9550-18-1-0046). AJ acknowledges the support from the Lee Shau Kee Chair Professorship.

References

1 W. Shen, X. Chen, J. Qiu, J. A. Hayward, S. Sayeef, P. Osman, K. Meng and Z. Y. Dong, Renew. Sustain. Energy Rev, 2020, 133, 110301.

2 L. A. Zafoschnig, S. Nold and J. C. Goldschmidt, *IEEE J PHOTOVOLT*, 2020, **10**, 1632-1641.

3 K. Chen, S. Schünemann, S. Song and H. Tüysüz, *Chem. Soc. Rev.*, 2018, **47**, 7045-7077.

4 A. Rajagopal, K. Yao and A. K. Y. Jen, *Adv. Mater.*, 2018, **30**, 1800455.

5 A. Kojima, K. Teshima, Y. Shirai and T. Miyasaka, *J. Am. Chem. Soc.*, 2009, **131**, 6050-6051.

6 N. R. E. L. (NREL), *Best Research-Cell Efficiencies Chart*, https://www.nrel.gov/pv/cell-efficiency.html.

7 Z. Li, J. Zhang, S. Wu, X. Deng, F. Li, D. Liu, C. C. Lee, F. Lin, D. Lei, C.-C. Chueh, Z. Zhu and A. K. Y. Jen, *Nano Energy*, 2020, **78**, 105377.

8 G. Lee, M.-c. Kim, Y. W. Choi, N. Ahn, J. Jang, J. Yoon, S. M. Kim, J.-G. Lee, D. Kang and H. S. Jung, *Energy Environ. Sci.*, 2019, **12**, 3182-3191.

9 X. Hu, Z. Huang, F. Li, M. Su, Z. Huang, Z. Zhao, Z. Cai, X. Yang, X. Meng and P. Li, *Energy Environ. Sci.*, 2019, **12**, 979-987.

10 B. Shi, L. Duan, Y. Zhao, J. Luo and X. Zhang, *Adv. Mater.*, 2020, **32**, 1806474.

11 E. M. Tennyson, T. A. Doherty and S. D. Stranks, *Nat. Rev. Mater*, 2019, **4**, 573-587.

12 W.-J. Yin, T. Shi and Y. Yan, *Appl. Phys. Lett.*, 2014, **104**, 063903.

13 J. M. Ball and A. Petrozza, *Nat. Energy*, 2016, **1**, 1-13.

14 B. Chen, P. N. Rudd, S. Yang, Y. Yuan and J. Huang, *Chem. Soc. Rev.*, 2019, **48**, 3842-3867.

15 P. Calado, A. M. Telford, D. Bryant, X. Li, J. Nelson, B. C. O'Regan and P. R. Barnes, *Nat. Commun.*, 2016, **7**, 1-10.

16 Z. Li, C. Xiao, Y. Yang, S. P. Harvey, D. H. Kim, J. A. Christians, M. Yang, P. Schulz, S. U. Nanayakkara and C.-S. Jiang, *Energy Environ. Sci.*, 2017, **10**, 1234-1242.

17 J.-W. Lee, S.-H. Bae, N. De Marco, Y.-T. Hsieh, Z. Dai and Y. Yang, *Mater. Today Energy*, 2018, **7**, 149-160.

18 Z. Chu, M. Yang, P. Schulz, D. Wu, X. Ma, E. Seifert, L. Sun, X. Li, K. Zhu and K. Lai, *Nat. Commun.*, 2017, **8**, 1-8.

19 A. N. Cho and N. G. Park, *ChemSusChem*, 2017, **10**, 3687-3704.

20 T. H. Han, S. Tan, J. Xue, L. Meng, J. W. Lee and Y. Yang, *Adv. Mater.*, 2019, **31**, 1803515.

21 M. Vasilopoulou, A. Fakharuddin, A. G. Coutsolelos, P. Falaras, P. Argitis, A. R. bin Mohd Yusoff and M. K. Nazeeruddin, *Chem. Soc. Rev.*, 2020, **49**, 4496-4526.

22 N.-G. Park and H. Segawa, *ACS Photonics*, 2018, **5**, 2970-2977.

23 L. M. Pazos-Outón, T. P. Xiao and E. Yablonovitch, *J. Phys. Chem. Lett.*, 2018, **9**, 1703-1711.

24 A. De Vos, *J. Phys. D: Appl. Phys.*, 1980, **13**, 839.

25 F. Meillaud, A. Shah, C. Droz, E. Vallat-Sauvain and C. Miazza, *Sol. Energy Mater. Sol. Cells*, 2006, **90**, 2952-2959.

26 M. Saliba, J. P. Correa-Baena, M. Grätzel, A. Hagfeldt and A. Abate, *Angew. Chem. Int. Ed.*, 2018, **57**, 2554-2569.

27 T. Leijtens, K. A. Bush, R. Prasanna and M. D. McGehee, *Nat. Energy*, 2018, **3**, 828-838.

28 M. Jošt, L. Kegelmann, L. Korte and S. Albrecht, *Adv. Energy Mater.*, 2020, **10**, 1904102.

29 A. Al-Ashouri, E. Köhnen, B. Li, A. Magomedov, H. Hempel, P. Caprioglio, J. A. Márquez, A. B. M. Vilches, E. Kasparavicius and J. A. Smith, *Science*, 2020, **370**, 1300-1309.

30 Y. Yamada, T. Nakamura, M. Endo, A. Wakamiya and Y. Kanemitsu, *J. Am. Chem. Soc.*, 2014, **136**, 11610-11613.

31 Q. K. Wang, R. B. Wang, P. F. Shen, C. Li, Y. Q. Li, L. J. Liu, S. Duhm and J. X. Tang, *Adv. Mater. Interfaces*, 2015, **2**, 1400528.

32 Y.-C. Hsiao, T. Wu, M. Li, Q. Liu, W. Qin and B. Hu, *J. Mater. Chem. A*, 2015, **3**, 15372-15385.

33 A. M. Askar and K. Shankar, *J. Nanosci. Nanotechnol.*, 2016, **16**, 5890-5901.

34 M. Grätzel, *Nat. Mater.*, 2014, **13**, 838-842.

35 A. A. Zhumekenov, M. I. Saidaminov, M. A. Haque, E. Alarousu, S. P. Sarmah, B. Murali, I. Dursun, X.-H. Miao, A. L. Abdelhady and T. Wu, *ACS Energy Lett.*, 2016, **1**, 32-37.

36 Y. Zhao, A. M. Nardes and K. Zhu, *J. Phys. Chem. Lett.*, 2014, **5**, 490-494.

37 J. Yao, T. Kirchartz, M. S. Vezie, M. A. Faist, W. Gong, Z. He, H. Wu, J. Troughton, T. Watson and D. Bryant, *Phys. Rev. Appl.*, 2015, **4**, 014020.

38 M. Stolterfoht, P. Caprioglio, C. M. Wolff, J. A. Márquez, J. Nordmann, S. Zhang, D. Rothhardt, U. Hörmann, Y. Amir and A. Redinger, *Energy Environ. Sci.*, 2019, **12**, 2778-2788.

39 Y. Chen, N. Li, L. Wang, L. Li, Z. Xu, H. Jiao, P. Liu, C. Zhu, H. Zai and M. Sun, *Nat. Commun.*, 2019, **10**, 1-10.

40 G. Zheng, C. Zhu, J. Ma, X. Zhang, G. Tang, R. Li, Y. Chen, L. Li, J. Hu and J. Hong, *Nat. Commun.*, 2018, **9**, 1-11.

41 L. Zeng, S. Chen, K. Forberich, C. J. Brabec, Y. Mai and F. Guo, *Energy Environ. Sci.*, 2020, **13**, 4666-4690.

42 S. Sánchez, L. Pfeifer, N. Vlachopoulos and A. Hagfeldt, *Chem. Soc. Rev.*, 2021, **50**, 7108-7131.

43 S. Okita, E. Miyoshi, S. Sakane, T. Takaki, M. Ohno and Y. Shibuta, *Acta Mater.*, 2018, **153**, 108-116.

44 G. M. Maggioni and M. Mazzotti, *Cryst. Growth Des.*, 2019, **19**, 4698-4709.

45 M. He, B. Li, X. Cui, B. Jiang, Y. He, Y. Chen, D. O'Neil, P. Szymanski, M. A. Ei-Sayed and J. Huang, *Nat. Commun.*, 2017, **8**, 1-10.

46 W. S. Yang, J. H. Noh, N. J. Jeon, Y. C. Kim, S. Ryu, J. Seo and S. I. Seok, *Science*, 2015, **348**, 1234-1237.

47 L. Li, Y. Chen, Z. Liu, Q. Chen, X. Wang and H. Zhou, *Adv. Mater.*, 2016, **28**, 9862-9868.

48 B. Li, M. Li, C. Fei, G. Cao and J. Tian, *J. Mater. Chem. A*, 2017, **5**, 24168-24177.

49 D. P. McMeekin, Z. Wang, W. Rehman, F. Pulvirenti, J. B. Patel, N. K. Noel, M. B. Johnston, S. R. Marder, L. M. Herz and H. J. Snaith, *Adv. Mater.*, 2017, **29**, 1607039.

50 N. S. Dutta, N. K. Noel and C. B. Arnold, *J. Phys. Chem. Lett.*, 2020, **11**, 5980-5986.

51 K. Yan, M. Long, T. Zhang, Z. Wei, H. Chen, S. Yang and J. Xu, *J. Am. Chem. Soc.*, 2015, **137**, 4460-4468.

52 N. K. Noel, M. Congiu, A. J. Ramadan, S. Fearn, D. P. McMeekin, J. B. Patel, M. B. Johnston, B. Wenger and H. J. Snaith, *Joule*, 2017, **1**, 328-343.

53 J. Pan, C. Mu, Q. Li, W. Li, D. Ma and D. Xu, *Adv. Mater.*, 2016, **28**, 8309-8314.

54 Y. Guo, W. Sato, K. Shoyama and E. Nakamura, *J. Am. Chem. Soc.*, 2016, **138**, 5410-5416.

55 Y. Guo, W. Sato, K. Shoyama, H. Halim, Y. Itabashi, R. Shang and E. Nakamura, *J. Am. Chem. Soc.*, 2017, **139**, 9598-9604.

56 Y. Jo, K. S. Oh, M. Kim, K. H. Kim, H. Lee, C. W. Lee and D. S. Kim, *Adv. Mater. Interfaces*, 2016, **3**, 1500768.
57 Y. Wu, F. Xie, H. Chen, X. Yang, H. Su, M. Cai, Z. Zhou, T. Noda and L. Han, *Adv. Mater.*, 2017, **29**, 1701073.
58 K. Jung, W.-S. Chae, Y. C. Park, J. Kim and M.-J. Lee, *Chem. Eng. J.*, 2020, **380**, 122436.
59 Y. Zhang, P. Gao, E. Oveisi, Y. Lee, Q. Jeangros, G. Grancini, S. Paek, Y. Feng and M. K. Nazeeruddin, *J. Am. Chem. Soc.*, 2016, **138**, 14380-14387.
60 X. Liu, J. Wu, Q. Guo, Y. Yang, H. Luo, Q. Liu, X. Wang, X. He, M. Huang and Z. Lan, *J. Mater. Chem. A*, 2019, **7**, 11764-11770.
61 W. Zhou, D. Li, Z. Xiao, Z. Wen, M. Zhang, W. Hu, X. Wu, M. Wang, W. H. Zhang and Y. Lu, *Adv. Funct. Mater.*, 2019, **29**, 1901026.
62 X. Deng, Z. Cao, Y. Yuan, M. O. L. Chee, L. Xie, A. Wang, Y. Xiang, T. Li, P. Dong and L. Ding, *Coord. Chem. Rev.*, 2020, **420**, 213408.
63 J. Y. Seo, T. Matsui, J. Luo, J. P. Correa-Baena, F. Giordano, M. Saliba, K. Schenk, A. Ummadisingu, K. Domanski and M. Hadadian, *Adv. Energy Mater.*, 2016, **6**, 1600767.
64 H. Zhang, J. Cheng, D. Li, F. Lin, J. Mao, C. Liang, A. K. Y. Jen, M. Grätzel and W. C. Choy, *Adv. Mater.*, 2017, **29**, 1604695.
65 P. W. Liang, C. Y. Liao, C. C. Chueh, F. Zuo, S. T. Williams, X. K. Xin, J. Lin and A. K. Y. Jen, *Adv. Mater.*, 2014, **26**, 3748-3754.
66 M. Wang, B. Li, P. Siffalovic, L.-C. Chen, G. Cao and J. Tian, *J. Mater. Chem. A*, 2018, **6**, 15386-15394.
67 D. H. Kim, C. P. Muzzillo, J. Tong, A. F. Palmstrom, B. W. Larson, C. Choi, S. P. Harvey, S. Glynn, J. B. Whitaker and F. Zhang, *Joule*, 2019, **3**, 1734-1745.
68 M. Kim, G.-H. Kim, T. K. Lee, I. W. Choi, H. W. Choi, Y. Jo, Y. J. Yoon, J. W. Kim, J. Lee, D. Huh, H. Lee, S. K. Kwak, J. Y. Kim and D. S. Kim, *Joule*, 2019, **3**, 2179-2192.
69 C. Wang, D. Zhao, Y. Yu, N. Shrestha, C. R. Grice, W. Liao, A. J. Cimaroli, J. Chen, R. J. Ellingson and X. Zhao, *Nano Energy*, 2017, **35**, 223-232.
70 Y. Yu, C. Wang, C. R. Grice, N. Shrestha, D. Zhao, W. Liao, L. Guan, R. A. Awni, W. Meng and A. J. Cimaroli, *ACS Energy Lett.*, 2017, **2**, 1177-1182.
71 X. Zhou, Y. Wang, C. Li and T. Wu, *Chem. Eng. J.*, 2019, **372**, 46-52.
72 Y. Zhang, Z. Fei, P. Gao, Y. Lee, F. F. Tirani, R. Scopelliti, Y. Feng, P. J. Dyson and M. K. Nazeeruddin, *Adv. Mater.*, 2017, **29**, 1702157.
73 D. T. Moore, K. W. Tan, H. Sai, K. P. Barteau, U. Wiesner and L. A. Estroff, *Chem. Mater.*, 2015, **27**, 3197-3199.
74 T.-H. Han, J.-W. Lee, C. Choi, S. Tan, C. Lee, Y. Zhao, Z. Dai, N. De Marco, S.-J. Lee and S.-H. Bae, *Nat. Commun.*, 2019, **10**, 1-10.
75 Y. Zhao, P. Zhu, M. Wang, S. Huang, Z. Zhao, S. Tan, T. H. Han, J. W. Lee, T. Huang and R. Wang, *Adv. Mater.*, 2020, **32**, 1907769.
76 Y. Wu, A. Islam, X. Yang, C. Qin, J. Liu, K. Zhang, W. Peng and L. Han, *Energy Environ. Sci.*, 2014, **7**, 2934-2938.
77 Z. Xiao, C. Bi, Y. Shao, Q. Dong, Q. Wang, Y. Yuan, C. Wang, Y. Gao and J. Huang, *Energy Environ. Sci.*, 2014, **7**, 2619-2623.
78 H. Zhang, J. Mao, H. He, D. Zhang, H. L. Zhu, F. Xie, K. S. Wong, M. Grätzel and W. C. Choy, *Adv. Energy Mater.*, 2015, **5**, 1501354.
79 C. Momblona, L. Gil-Escrig, E. Bandiello, E. M. Hutter, M. Sessolo, K. Lederer, J. Blochwitz-Nimoth and H. J. Bolink, *Energy Environ. Sci.*, 2016, **9**, 3456-3463.
80 W. Tress, N. Marinova, O. Inganäs, M. K. Nazeeruddin, S. M. Zakeeruddin and M. Graetzel, *Adv. Energy Mater.*, 2015, **5**, 1400812.
81 G. J. A. Wetzelaer, M. Scheepers, A. M. Sempere, C. Momblona, J. Ávila and H. J. Bolink, *Adv. Mater.*, 2015, **27**, 1837-1841.
82 T. Leijtens, G. E. Eperon, A. J. Barker, G. Grancini, W. Zhang, J. M. Ball, A. R. S. Kandada, H. J. Snaith and A. Petrozza, *Energy Environ. Sci.*, 2016, **9**, 3472-3481.
83 J. Peng, Y. Wu, W. Ye, D. A. Jacobs, H. Shen, X. Fu, Y. Wan, N. Wu, C. Barugkin and H. T. Nguyen, *Energy Environ. Sci.*, 2017, **10**, 1792-1800.
84 Y. Fang, C. Bi, D. Wang and J. Huang, *ACS Energy Lett.*, 2017, **2**, 782-794.
85 X. Liu, F. Lin, C.-C. Chueh, Q. Chen, T. Zhao, P.-W. Liang, Z. Zhu, Y. Sun and A. K.-Y. Jen, *Nano Energy*, 2016, **30**, 417-425.
86 J. Xu, A. Buin, A. H. Ip, W. Li, O. Voznyy, R. Comin, M. Yuan, S. Jeon, Z. Ning and J. J. McDowell, *Nat. Commun.*, 2015, **6**, 1-8.
87 C.-H. Chiang and C.-G. Wu, *Nat. Photonics*, 2016, **10**, 196-200.
88 A. Abate, M. Saliba, D. J. Hollman, S. D. Stranks, K. Wojciechowski, R. Avolio, G. Grancini, A. Petrozza and H. J. Snaith, *Nano Lett.*, 2014, **14**, 3247-3254.
89 D. W. DeQuilettes, S. Koch, S. Burke, R. K. Paranji, A. J. Shropshire, M. E. Ziffer and D. S. Ginger, *ACS Energy Lett.*, 2016, **1**, 438-444.
90 H. Chen, T. Liu, P. Zhou, S. Li, J. Ren, H. He, J. Wang, N. Wang and S. Guo, *Adv. Mater.*, 2020, **32**, 1905661.
91 S. Yang, J. Dai, Z. Yu, Y. Shao, Y. Zhou, X. Xiao, X. C. Zeng and J. Huang, *J. Am. Chem. Soc.*, 2019, **141**, 5781-5787.
92 S. Yang, S. Chen, E. Mosconi, Y. Fang, X. Xiao, C. Wang, Y. Zhou, Z. Yu, J. Zhao and Y. Gao, *Science*, 2019, **365**, 473-478.
93 F. Zhang, D. Bi, N. Pellet, C. Xiao, Z. Li, J. J. Berry, S. M. Zakeeruddin, K. Zhu and M. Grätzel, *Energy Environ. Sci.*, 2018, **11**, 3480-3490.
94 T. Zhao, C.-C. Chueh, Q. Chen, A. Rajagopal and A. K.-Y. Jen, *ACS Energy Lett.*, 2016, **1**, 757-763.
95 Q. Jiang, Y. Zhao, X. Zhang, X. Yang, Y. Chen, Z. Chu, Q. Ye, X. Li, Z. Yin and J. You, *Nat. Photonics*, 2019, **13**, 460-466.
96 Z. Li, J. Zhang, S. Wu, X. Deng, F. Li, D. Liu, C. C. Lee, F. Lin, D. Lei and C.-C. Chueh, *Nano Energy*, 2020, **78**, 105377.
97 F. Li, X. Deng, F. Qi, Z. Li, D. Liu, D. Shen, M. Qin, S. Wu, F. Lin, S.-H. Jang, J. Zhang, X. Lu, D. Lei, C.-S. Lee, Z. Zhu and A. K. Y. Jen, *J. Am. Chem. Soc.*, 2020, **142**, 20134-20142.
98 K. Liu, Q. Liang, M. Qin, D. Shen, H. Yin, Z. Ren, Y. Zhang, H. Zhang, P. W. Fong and Z. Wu, *Joule*, 2020, **4**, 2404-2425.
99 X. Zheng, Y. Deng, B. Chen, H. Wei, X. Xiao, Y. Fang, Y. Lin, Z. Yu, Y. Liu and Q. Wang, *Adv. Mater.*, 2018, **30**, 1803428.
100 D. Wang, L. Huang, Q. Chen, L. Hu, F. Zeng, X. Zhou, L. Zhang, C. Liu, X. Wang and L. Yan, *Chem. Commun.*, 2020, **56**, 6929-6932.
101 X. Zheng, B. Chen, J. Dai, Y. Fang, Y. Bai, Y. Lin, H. Wei, X. C. Zeng and J. Huang, *Nat. Energy*, 2017, **2**, 17102.
102 Y. Wang, M. I. Dar, L. K. Ono, T. Zhang, M. Kan, Y. Li, L. Zhang, X. Wang, Y. Yang and X. Gao, *Science*, 2019, **365**, 591-595.
103 L. Wang, H. Zhou, J. Hu, B. Huang, M. Sun, B. Dong, G. Zheng, Y. Huang, Y. Chen, L. Li, Z. Xu, N. Li, Z. Liu, Q. Chen, L.-D. Sun and C.-h. Yan, *Science*, 2019, **363**, 265-270.
104 N. Li, S. Tao, Y. Chen, X. Niu, C. K. Onwudinanti, C. Hu, Z. Qiu,

Z. Xu, G. Zheng, L. Wang, Y. Zhang, L. Li, H. Liu, Y. Lun, J. Hong, X. Wang, Y. Liu, H. Xie, Y. Gao, Y. Bai, S. Yang, G. Brocks, Q. Chen and H. Zhou, *Nat. Energy*, 2019, **4**, 408-415.

105 X. Huang, H. Guo, K. Wang and X. Liu, *Org. Electron.*, 2017, **41**, 42-48.

106 W. Zhang, X. Liu, B. He, Z. Gong, J. Zhu, Y. Ding, H. Chen and Q. Tang, *ACS Appl. Mater. Interfaces*, 2020, **12**, 4540-4548.

107 A. Wang, X. Deng, J. Wang, S. Wang, X. Niu, F. Hao and L. Ding, *Nano Energy*, 2020, 105631.

108 X. Zhu, M. Du, J. Feng, H. Wang, Z. Xu, L. Wang, S. Zuo, C. Wang, Z. Wang, C. Zhang, X. Ren, S. Priya, D. Yang and S. Liu, *Angew. Chem. Int. Ed.*, 2020, DOI:10.1002/anie.202010987.

109 G. Tong, H. Li, G. Li, T. Zhang, C. Li, L. Yu, J. Xu, Y. Jiang, Y. Shi and K. Chen, *Nano Energy*, 2018, **48**, 536-542.

110 T. Wu, D. Cui, X. Liu, X. Meng, Y. Wang, T. Noda, H. Segawa, X. Yang, Y. Zhang and L. Han, *Solar RRL*, 2020, **4**, 2000240.

111 M.-c. Kim, B. J. Kim, D.-Y. Son, N.-G. Park, H. S. Jung and M. Choi, *Nano Lett.*, 2016, **16**, 5756-5763.

112 K. T. Cho, S. Paek, G. Grancini, C. Roldán-Carmona, P. Gao, Y. Lee and M. K. Nazeeruddin, *Energy Environ. Sci.*, 2017, **10**, 621-627.

113 W. S. Subhani, K. Wang, M. Du, X. Wang and S. Liu, *Adv. Energy Mater.*, 2019, **9**, 1803785.

114 H. W. Qiao, S. Yang, Y. Wang, X. Chen, T. Y. Wen, L. J. Tang, Q. Cheng, Y. Hou, H. Zhao and H. G. Yang, *Adv. Mater.*, 2019, **31**, 1804217.

115 M. U. Rothmann, J. S. Kim, J. Borchert, K. B. Lohmann, C. M. O'Leary, A. A. Sheader, L. Clark, H. J. Snaith, M. B. Johnston, P. D. Nellist and L. M. Herz, *Science*, 2020, **370**, eabb5940.

116 Z. Wang, Q. Lin, F. P. Chmiel, N. Sakai, L. M. Herz and H. J. Snaith, *Nat. Energy*, 2017, **2**, 17135.

117 D. S. Lee, J. S. Yun, J. Kim, A. M. Soufiani, S. Chen, Y. Cho, X. Deng, J. Seidel, S. Lim and S. Huang, *ACS Energy Lett.*, 2018, **3**, 647-654.

118 G. Grancini, C. Roldán-Carmona, I. Zimmermann, E. Mosconi, X. Lee, D. Martineau, S. Narbey, F. Oswald, F. De Angelis and M. Graetzel, *Nat. Commun.*, 2017, **8**, 15684.

119 Q. Yao, Q. Xue, Z. Li, K. Zhang, T. Zhang, N. Li, S. Yang, C. J. Brabec, H. L. Yip and Y. Cao, *Adv. Mater.*, 2020, **32**, 2000571.

120 T. Liu, J. Guo, D. Lu, Z. Xu, Q. Fu, N. Zheng, Z. Xie, X. Wan, X. Zhang and Y. Liu, *ACS nano*, 2021, **15**, 7811-7820.

121 K. Liu, S. Yuan, Y. Xian, Y. Long, Q. Yao, N. U. Rahman, Y. Guo, M. Sun, Q. Xue and H. L. Yip, *Small*, 2021, 2100888.

122 T. Zhang, M. I. Dar, G. Li, F. Xu, N. Guo, M. Grätzel and Y. Zhao, *Sci. Adv.*, 2017, **3**, e1700841.

123 T. Niu, J. Lu, M.-C. Tang, D. Barrit, D.-M. Smilgies, Z. Yang, J. Li, Y. Fan, T. Luo and I. McCulloch, *Energy Environ. Sci.*, 2018, **11**, 3358-3366.

124 E. Ruggeri, M. Anaya, K. Gałkowski, G. Delport, F. U. Kosasih, A. Abfalterer, S. Mackowski, C. Ducati and S. D. Stranks, *Adv. Mater.*, 2019, **31**, 1905247.

125 D. Bi, P. Gao, R. Scopelliti, E. Oveisi, J. Luo, M. Grätzel, A. Hagfeldt and M. K. Nazeeruddin, *Adv. Mater.*, 2016, **28**, 2910-2915.

126 J. Fan, Y. Ma, C. Zhang, C. Liu, W. Li, R. E. Schropp and Y. Mai, *Adv. Energy Mater.*, 2018, **8**, 1703421.

127 P. Liu, Y. Xian, W. Yuan, Y. Long, K. Liu, N. U. Rahman, W. Li and J. Fan, *Adv. Energy Mater.*, 2020, **10**, 1903654.

128 Y. Bai, S. Xiao, C. Hu, T. Zhang, X. Meng, H. Lin, Y. Yang and S. Yang, *Adv. Energy Mater.*, 2017, **7**, 1701038.

129 F. Wang, X. Jiang, H. Chen, Y. Shang, H. Liu, J. Wei, W. Zhou, H. He, W. Liu and Z. Ning, *Joule*, 2018, **2**, 2732-2743.

130 T. Zhang, M. Long, M. Qin, X. Lu, S. Chen, F. Xie, L. Gong, J. Chen, M. Chu and Q. Miao, *Joule*, 2018, **2**, 2706-2721.

131 Y. Liu, S. Akin, L. Pan, R. Uchida, N. Arora, J. V. Milić, A. Hinderhofer, F. Schreiber, A. R. Uhl and S. M. Zakeeruddin, *Sci. Adv.*, 2019, **5**, eaaw2543.

132 T. Zhou, H. Lai, T. Liu, D. Lu, X. Wan, X. Zhang, Y. Liu and Y. Chen, *Adv. Mater.*, 2019, **31**, 1901242.

133 Y.-W. Jang, S. Lee, K. M. Yeom, K. Jeong, K. Choi, M. Choi and J. H. Noh, *Nat. Energy*, 2021, **6**, 63-71.

134 P. Chen, Y. Bai, S. Wang, M. Lyu, J.-H. Yun and L. Wang, *Adv. Funct. Mater.*, 2018, **28**, 1706923.

135 G. Grancini, C. Roldan-Carmona, I. Zimmermann, E. Mosconi, X. Lee, D. Martineau, S. Narbey, F. Oswald, F. De Angelis, M. Graetzel and M. K. Nazeeruddin, *Nat Commun*, 2017, **8**, 15684.

136 C. Ran, J. Xi, W. Gao, F. Yuan, T. Lei, B. Jiao, X. Hou and Z. Wu, *ACS Energy Lett.*, 2018, **3**, 713-721.

137 T. Ye, A. Bruno, G. Han, T. M. Koh, J. Li, N. F. Jamaludin, C. Soci, S. G. Mhaisalkar and W. L. Leong, *Adv. Funct. Mater.*, 2018, **28**, 1801654.

138 M. H. Li, H. H. Yeh, Y. H. Chiang, U. S. Jeng, C. J. Su, H. W. Shiu, Y. J. Hsu, N. Kosugi, T. Ohigashi, Y. A. Chen, P. S. Shen, P. Chen and T. F. Guo, *Adv. Mater.*, 2018, **30**, 1801401.

139 K. T. Cho, G. Grancini, Y. Lee, E. Oveisi, J. Ryu, O. Almora, M. Tschumi, P. A. Schouwink, G. Seo, S. Heo, J. Park, J. Jang, S. Paek, G. Garcia-Belmonte and M. K. Nazeeruddin, *Energy Environ. Sci.*, 2018, **11**, 952-959.

140 S. Gharibzadeh, B. Abdollahi Nejand, M. Jakoby, T. Abzieher, D. Hauschild, S. Moghadamzadeh, J. A. Schwenzer, P. Brenner, R. Schmager, A. A. Haghighirad, L. Weinhardt, U. Lemmer, B. S. Richards, I. A. Howard and U. W. Paetzold, *Adv. Energy Mater.*, 2019, **9**, 1803699.

141 D. Lin, T. Zhang, J. Wang, M. Long, F. Xie, J. Chen, B. Wu, T. Shi, K. Yan, W. Xie, P. Liu and J. Xu, *Nano Energy*, 2019, **59**, 619-625.

142 T. Zhang, M. Long, M. Qin, X. Lu, S. Chen, F. Xie, L. Gong, J. Chen, M. Chu, Q. Miao, Z. Chen, W. Xu, P. Liu, W. Xie and J.-b. Xu, *Joule*, 2018, **2**, 2706-2721.

143 C. Zhang, S. Wu, L. Tao, G. M. Arumugam, C. Liu, Z. Wang, S. Zhu, Y. Yang, J. Lin and X. Liu, *Adv. Energy Mater.*, 2020, **10**, 2002004.

144 M. He, J. Liang, Z. Zhang, Y. Qiu, Z. Deng, H. Xu, J. Wang, Y. Yang, Z. Chen and C.-C. Chen, *J. Mater. Chem. A*, 2020, **8**, 25831-25841.

145 S. Wu, J. Zhang, Z. Li, D. Liu, M. Qin, S. H. Cheung, X. Lu, D. Lei, S. K. So, Z. Zhu and A. K.-Y. Jen, *Joule*, 2020, **4**, 1248-1262.

146 J. Li, M. Wu, G. Yang, D. Zhang, Z. Wang, D. Zheng and J. Yu, *Sol. Energy*, 2020, **205**, 44-50.

147 L. Gao, I. Spanopoulos, W. Ke, S. Huang, I. Hadar, L. Chen, X. Li, G. Yang and M. G. Kanatzidis, *ACS Energy Lett.*, 2019, **4**, 1763-1769.

148 M. M. Elsenety, M. Antoniadou, N. Balis, A. Kaltzoglou, L. Sygellou, A. Stergiou, N. Tagmatarchis and P. Falaras, *ACS Applied Energy Materials*, 2020, **3**, 2465-2477.

149 N. Yang, C. Zhu, Y. Chen, H. Zai, C. Wang, X. Wang, H. Wang, S. Ma, Z. Gao and X. Wang, *Energy Environ. Sci.*, 2020, **13**, 4344-4352.

150 M. Cha, P. Da, J. Wang, W. Wang, Z. Chen, F. Xiu, G. Zheng and Z.-S. Wang, *J. Am. Chem. Soc.*, 2016, **138**, 8581-8587.

151 M. Que, Z. Dai, H. Yang, H. Zhu, Y. Zong, W. Que, N. P. Padture, Y. Zhou and O. Chen, *ACS Energy Lett.*, 2019, **4**,

1970-1975.
152 X. Zheng, J. Troughton, N. Gasparini, Y. Lin, M. Wei, Y. Hou, J. Liu, K. Song, Z. Chen and C. Yang, *Joule*, 2019, **3**, 1963-1976.
153 S. Zhang, Y. J. Yoon, X. Cui, Y. Chang, M. Zhang, S. Liang, C.-H. Lu and Z. Lin, *J. Mater. Chem. A*, 2020, **8**, 26098-26108.
154 J. Zhang, D. Bai, Z. Jin, H. Bian, K. Wang, J. Sun, Q. Wang and S. Liu, *Adv. Energy Mater.*, 2018, **8**, 1703246.
155 Z. Xiao, Y. Yuan, Y. Shao, Q. Wang, Q. Dong, C. Bi, P. Sharma, A. Gruverman and J. Huang, *Nat. Mater.*, 2015, **14**, 193-198.
156 B. Chen, M. Yang, X. Zheng, C. Wu, W. Li, Y. Yan, J. Bisquert, G. Garcia-Belmonte, K. Zhu and S. Priya, *J. Phys. Chem. Lett.*, 2015, **6**, 4693-4700.
157 T. Minemoto and M. Murata, *Sol. Energy Mater. Sol. Cells*, 2015, **133**, 8-14.
158 Z. Zhou, S. Pang, Z. Liu, H. Xu and G. Cui, *J. Mater. Chem. A*, 2015, **3**, 19205-19217.
159 H. Lu, Y. Liu, P. Ahlawat, A. Mishra, W. R. Tress, F. T. Eickemeyer, Y. Yang, F. Fu, Z. Wang, C. E. Avalos, B. I. Carlsen, A. Agarwalla, X. Zhang, X. Li, Y. Zhan, S. M. Zakeeruddin, L. Emsley, U. Rothlisberger, L. Zheng, A. Hagfeldt and M. Gratzel, *Science*, 2020, **370**, eabb8985.
160 G. Kim, H. Min, K. S. Lee, S. M. Yoon and S. I. Seok, *Science*, 2020, **370**, 108-112.
161 H. Min, M. Kim, S.-U. Lee, H. Kim, G. Kim, K. Choi, J. H. Lee and S. I. Seok, *Science*, 2019, **366**, 749-753.
162 S. K. Pathak, A. Abate, P. Ruckdeschel, B. Roose, K. C. Gödel, Y. Vaynzof, A. Santhala, S. I. Watanabe, D. J. Hollman and N. Noel, *Adv. Funct. Mater.*, 2014, **24**, 6046-6055.
163 W. Göpel, J. Anderson, D. Frankel, M. Jaehnig, K. Phillips, J. Schäfer and G. Rocker, *Surf. Sci.*, 1984, **139**, 333-346.
164 S. Sidhik, J. Velusamy, E. De la Rosa, S. A. Pérez-García, G. Ramos-Ortiz and T. López-Luke, *Carbon*, 2019, **146**, 388-398.
165 Y. Ai, W. Liu, C. Shou, J. Yan, N. Li, Z. Yang, W. Song, B. Yan, J. Sheng and J. Ye, *Sol. Energy*, 2019, **194**, 541-547.
166 S. You, H. Wang, S. Bi, J. Zhou, L. Qin, X. Qiu, Z. Zhao, Y. Xu, Y. Zhang and X. Shi, *Adv. Mater.*, 2018, **30**, 1706924.
167 T. Liu, J. Zhang, X. Wu, H. Liu, F. Li, X. Deng, F. Lin, X. Li, Z. Zhu and A. K.-Y. Jen, *Solar RRL*, **4**, 2000205.
168 X. Cui, Y. Chen, M. Zhang, Y. W. Harn, J. Qi, L. Gao, Z. L. Wang, J. Huang, Y. Yang and Z. Lin, *Energy Environ. Sci.*, 2020, **13**, 1743-1752.
169 B. Wang, M. Zhang, X. Cui, Z. Wang, M. Rager, Y. Yang, Z. Zou, Z. L. Wang and Z. Lin, *Angew. Chem. Int. Ed.*, 2020, **59**, 1611-1618.
170 J. Wei, F. Guo, X. Wang, K. Xu, M. Lei, Y. Liang, Y. Zhao and D. Xu, *Adv. Mater.*, 2018, **30**, 1805153.
171 B. Tu, Y. Shao, W. Chen, Y. Wu, X. Li, Y. He, J. Li, F. Liu, Z. Zhang and Y. Lin, *Adv. Mater.*, 2019, **31**, 1805944.
172 K. Yao, S. Leng, Z. Liu, L. Fei, Y. Chen, S. Li, N. Zhou, J. Zhang, Y.-X. Xu and L. Zhou, *Joule*, 2019, **3**, 417-431.
173 J. Cao, B. Wu, R. Chen, Y. Wu, Y. Hui, B. W. Mao and N. Zheng, *Adv. Mater.*, 2018, **30**, 1705596.
174 S. S. Shin, E. J. Yeom, W. S. Yang, S. Hur, M. G. Kim, J. Im, J. Seo, J. H. Noh and S. I. Seok, *Science*, 2017, **356**, 167-171.
175 S. S. Shin, W. S. Yang, J. H. Noh, J. H. Suk, N. J. Jeon, J. H. Park, J. S. Kim, W. M. Seong and S. I. Seok, *Nat. Commun.*, 2015, **6**, 1-8.
176 T. Mahmoudi, Y. Wang and Y. B. Hahn, *Adv. Energy Mater.*, 2020, **10**, 1903369.
177 J. Chung, S. S. Shin, G. Kim, N. J. Jeon, T.-Y. Yang, J. H. Noh and J. Seo, *Joule*, 2019, **3**, 1977-1985.
178 M. Zhang, X. Cui, Y. Wang, B. Wang, M. Ye, W. Wang, C. Ma and Z. Lin, *Nano Energy*, 2020, **71**, 104620.
179 S. You, H. Wang, S. Bi, J. Zhou, L. Qin, X. Qiu, Z. Zhao, Y. Xu, Y. Zhang, X. Shi, H. Zhou and Z. Tang, *Adv. Mater.*, 2018, **30**, 1706924.
180 T. Singh, S. Öz, A. Sasinska, R. Frohnhoven, S. Mathur and T. Miyasaka, *Adv. Funct. Mater.*, 2018, **28**, 1706287.
181 H. Tan, A. Jain, O. Voznyy, X. Lan, F. P. G. De Arquer, J. Z. Fan, R. Quintero-Bermudez, M. Yuan, B. Zhang and Y. Zhao, *Science*, 2017, **355**, 722-726.
182 Y. Zhang, X. Liu, P. Li, Y. Duan, X. Hu, F. Li and Y. Song, *Nano Energy*, 2019, **56**, 733-740.
183 C. Chen, D. Liu, Y. Wu, W. Bi, X. Sun, X. Chen, W. Liu, L. Xu, H. Song and Q. Dai, *Nano Energy*, 2018, **53**, 849-862.
184 J.-Y. Seo, R. Uchida, H.-S. Kim, Y. Saygili, J. Luo, C. Moore, J. Kerrod, A. Wagstaff, M. Eklund, R. McIntyre, N. Pellet, S. M. Zakeeruddin, A. Hagfeldt and M. Grätzel, *Adv. Funct. Mater.*, 2018, **28**, 1705763.
185 M. M. Tavakoli, P. Yadav, R. Tavakoli and J. Kong, *Adv. Energy Mater.*, 2018, **8**, 1800794.
186 J. Wei, F. Guo, X. Wang, K. Xu, M. Lei, Y. Liang, Y. Zhao and D. Xu, *Adv. Mater.*, 2018, **30**, 1805153.
187 B. Tu, Y. Shao, W. Chen, Y. Wu, X. Li, Y. He, J. Li, F. Liu, Z. Zhang, Y. Lin, X. Lan, L. Xu, X. Shi, A. M. C. Ng, H. Li, L. W. Chung, A. B. Djurisic and Z. He, *Adv. Mater.*, 2019, **31**, 1805944.
188 Y. Lee, S. Lee, G. Seo, S. Paek, K. T. Cho, A. J. Huckaba, M. Calizzi, D. W. Choi, J. S. Park, D. Lee, H. J. Lee, A. M. Asiri and M. K. Nazeeruddin, *Adv Sci (Weinh)*, 2018, **5**, 1800130.
189 K. Liu, S. Chen, J. Wu, H. Zhang, M. Qin, X. Lu, Y. Tu, Q. Meng and X. Zhan, *Energy Environ. Sci.*, 2018, **11**, 3463-3471.
190 Z. Liu, K. Deng, J. Hu and L. Li, *Angew. Chem. Int. Ed. Engl.*, 2019, **131**, 11621-11628.
191 M. M. Tavakoli, M. Saliba, P. Yadav, P. Holzhey, A. Hagfeldt, S. M. Zakeeruddin and M. Grätzel, *Adv. Energy Mater.*, 2019, **9**, 1802646.
192 R. Azmi, C. L. Lee, I. H. Jung and S. Y. Jang, *Adv. Energy Mater.*, 2018, **8**, 1702934.
193 K. Yao, S. Leng, Z. Liu, L. Fei, Y. Chen, S. Li, N. Zhou, J. Zhang, Y.-X. Xu, L. Zhou, H. Huang and A. K. Y. Jen, *Joule*, 2019, **3**, 417-431.
194 R. Chen, J. Cao, Y. Duan, Y. Hui, T. T. Chuong, D. Ou, F. Han, F. Cheng, X. Huang, B. Wu and N. Zheng, *J. Am. Chem. Soc.*, 2019, **141**, 541-547.
195 M. Saliba, S. Orlandi, T. Matsui, S. Aghazada, M. Cavazzini, J.-P. Correa-Baena, P. Gao, R. Scopelliti, E. Mosconi, K.-H. Dahmen, F. De Angelis, A. Abate, A. Hagfeldt, G. Pozzi, M. Graetzel and M. K. Nazeeruddin, *Nat. Energy*, 2016, **1**, 15017.
196 N. J. Jeon, H. Na, E. H. Jung, T.-Y. Yang, Y. G. Lee, G. Kim, H.-W. Shin, S. Il Seok, J. Lee and J. Seo, *Nat. Energy*, 2018, **3**, 682-689.
197 F. Zhang, Z. Wang, H. Zhu, N. Pellet, J. Luo, C. Yi, X. Liu, H. Liu, S. Wang, X. Li, Y. Xiao, S. M. Zakeeruddin, D. Bi and M. Grätzel, *Nano Energy*, 2017, **41**, 469-475.
198 B. Xu, J. Zhang, Y. Hua, P. Liu, L. Wang, C. Ruan, Y. Li, G. Boschloo, E. M. J. Johansson, L. Kloo, A. Hagfeldt, A. K. Y. Jen and L. Sun, *Chem*, 2017, **2**, 676-687.
199 Q. Q. Ge, J. Y. Shao, J. Ding, L. Y. Deng, W. K. Zhou, Y. X. Chen, J. Y. Ma, L. J. Wan, J. Yao, J. S. Hu and Y. W. Zhong, *Angew. Chem. Int. Ed. Engl.*, 2018, **57**, 10959-10965.
200 K. Gao, B. Xu, C. Hong, X. Shi, H. Liu, X. Li, L. Xie and A. K. Y.

Jen, *Adv. Energy Mater.*, 2018, **8**, 1800809.
201 B. Xu, Z. Zhu, J. Zhang, H. Liu, C.-C. Chueh, X. Li and A. K. Y. Jen, *Adv. Energy Mater.*, 2017, **7**, 1700683.
202 Y. Wang, W. Chen, L. Wang, B. Tu, T. Chen, B. Liu, K. Yang, C. W. Koh, X. Zhang, H. Sun, G. Chen, X. Feng, H. Y. Woo, A. B. Djurisic, Z. He and X. Guo, *Adv. Mater.*, 2019, **31**, 1902781.
203 M. Jeong, I. W. Choi, E. M. Go, Y. Cho, M. Kim, B. Lee, S. Jeong, Y. Jo, H. W. Choi and J. Lee, *Science*, 2020, **369**, 1615-1620.
204 E. H. Jung, N. J. Jeon, E. Y. Park, C. S. Moon, T. J. Shin, T.-Y. Yang, J. H. Noh and J. Seo, *Nature*, 2019, **567**, 511-515.
205 W. S. Yang, B.-W. Park, E. H. Jung, N. J. Jeon, Y. C. Kim, D. U. Lee, S. S. Shin, J. Seo, E. K. Kim and J. H. Noh, *Science*, 2017, **356**, 1376-1379.
206 J. H. Heo, H. J. Han, D. Kim, T. K. Ahn and S. H. Im, *Energy Environ. Sci.*, 2015, **8**, 1602-1608.
207 F. Cai, J. Cai, L. Yang, W. Li, R. S. Gurney, H. Yi, A. Iraqi, D. Liu and T. Wang, *Nano Energy*, 2018, **45**, 28-36.
208 L. Zhang, C. Liu, J. Zhang, X. Li, C. Cheng, Y. Tian, A. K. Y. Jen and B. Xu, *Adv. Mater.*, 2018, **30**, 1804028.
209 G.-W. Kim, J. Lee, G. Kang, T. Kim and T. Park, *Adv. Energy Mater.*, 2018, **8**, 1701935.
210 N. Arora, M. I. Dar, A. Hinderhofer, N. Pellet, F. Schreiber, S. M. Zakeeruddin and M. Grätzel, *Science*, 2017, **358**, 768-771.
211 H. Zhang, H. Wang, W. Chen and A. K. Y. Jen, *Adv. Mater.*, 2017, **29**, 1604984.
212 H. Zhang, H. Wang, H. Zhu, C.-C. Chueh, W. Chen, S. Yang and A. K. Y. Jen, *Adv. Energy Mater.*, 2018, **8**, 1702762.
213 C. Liu, X. Zhou, S. Chen, X. Zhao, S. Dai and B. Xu, *Adv Sci (Weinh)*, 2019, **6**, 1801169.
214 Z.-K. Yu, W.-F. Fu, W.-Q. Liu, Z.-Q. Zhang, Y.-J. Liu, J.-L. Yan, T. Ye, W.-T. Yang, H.-Y. Li and H.-Z. Chen, *Chin. Chem. Lett.*, 2017, **28**, 13-18.
215 F. Xie, C.-C. Chen, Y. Wu, X. Li, M. Cai, X. Liu, X. Yang and L. Han, *Energy Environ. Sci.*, 2017, **10**, 1942-1949.
216 Y. C. Kim, T. Y. Yang, N. J. Jeon, J. Im, S. Jang, T. J. Shin, H. W. Shin, S. Kim, E. Lee, S. Kim, J. H. Noh, S. I. Seok and J. Seo, *Energy Environ. Sci.*, 2017, **10**, 2109-2116.
217 X. Jiang, D. Wang, Z. Yu, W. Ma, H.-B. Li, X. Yang, F. Liu, A. Hagfeldt and L. Sun, *Adv. Energy Mater.*, 2019, **9**, 1803287.
218 M. Cheng, Y. Li, M. Safdari, C. Chen, P. Liu, L. Kloo and L. Sun, *Adv. Energy Mater.*, 2017, **7**, 1602556.
219 K. Yao, F. Li, Q. He, X. Wang, Y. Jiang, H. Huang and A. K.-Y. Jen, *Nano Energy*, 2017, **40**, 155-162.
220 W. Chen, Y. Zhou, L. Wang, Y. Wu, B. Tu, B. Yu, F. Liu, H. W. Tam, G. Wang and A. B. Djurišić, *Adv. Mater.*, 2018, **30**, 1800515.
221 A. Magomedov, A. Al-Ashouri, E. Kasparavičius, S. Strazdaite, G. Niaura, M. Jošt, T. Malinauskas, S. Albrecht and V. Getautis, *Adv. Energy Mater.*, 2018, **8**, 1801892.
222 E. Yalcin, M. Can, C. Rodriguez-Seco, E. Aktas, R. Pudi, W. Cambarau, S. Demic and E. Palomares, *Energy Environ. Sci.*, 2019, **12**, 230-237.
223 M. Abdi-Jalebi, M. I. Dar, S. P. Senanayak, A. Sadhanala, Z. Andaji-Garmaroudi, L. M. Pazos-Outón, J. M. Richter, A. J. Pearson, H. Sirringhaus and M. Grätzel, *Sci. Adv.*, 2019, **5**, eaav2012.
224 S. N. Habisreutinger, T. Leijtens, G. E. Eperon, S. D. Stranks, R. J. Nicholas and H. J. Snaith, *Nano Lett.*, 2014, **14**, 5561-5568.
225 S. N. Habisreutinger, T. Leijtens, G. E. Eperon, S. D. Stranks, R. J. Nicholas and H. J. Snaith, *J. Phys. Chem. Lett.*, 2014, **5**, 4207-4212.
226 B. Wang, J. Iocozzia, M. Zhang, M. Ye, S. Yan, H. Jin, S. Wang, Z. Zou and Z. Lin, *Chem. Soc. Rev.*, 2019, **48**, 4854-4891.
227 S. S. Bhosale, E. Jokar, A. Fathi, C. M. Tsai, C. Y. Wang and E. W. G. Diau, *Adv. Funct. Mater.*, 2018, **28**, 1803200.
228 E. Jokar, Z. Y. Huang, S. Narra, C. Y. Wang, V. Kattoor, C. C. Chung and E. W. G. Diau, *Adv. Energy Mater.*, 2018, **8**, 1701640.
229 Q.-D. Yang, J. Li, Y. Cheng, H.-W. Li, Z. Guan, B. Yu and S.-W. Tsang, *J. Mater. Chem. A*, 2017, **5**, 9852-9858.
230 J. Du, J. Duan, X. Yang, Y. Duan, Q. Zhou and Q. Tang, *Angew. Chem.*, 2021, **133**, 10702-10707.
231 Y. Wang, T. Wu, J. Barbaud, W. Kong, D. Cui, H. Chen, X. Yang and L. Han, *Science*, 2019, **365**, 687-691.
232 G. Tang, P. You, Q. Tai, A. Yang, J. Cao, F. Zheng, Z. Zhou, J. Zhao, P. K. L. Chan and F. Yan, *Adv. Mater.*, 2019, **31**, 1807689.
233 X. Zhao, S. Liu, H. Zhang, S. Y. Chang, W. Huang, B. Zhu, Y. Shen, C. Shen, D. Wang and Y. Yang, *Adv. Funct. Mater.*, 2019, **29**, 1805168.
234 A. Agresti, S. Pescetelli, A. L. Palma, B. Martín-García, L. Najafi, S. Bellani, I. Moreels, M. Prato, F. Bonaccorso and A. Di Carlo, *ACS Energy Lett.*, 2019, **4**, 1862-1871.
235 G. Yin, H. Zhao, J. Feng, J. Sun, J. Yan, Z. Liu, S. Lin and S. F. Liu, *J. Mater. Chem. A*, 2018, **6**, 9132-9138.
236 P. Huang, Q. Chen, K. Zhang, L. Yuan, Y. Zhou, B. Song and Y. Li, *J. Mater. Chem. A*, 2019, **7**, 6213-6219.
237 J. Cao, G. Tang, P. You, T. Wang, F. Zheng, J. Zhao and F. Yan, *Adv. Funct. Mater.*, 2020, **30**, 2002358.
238 Q. Zhou, J. Duan, X. Yang, Y. Duan and Q. Tang, *Angew. Chem.*, 2020, **132**, 22181-22185.
239 B. Li, Y. Zhang, L. Fu, L. Zhang, Z. Liu and L. Yin, *J. Mater. Chem. A*, 2019, **7**, 22539-22549.
240 M. Zhang, M. Ye, W. Wang, C. Ma, S. Wang, Q. Liu, T. Lian, J. Huang and Z. Lin, *Adv. Mater.*, 2020, **32**, 2000999.
241 Z. Li, P. Wang, C. Ma, F. Igbari, Y. Kang, K.-L. Wang, W. Song, C. Dong, Y. Li and J. Yao, *J. Am. Chem. Soc.*, 2021, **143**, 2593-2600.
242 L. Huang, X. Zhou, R. Xue, P. Xu, S. Wang, C. Xu, W. Zeng, Y. Xiong, H. Sang and D. Liang, *Nano-micro letters*, 2020, **12**, 1-19.
243 A. Agresti, A. Pazniak, S. Pescetelli, A. Di Vito, D. Rossi, A. Pecchia, M. A. der Maur, A. Liedl, R. Larciprete and D. V. Kuznetsov, *Nat. Mater.*, 2019, **18**, 1228-1234.
244 A. Di Vito, A. Pecchia, M. Auf der Maur and A. Di Carlo, *Adv. Funct. Mater.*, 2020, **30**, 1909028.
245 D. Saranin, S. Pescetelli, A. Pazniak, D. Rossi, A. Liedl, A. Yakusheva, L. Luchnikov, D. Podgorny, P. Gostischev and S. Didenko, *Nano Energy*, 2021, **82**, 105771.
246 Y. Liu and Y. Chen, *Adv. Mater.*, 2020, **32**, 1805843.
247 S. Dong, Y. Liu, Z. Hong, E. Yao, P. Sun, L. Meng, Y. Lin, J. Huang, G. Li and Y. Yang, *Nano Lett.*, 2017, **17**, 5140-5147.
248 J. Yuan, Y. Zhang, L. Zhou, G. Zhang, H.-L. Yip, T.-K. Lau, X. Lu, C. Zhu, H. Peng and P. A. Johnson, *Joule*, 2019, **3**, 1140-1151.
249 F. Qi, K. Jiang, F. Lin, Z. Wu, H. Zhang, W. Gao, Y. Li, Z. Cai, H. Y. Woo and Z. Zhu, *ACS Energy Lett.*, 2020, **6**, 9-15.
250 X. Shi, X. Liao, K. Gao, L. Zuo, J. Chen, J. Zhao, F. Liu, Y. Chen and A. K. Y. Jen, *Adv. Funct. Mater.*, 2018, **28**, 1802324.
251 F. Lin, K. Jiang, W. Kaminsky, Z. Zhu and A. K.-Y. Jen, *J. Am. Chem. Soc.*, 2020, **142**, 15246-15251.
252 Y. Liu, Z. Hong, Q. Chen, W. Chang, H. Zhou, T.-B. Song, E.

Young, Y. Yang, J. You and G. Li, *Nano Lett.*, 2015, **15**, 662-668.
253 M. Cheng, C. Chen, K. Aitola, F. Zhang, Y. Hua, G. Boschloo, L. Kloo and L. Sun, *Chem. Mater.*, 2016, **28**, 8631-8639.
254 K. Gao, Z. Zhu, B. Xu, S. B. Jo, Y. Kan, X. Peng and A. K. Y. Jen, *Adv. Mater.*, 2017, **29**, 1703980.
255 Q. Guo, Y. Bai, K. Lang, Z.-Z. Yu, T. Hayat, A. Alsaedi, E. Zhou and Z. a. Tan, *ACS Appl. Mater. Interfaces*, 2019, **11**, 37991-37998.
256 W. Chen, D. Li, S. Chen, S. Liu, Y. Shen, G. Zeng, X. Zhu, E. Zhou, L. Jiang and Y. Li, *Adv. Energy Mater.*, 2020, **10**, 2000851.
257 L. Ye, B. Fan, S. Zhang, S. Li, B. Yang, Y. Qin, H. Zhang and J. Hou, *Science China Materials*, 2015, **58**, 953-960.
258 Y. Zhang, W. Yu, W. Qin, Z. Yang, D. Yang, Y. Xing, S. F. Liu and C. Li, *Nano Energy*, 2016, **20**, 126-133.
259 J. Kim, G. Kim, H. Back, J. Kong, I. W. Hwang, T. K. Kim, S. Kwon, J. H. Lee, J. Lee and K. Yu, *Adv. Mater.*, 2016, **28**, 3159-3165.
260 C. I. Chen, S. Wu, Y. A. Lu, C. C. Lee, K. C. Ho, Z. Zhu, W. C. Chen and C. C. Chueh, *Adv. Sci.*, 2019, **6**, 1901714.
261 X. Zhao, C. Yao, T. Liu, J. C. Hamill Jr, G. O. Ngongang Ndjawa, G. Cheng, N. Yao, H. Meng and Y. L. Loo, *Adv. Mater.*, 2019, **31**, 1904494.
262 M. Daboczi, J. Kim, J. Lee, H. Kang, I. Hamilton, C. T. Lin, S. D. Dimitrov, M. A. McLachlan, K. Lee, J. R. Durrant and J.-S. Kim, *Adv. Funct. Mater.*, 2020, **30**, 2001482.
263 W. Chen, H. Sun, Q. Hu, A. B. Djurišić, T. P. Russell, X. Guo and Z. He, *ACS Energy Lett.*, 2019, **4**, 2535-2536.
264 S. Essig, C. Allebé, T. Remo, J. F. Geisz, M. A. Steiner, K. Horowitz, L. Barraud, J. S. Ward, M. Schnabel and A. Descoeudres, *Nat. Energy*, 2017, **2**, 1-9.
265 A. Benmir and M. Aida, *Energy Procedia*, 2013, **36**, 618-627.
266 M. Wang, J. Yi, S. Yang, Z. Cao, X. Huang, Y. Li, H. Li and J. Zhong, *Appl. Surf. Sci.*, 2016, **382**, 217-224.
267 N. Mufti, T. Amrillah, A. Taufiq, M. Diantoro and H. Nur, *Sol. Energy*, 2020, **207**, 1146-1157.
268 A. F. Palmstrom, G. E. Eperon, T. Leijtens, R. Prasanna, S. N. Habisreutinger, W. Nemeth, E. A. Gaulding, S. P. Dunfield, M. Reese and S. Nanayakkara, *Joule*, 2019, **3**, 2193-2204.
269 C. Li, Y. Wang and W. C. Choy, *Small Methods*, 2020, **4**, 2000093.
270 X. Chen, Z. Jia, Z. Chen, T. Jiang, L. Bai, F. Tao, J. Chen, X. Chen, T. Liu, X. Xu, C. Yang, W. Shen, W. E. I. Sha, H. Zhu and Y. Yang, *Joule*, 2020, **4**, 1594-1606.
271 Z. Yu, Z. Yang, Z. Ni, Y. Shao, B. Chen, Y. Lin, H. Wei, J. Y. Zhengshan, Z. Holman and J. Huang, *Nat. Energy*, 2020, **5**, 657-665.
272 C. Li, Z. S. Wang, H. L. Zhu, D. Zhang, J. Cheng, H. Lin, D. Ouyang and W. C. Choy, *Adv. Energy Mater.*, 2018, **8**, 1801954.
273 C.-Y. Chang, B.-C. Tsai, Y.-C. Hsiao, M.-Z. Lin and H.-F. Meng, *Nano Energy*, 2019, **55**, 354-367.
274 J. H. Heo and S. H. Im, *Adv. Mater.*, 2016, **28**, 5121-5125.
275 G. E. Eperon, T. Leijtens, K. A. Bush, R. Prasanna, T. Green, J. T.-W. Wang, D. P. McMeekin, G. Volonakis, R. L. Milot and R. May, *Science*, 2016, **354**, 861-865.
276 A. Rajagopal, Z. Yang, S. B. Jo, I. L. Braly, P. W. Liang, H. W. Hillhouse and A. K.-Y. Jen, *Adv. Mater.*, 2017, **29**, 1702140.
277 D. Zhao, C. Chen, C. Wang, M. M. Junda, Z. Song, C. R. Grice, Y. Yu, C. Li, B. Subedi, N. J. Podraza, X. Zhao, G. Fang, R.-G. Xiong, K. Zhu and Y. Yan, *Nat. Energy*, 2018, **3**, 1093-1100.
278 J. Tong, Z. Song, D. H. Kim, X. Chen, C. Chen, A. F. Palmstrom, P. F. Ndione, M. O. Reese, S. P. Dunfield and O. G. Reid, *Science*, 2019, **364**, 475-479.
279 R. Lin, K. Xiao, Z. Qin, Q. Han, C. Zhang, M. Wei, M. I. Saidaminov, Y. Gao, J. Xu, M. Xiao, A. Li, J. Zhu, E. H. Sargent and H. Tan, *Nat. Energy*, 2019, **4**, 864-873.
280 K. Xiao, R. Lin, Q. Han, Y. Hou, Z. Qin, H. T. Nguyen, J. Wen, M. Wei, V. Yeddu, M. I. Saidaminov, Y. Gao, X. Luo, Y. Wang, H. Gao, C. Zhang, J. Xu, J. Zhu, E. H. Sargent and H. Tan, *Nat. Energy*, 2020, **5**, 870-880.
281 D. Zhao, Y. Yu, C. Wang, W. Liao, N. Shrestha, C. R. Grice, A. J. Cimaroli, L. Guan, R. J. Ellingson, K. Zhu, X. Zhao, R.-G. Xiong and Y. Yan, *Nat. Energy*, 2017, **2**, 17018.
282 D. Zhao, C. Wang, Z. Song, Y. Yu, C. Chen, X. Zhao, K. Zhu and Y. Yan, *ACS Energy Letters*, 2018, **3**, 305-306.
283 S. Albrecht, M. Saliba, J. P. Correa Baena, F. Lang, L. Kegelmann, M. Mews, L. Steier, A. Abate, J. Rappich, L. Korte, R. Schlatmann, M. K. Nazeeruddin, A. Hagfeldt, M. Grätzel and B. Rech, *Energy Environ. Sci.*, 2016, **9**, 81-88.
284 K. A. Bush, A. F. Palmstrom, Z. J. Yu, M. Boccard, R. Cheacharoen, J. P. Mailoa, D. P. McMeekin, R. L. Z. Hoye, C. D. Bailie, T. Leijtens, I. M. Peters, M. C. Minichetti, N. Rolston, R. Prasanna, S. Sofia, D. Harwood, W. Ma, F. Moghadam, H. J. Snaith, T. Buonassisi, Z. C. Holman, S. F. Bent and M. D. McGehee, *Nat. Energy*, 2017, **2**, 17009.
285 D. Kim, H. J. Jung, I. J. Park, B. W. Larson, S. P. Dunfield, C. Xiao, J. Kim, J. Tong, P. Boonmongkolras and S. G. Ji, *Science*, 2020, **368**, 155-160.
286 N. R. E. L. (NREL), *Best Research-Cell Efficiencies Chart*, **https://www.nrel.gov/pv/cell-efficiency.html**.
287 P. Loper, S. J. Moon, S. M. de Nicolas, B. Niesen, M. Ledinsky, S. Nicolay, J. Bailat, J. H. Yum, S. De Wolf and C. Ballif, *Phys. Chem. Chem. Phys.*, 2015, **17**, 1619-1629.
288 J. Werner, L. Barraud, A. Walter, M. Bräuninger, F. Sahli, D. Sacchetto, N. Tétreault, B. Paviet-Salomon, S.-J. Moon, C. Allebé, M. Despeisse, S. Nicolay, S. De Wolf, B. Niesen and C. Ballif, *ACS Energy Lett.*, 2016, **1**, 474-480.
289 M. Jaysankar, M. Filipič, B. Zielinski, R. Schmager, W. Song, W. Qiu, U. W. Paetzold, T. Aernouts, M. Debucquoy, R. Gehlhaar and J. Poortmans, *Energy Environ. Sci.*, 2018, **11**, 1489-1498.
290 M. Jaysankar, B. A. L. Raul, J. Bastos, C. Burgess, C. Weijtens, M. Creatore, T. Aernouts, Y. Kuang, R. Gehlhaar, A. Hadipour and J. Poortmans, *ACS Energy Lett.*, 2018, **4**, 259-264.
291 T. Duong, H. Pham, T. C. Kho, P. Phang, K. C. Fong, D. Yan, Y. Yin, J. Peng, M. A. Mahmud, S. Gharibzadeh, B. A. Nejand, I. M. Hossain, M. R. Khan, N. Mozaffari, Y. Wu, H. Shen, J. Zheng, H. Mai, W. Liang, C. Samundsett, M. Stocks, K. McIntosh, G. G. Andersson, U. Lemmer, B. S. Richards, U. W. Paetzold, A. Ho-Ballie, Y. Liu, D. Macdonald, A. Blakers, J. Wong-Leung, T. White, K. Weber and K. Catchpole, *Adv. Energy Mater.*, 2020, **10**, 1903553.
292 T. Todorov, T. Gershon, O. Gunawan, Y. S. Lee, C. Sturdevant, L.-Y. Chang and S. Guha, *Adv. Energy Mater.*, 2015, **5**, 1500799.
293 A. Al-Ashouri, A. Magomedov, M. Roß, M. Jošt, M. Talaikis, G. Chistiakova, T. Bertram, J. A. Márquez, E. Köhnen, E. Kasparavičius, S. Levcenco, L. Gil-Escrig, C. J. Hages, R. Schlatmann, B. Rech, T. Malinauskas, T. Unold, C. A. Kaufmann, L. Korte, G. Niaura, V. Getautis and S. Albrecht, *Energy Environ. Sci.*, 2019, **12**, 3356-3369.
294 F. Fu, T. Feurer, T. Jager, E. Avancini, B. Bissig, S. Yoon, S.

Buecheler and A. N. Tiwari, *Nat. Commun.*, 2015, **6**, 8932.
295 F. Fu, T. Feurer, Thomas P. Weiss, S. Pisoni, E. Avancini, C. Andres, S. Buecheler and Ayodhya N. Tiwari, *Nat. Energy*, 2016, **2**, 16190.
296 H. Shen, T. Duong, J. Peng, D. Jacobs, N. Wu, J. Gong, Y. Wu, S. K. Karuturi, X. Fu, K. Weber, X. Xiao, T. P. White and K. Catchpole, *Energy Environ. Sci.*, 2018, **11**, 394-406.
297 D. H. Kim, C. P. Muzzillo, J. Tong, A. F. Palmstrom, B. W. Larson, C. Choi, S. P. Harvey, S. Glynn, J. B. Whitaker, F. Zhang, Z. Li, H. Lu, M. F. A. M. van Hest, J. J. Berry, L. M. Mansfield, Y. Huang, Y. Yan and K. Zhu, *Joule*, 2019, **3**, 1734-1745.
298 Q. Han, Y.-T. Hsieh, L. Meng, J.-L. Wu, P. Sun, E.-P. Yao, S.-Y. Chang, S.-H. Bae, T. Kato and V. Bermudez, *Science*, 2018, **361**, 904-908.
299 S. Albrecht, M. Saliba, J. P. C. Baena, F. Lang, L. Kegelmann, M. Mews, L. Steier, A. Abate, J. Rappich and L. Korte, *Energy Environ. Sci.*, 2016, **9**, 81-88.
300 J. Zheng, C. F. J. Lau, H. Mehrvarz, F.-J. Ma, Y. Jiang, X. Deng, A. Soeriyadi, J. Kim, M. Zhang and L. Hu, *Energy Environ. Sci.*, 2018, **11**, 2432-2443.
301 J. Zheng, H. Mehrvarz, F.-J. Ma, C. F. J. Lau, M. A. Green, S. Huang and A. W. Ho-Baillie, *ACS Energy Lett.*, 2018, **3**, 2299-2300.
302 P. Löper, S.-J. Moon, S. M. De Nicolas, B. Niesen, M. Ledinsky, S. Nicolay, J. Bailat, J.-H. Yum, S. De Wolf and C. Ballif, *PCCP*, 2015, **17**, 1619-1629.
303 F. Sahli, J. Werner, B. A. Kamino, M. Bräuninger, R. Monnard, B. Paviet-Salomon, L. Barraud, L. Ding, J. J. D. Leon and D. Sacchetto, *Nat. Mater.*, 2018, **17**, 820-826.
304 Y. Hou, E. Aydin, M. De Bastiani, C. Xiao, F. H. Isikgor, D.-J. Xue, B. Chen, H. Chen, B. Bahrami and A. H. Chowdhury, *Science*, 2020, **367**, 1135-1140.
305 B. Chen, J. Y. Zhengshan, S. Manzoor, S. Wang, W. Weigand, Z. Yu, G. Yang, Z. Ni, X. Dai, Z. C. Holman and J. Huang, *Joule*, 2020, **4**, 850-864.
306 F. Sahli, B. A. Kamino, J. Werner, M. Bräuninger, B. Paviet-Salomon, L. Barraud, R. Monnard, J. P. Seif, A. Tomasi and Q. Jeangros, *Adv. Energy Mater.*, 2018, **8**, 1701609.
307 L. Mazzarella, Y. H. Lin, S. Kirner, A. B. Morales-Vilches, L. Korte, S. Albrecht, E. Crossland, B. Stannowski, C. Case and H. J. Snaith, *Adv. Energy Mater.*, 2019, **9**, 1803241.
308 J. Zheng, H. Mehrvarz, C. Liao, J. Bing, X. Cui, Y. Li, V. R. Gonçales, C. F. J. Lau, D. S. Lee and Y. Li, *ACS Energy Lett.*, 2019, **4**, 2623-2631.
309 K. A. Bush, S. Manzoor, K. Frohna, Z. J. Yu, J. A. Raiford, A. F. Palmstrom, H.-P. Wang, R. Prasanna, S. F. Bent and Z. C. Holman, *ACS Energy Lett.*, 2018, **3**, 2173-2180.
310 H. Shen, S. T. Omelchenko, D. A. Jacobs, S. Yalamanchili, Y. Wan, D. Yan, P. Phang, Y. Wu, Y. Yin and C. Samundsett, *Sci. Adv.*, 2018, **4**, eaau9711.
311 B. Chen, Y. Bai, Z. Yu, T. Li, X. Zheng, Q. Dong, L. Shen, M. Boccard, A. Gruverman and Z. Holman, *Adv. Energy Mater.*, 2016, **6**, 1601128.
312 K. Yoshikawa, H. Kawasaki, W. Yoshida, T. Irie, K. Konishi, K. Nakano, T. Uto, D. Adachi, M. Kanematsu, H. Uzu and K. Yamamoto, *Nat. Energy*, 2017, **2**, 17032.
313 B. Chen, Z. Yu, K. Liu, X. Zheng, Y. Liu, J. Shi, D. Spronk, P. N. Rudd, Z. Holman and J. Huang, *Joule*, 2019, **3**, 177-190.
314 D. P. McMeekin, G. Sadoughi, W. Rehman, G. E. Eperon, M. Saliba, M. T. Hörantner, A. Haghighirad, N. Sakai, L. Korte and B. Rech, *Science*, 2016, **351**, 151-155.
315 T. Duong, H. Pham, T. C. Kho, P. Phang, K. C. Fong, D. Yan, Y. Yin, J. Peng, M. A. Mahmud and S. Gharibzadeh, *Adv. Energy Mater.*, 2020, **10**, 1903553.
316 M. Jaysankar, B. A. Raul, J. Bastos, C. Burgess, C. Weijtens, M. Creatore, T. Aernouts, Y. Kuang, R. Gehlhaar and A. Hadipour, *ACS Energy Lett.*, 2018, **4**, 259-264.
317 T. Duong, Y. Wu, H. Shen, J. Peng, X. Fu, D. Jacobs, E. C. Wang, T. C. Kho, K. C. Fong and M. Stocks, *Adv. Energy Mater.*, 2017, **7**, 1700228.
318 J. Xu, C. C. Boyd, J. Y. Zhengshan, A. F. Palmstrom, D. J. Witter, B. W. Larson, R. M. France, J. Werner, S. P. Harvey and E. J. Wolf, *Science*, 2020, **367**, 1097-1104.
319 E. Dilena, Y. Xie, R. Brescia, M. Prato, L. Maserati, R. Krahne, A. Paolella, G. Bertoni, M. Povia and I. Moreels, *Chem. Mater.*, 2013, **25**, 3180-3187.
320 Y.-H. A. Wang, X. Zhang, N. Bao, B. Lin and A. Gupta, *J. Am. Chem. Soc.*, 2011, **133**, 11072-11075.
321 R. Kamada, T. Yagioka, S. Adachi, A. Handa, K. F. Tai, T. Kato and H. Sugimoto, 2016.
322 P. Jackson, D. Hariskos, R. Wuerz, O. Kiowski, A. Bauer, T. M. Friedlmeier and M. Powalla, *physica status solidi (RRL)–Rapid Research Letters*, 2015, **9**, 28-31.
323 S. Pisoni, F. Fu, T. Feurer, M. Makha, B. Bissig, S. Nishiwaki, A. N. Tiwari and S. Buecheler, *J. Mater. Chem. A*, 2017, **5**, 13639-13647.
324 M. Jošt, T. Bertram, D. Koushik, J. A. Marquez, M. A. Verheijen, M. D. Heinemann, E. Köhnen, A. Al-Ashouri, S. Braunger and F. Lang, *ACS Energy Lett.*, 2019, **4**, 583-590.
325 A. Al-Ashouri, A. Magomedov, M. Roß, M. Jošt, M. Talaikis, G. Chistiakova, T. Bertram, J. A. Márquez, E. Köhnen and E. Kasparavičius, *Energy Environ. Sci.*, 2019, **12**, 3356-3369.
326 Y. H. Jang, J. M. Lee, J. W. Seo, I. Kim and D.-K. Lee, *J. Mater. Chem. A*, 2017, **5**, 19439-19446.
327 T. Todorov, T. Gershon, O. Gunawan, Y. S. Lee, C. Sturdevant, L. Y. Chang and S. Guha, *Adv. Energy Mater.*, 2015, **5**, 1500799.
328 A. R. Uhl, Z. Yang, A. K.-Y. Jen and H. W. Hillhouse, *J. Mater. Chem. A*, 2017, **5**, 3214-3220.
329 H. Shen, J. Peng, D. Jacobs, N. Wu, J. Gong, Y. Wu, S. K. Karuturi, X. Fu, K. Weber and X. Xiao, *Energy Environ. Sci.*, 2018, **11**, 394-406.
330 A. Rajagopal, Z. Yang, S. B. Jo, I. L. Braly, P. W. Liang, H. W. Hillhouse and A. K. Y. Jen, *Adv. Mater.*, 2017, **29**, 1702140.
331 D. Zhao, C. Chen, C. Wang, M. M. Junda, Z. Song, C. R. Grice, Y. Yu, C. Li, B. Subedi and N. J. Podraza, *Nat. Energy*, 2018, **3**, 1093-1100.
332 R. Lin, K. Xiao, Z. Qin, Q. Han, C. Zhang, M. Wei, M. I. Saidaminov, Y. Gao, J. Xu and M. Xiao, *Nat. Energy*, 2019, **4**, 864-873.
333 X. Wu, Y. Liu, F. Qi, F. Lin, H. Fu, K. Jiang, S. Wu, L. Bi, D. Wang and F. Xu, *J. Mater. Chem. A*, 2021, DOI: 10.1039/D0TA12286F
334 J. Liu, S. Lu, L. Zhu, X. Li and W. C. Choy, *Nanoscale*, 2016, **8**, 3638-3646.
335 W. Chen, J. Zhang, G. Xu, R. Xue, Y. Li, Y. Zhou, J. Hou and Y. Li, *Adv. Mater.*, 2018, **30**, 1800855.
336 Z. Li, S. Wu, J. Zhang, K. C. Lee, H. Lei, F. Lin, Z. Wang, Z. Zhu and A. K. Jen, *Adv. Energy Mater.*, 2020, **10**, 2000361.
337 S. Xie, R. Xia, Z. Chen, J. Tian, L. Yan, M. Ren, Z. Li, G. Zhang, Q. Xue and H.-L. Yip, *Nano Energy*, 2020, **78**, 105238.
338 H. Aqoma, I. F. Imran, F. T. A. Wibowo, N. V. Krishna, W. Lee, A. K. Sarker, D. Y. Ryu and S. Y. Jang, *Adv. Energy Mater.*,

2020, **10**, 2001188.
339 X. Chen, Z. Jia, Z. Chen, T. Jiang, L. Bai, F. Tao, J. Chen, X. Chen, T. Liu and X. Xu, *Joule*, 2020, **4**, 1594-1606.
340 J. Wang, V. Zardetto, K. Datta, D. Zhang, M. M. Wienk and R. A. Janssen, *Nat. Commun.*, 2020, **11**, 5254.
341 J. r. m. Werner, F. Sahli, F. Fu, J. J. Diaz Leon, A. Walter, B. A. Kamino, B. Niesen, S. Nicolay, Q. Jeangros and C. Ballif, *ACS Energy Lett.*, 2018, **3**, 2052-2058.
342 D. P. McMeekin, S. Mahesh, N. K. Noel, M. T. Klug, J. Lim, J. H. Warby, J. M. Ball, L. M. Herz, M. B. Johnston and H. J. Snaith, *Joule*, 2019, **3**, 387-401.
343 X. Jiang, H. Li, Q. Zhou, Q. Wei, M. Wei, L. Jiang, Z. Wang, Z. Peng, F. Wang and Z. Zang, *J. Am. Chem. Soc.*, 2021, **143**, 10970-10976.
344 B. Li, H. Di, B. Chang, R. Yin, L. Fu, Y. N. Zhang and L. Yin, *Adv. Funct. Mater.*, 2021, **31**, 2007447.
345 D. Cui, X. Liu, T. Wu, X. Lin, X. Luo, Y. Wu, H. Segawa, X. Yang, Y. Zhang and Y. Wang, *Adv. Funct. Mater.*, 2021, 2100931.

Biography

Xin Wu obtained his B.S. degree and M.S. degree in 2016 and 2019 from the School of Chemistry, Beihang University. Currently, he is undertaking a PhD study in Department of Chemistry, City University of Hong Kong. His research focuses on physical properties of perovskite materials, carbon-based perovskite solar cells, inverted perovskite solar cells, and perovskite-based tandem solar cells.

Dr. Bo Li is currently a postdoctoral fellow in Department of Materials Science and Engineering, City University of Hong Kong. His research focuses on the structure design and photophysics of semiconductor materials, lead-free perovskite solar cells, and inorganic perovskite solar cells

Dr. Zonglong Zhu is an Assistant Professor in Department of Chemistry, City University of Hong Kong. He obtained his B.S. degree (Chemistry) in 2010 from Nanjing University (China). In 2015, he earned his Ph.D. degree in Hong Kong University of Science and Technology (HKUST). Then he worked at the Department of Materials Science and Engineering in the University of Washington as a postdoctoral fellow. His research mainly focuses on the design inorganic/organic materials, as well connecting the materials synthesis, physical properties and device performance for optoelectronics application.

Dr. Chu-Chen Chueh received his Ph.D. in Chemical Engineering from the National Taiwan University (NTU) in 2010 and conducted his postdoctoral research at the University of Washington from 2011 to 2016. He joined NTU as an Assistant Professor of Department of Chemical Engineering in 2017. His research focus on the development of polymer semiconductors and organic/hybrid semiconductors and their applications in memory, light-emitting diode, transistors, and solar cells.

Prof. Alex K.-Y. Jen is currently serving as the Lee Shau Kee Chair Professor of the City University of Hong Kong. Before this, he served as the Provost for the CityU and the Boeing-Johnson Chair Professor and Chair of the Department of Materials Science and Engineering at the University of Washington. He also served as the Chief Scientist for the Clean Energy Institute endowed by the Washington State Governor. His research interest is focused on utilizing molecular, polymeric-, and bio-macromolecular self-assembly to create ordered arrangement of organic and inorganic functional materials for applications in photonics, optoelectronics, energy, nanomedicine and nanotechnology, and employing the "molecular engineering" approach to tailor size, shape, sequence, and functionality of organic/hybrid functional materials and explore their applications.